Microscopic Model To Investigate Stress-Strain Response For Polymer Nanocomposites Containing Rod-Like Particles

A Thesis

submitted to

Indian Institute of Science Education and Research, Pune

in partial fulfillment of the requirements for the BS-MS Dual Degree Programme

by

Somesh Kurahatti

Registration No : 20171182



Indian Institute of Science Education and Research, Pune

Dr Homi Bhabha Road,

Pashan,Pune 411008,

INDIA

May 2022

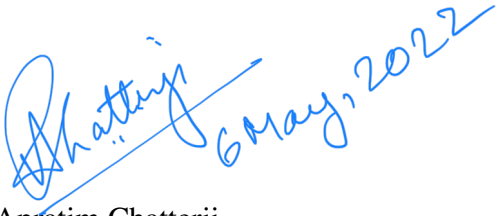
Supervisor: Dr. Apratim Chatterji

© Somesh Kurahatti 2022

All rights reserved

Certificate

This is to certify that this dissertation entitled ”Microscopic Model To Investigate Stress-Strain Response For Polymer Nanocomposites Containing Rod-Like Particles” towards the partial fulfilment of the BS-MS dual degree programme at the Indian Institute of Science Education and Research, Pune represents study/work carried out by Somesh Kurahatti at Indian Institute of Science Education and Research under the supervision of Apratim Chatterji, Associate Professor, Department of Physics during the academic year 2021-2022.



Somesh Kurahatti

Apratim Chatterji

Committee:

Apratim Chatterji

Vijayakumar Chikkadi

Abstract

Polymer nanocomposites are an important class of materials that exhibit distinct physicochemical properties that are inaccessible with individual components acting alone. These nanocomposites have recently attracted intensive research owing to their potential industrial interests. Polymers nanocomposites consist of nanofillers dispersed in the polymer matrix. Applications of these composites are enhanced by making them porous.

This project is an endeavor to study the mechanical properties of such composite containing the porous percolating structure of the nanoparticle-polymer mesh surrounding micron-sized inter-connected voids. In experiments, such porous structures are realized by the ice-templating method such that nanoparticles(NPs) are trapped in polymer mesh, which forms the walls around large inter-connected open voids. The nanoparticles are held together by polymers and cross-linkers. We approximate the interaction between them by a simple coarse-grained description which consists of springs. The mechanical response arises primarily from the network of cross-linked polymer and not from the nanoparticles. These nanocomposites with $90-95\%$ porosity are potential interests. They retain their original shape and size after the release of uni-axial compression up to 20% of their original volume. The stress response of NP-polymer mesh containing spherical particles has been microscopically modeled and the plot/data matches the experiment. We use non-equilibrium molecular dynamics as implemented in LAMMPS for our studies.

First we benchmark the previous results for the coarse-grained model.

- We replace the spherical voids in this model with cubical voids and note the change

in response.

- We obtain the functional dependence of Young's Modulus on the nominal density ρ_0 of the scaffold containing spherical particles.
- Our focus will be on nanocomposites that incorporate anisotropic rod particles. We also derive the functional dependence of Y on nominal density ρ_0 for scaffolds incorporating rod particles.

This increases the complexity as non-spherical particles have an additional orientation degree of freedom. The aspect ratio of rod-like fillers strongly influences the mechanical response of hybrid nanocomposites. Experimentally mechanical response of nanocomposites prepared from ellipsoidal fillers has been shown to have complex non-trivial behavior whose microscopic detail is not understood. Elastic modulus (Y) shows non-trivial dependence on the nominal density ρ_0 of the sponge. In experiments, we observe a scaling in ρ_0 dependence of G from linear to quadratic as the aspect ratio increases from 1 to 4 arising due to a change in the mechanism of sponge response. Understanding the interplay between filler aspect ratio and filler matrix interaction has important implications for the control of nanocomposite properties.

Dedication

To My Mother.

Declaration

I hereby declare that the matter embodied in the report entitled ”Microscopic Model To Investigate Stress-Strain Response For Polymer Nanocomposites Containing Rod-Like Particles” are the results of the investigations carried out by me at the Department of Physics, IISER Pune, under the supervision of Dr. Apratim Chatterji and the same has not been submitted elsewhere for any other degree.



Acknowledgements

I thank my supervisor, Dr. Apratim Chatterji, whose expertise was invaluable in formulating the research questions and methodology. He always made sure we had all the resources at our disposal which accelerated the research. I acknowledge the institute for high-performance PARAM-BRAHMA cluster. I am extremely grateful to thesis expert Dr. Vijayakumar Chikkadi who allowed me to use his supercomputer account. My sincere thanks to Dr. Guruswamy Kumaraswamy and Anish Sukumar, for their assistance to validate some major results in the thesis. Completion of the project could not have been accomplished without my beloved friend Dhruvanshu Parmar. I would like to express my sincere gratitude for his unwavering support throughout the project.
I am overwhelmed by the humbleness and support of my fellow lab mates. I thank Debarshi Mitra, Shreerang Pande, Nishant Bharuah for their relentless support and lively chess matches. I thank Dipanshu Garg, Lalit Singh Bhandari, Sakil Khan, and Priya Batra for their countless suggestions. Special thanks to Debarshi Mitra for his guidance as my senior.

Contents

1 Introduction **1**

1.1 Thesis Outline 4

1.2 Motivation for this Thesis 5

1.3 The Ice Templating Method 6

1.3.1 For Spherical Silica Particles 6

1.3.2 For Anisotropic Hematite Particles 7

1.4 The Mechanical Response of Monolith to Compression 9

1.5 Entropic Origin of Monolith Mechanical Response 10

1.6 Scaling Laws 11

1.7 Effect of Nanofiller Size and Shape 12

1.8 Response of Monolith is Chemistry Independent 14

2 Computational Models and Methods **15**

2.1 Spherical Particles and Spherical Voids 15

2.2 Spherical Particles and Cubical Voids 22

2.2.1 Procedure for creating cubical voids 23

2.3 Modelling Rod-like Particles 28

2.3.1 Details of Modelling 28

2.3.2 Creating Cubical Voids for System with Rod-like particles 28

3 Results and Discussions **35**

3.1 Validation of Previous Results 35

3.1.1 Stress-strain response 35

3.1.2 Microscopic response to applied strain 37
3.2 Results for Spherical Particles with Cubical Voids 40
3.2.1 Stress-strain response. 41
3.2.2 Calculation of Young's modulus 45
3.3 Results for Rod-like Particles with Cubical Voids 51
3.3.1 Stress-strain response 52
3.3.2 Calculation of Young's modulus 56

4 Conclusion **63**

A Appendix **67**
A.1 Void volume fraction calculation 67
A.1.1 Void volume fraction calculation for open spherical voids 67
A.1.2 Void volume fraction for spherical and cubical voids 68
A.2 LAMMPS Instructions 69

List of Figures

1.1 Diagram shows the schematic macroporous polymer nanocomposite. . . 2

1.2 Zoomed in view of the above figure 2

1.3 Man-made foams. From left: Open cell polyurethane, closed cell polyurethane, aluminum honeycomb. (Source: Reproduced from [9] with permission.) . 3

1.4 Naturally occurring foams. From left: Cork, wood, sponge. (Source: Reproduced from [9] with permission.) 3

1.5 Schematic shows how the inorganic sponge is prepared. An aqueous solution of silica particles, polymers, and crosslinkers is frozen. These components are expelled by growing ice-crystals which consolidate to form the walls of the sponge. After the ice is removed we obtain a dry macroporous scaffold consisting of NPs enmeshed in the network of polymer.(Source: Reproduced from [8] with permission.) 7

1.6 SEM images of the experimental system.(Source: Reproduced from [8] with due permission.) 7

1.7 Scanning electron microscopy hematite particles of aspect ratio (a) 1.0 (b) 2.2 (c) 4.0 .(Source: Reproduced from [22] with due permission.) . . 8

1.8 Schematic of scaffold preparation protocol and the scanning electron micrographs of scaffolds made of hematite particle with aspect ratios (a) and (b) $\sim$1, (c) and (d) $\sim$2.2, and (e) and (f) $\sim$4. (b), (d), and (f) are the high resolution SEM images of pore walls.(Source: Reproduced from [22] with due permission.) 8

1.9 Elastic recovery is observed after compressing the scaffold upto 15% of its original size. Water is squeezed out during compression and re-absorbed as it regains its original size. (Source: Reproduced from [19] with due permission.) 9

1.10 A schematic mechanical response of macroporous sponge upon uniaxial compression. Three distinct regions are demarcated. 10

1.11 SEM image of $1\mu m$ silica scaffolds prepared by ice-templating. a) $\phi = 10\%$ b) $\phi = 30\%$ c) $\phi = 40\%$. d) Nominal stress strain data for scaffolds obtained by varying colloid fraction $\phi = 10\%, 30\%, 40\%$. e)Young's Modulus(E^*) and shear modulus(G^*) also varies linealy with monolith bulk density. (Source: Reproduced from [19] with due permission.) . . . 11

1.12 Storage and Young's moduli as a function of scaffold nominal density (ρ_0) for scaffolds made of hematite particles with aspect ratios (a) ~ 1, (b) ~ 2.2, and (c) ~ 4. (Source: Reproduced from [22] with due permission.) 12

2.1 A schematic of how the inorganic sponge is prepared in our simulation model. Left box: The NPs are initialized in an FCC lattice surrounding 27 large spheres arranged in a $3 \times 3 \times 3$ cubic lattice where the grey spheres mimic ice-crystals. We implement excluded volume interaction between the NPs and the large grey spheres. We do not model the polymers in this step. Middlebox: After sufficient equilibration of NPs with large spheres in place we obtain a liquid-like short range order. Right box: We connect the NPs by springs with neighboring NPs; the spring network mimics the mesh of cross-linked polymers, which hold the NPs in place. Simultaneously the big spheres (which mimic the ice crystals) are removed from the simulation box such that voids remain. The NPs connected by springs (the NPs are enmeshed by the polymer gel in experiments) remain in position surrounding the voids, after which we do NVT and then NPT molecular dynamics simulations to prepare the system before applying uniaxial strain on the scaffold. (Source: Reproduced from [8] with due permission.) 16

2.2 Left: Initiaization of NPs and large spheres. Right: After equilibration of NPs in the NVT ensemble 17

2.3 Left: Figure shows the image $\rho_0 = 0.345 g/cc$ system after equilibration. Right: Shows the cross-section of the same system. 19

2.4 Left: The L_Y and L_z are plotted versus the strain γ. L_y , L_z increase linearly with γ in Regime-I, show a plateau regime in regime-II and start increasing from regime-III. Right: The figure shows the Stress-strain data during compression from 0 to 0.8, and relaxation from 0.8 to 0. (The nominal density (ρ_0) is in g/cc) 20

2.5 A plot of potential energy per particle(in k_BT units) as a function of strain. 22

2.6 Shows the images of the system having densities $\rho_0 = 0.307, 0.296, 0.253, 0.223, 0.199, 0.186, 0$ from top to bottom. The densities are in g/cc. Note the increase in pore size as the length of the simulation box increases while the bridge thickness Δ remains constant across different densities. 26

2.7 Nanoparticles whose centers are located within the defined cylindrical regions of radius r_S and length $L\sigma$ in the simulation box as shown in the figure are retained. There are 16 cylindrical regions defined between a pair of opposite faces and hence we define a total of 48 such cylindrical regions in the simulation box. The NPs whose centers are not located inside the union of 48 cylindrical regions, are simply deleted. 27

2.8 Left: Shows the $\phi_v = 0.86$ system before removing the NPs by defining cylindrical regions. Right: After removing the NPs. 27

2.9 Constructing a rod-like particle by connecting spherical particles in a linear fashion. Here the aspect ratio is 4.75. 29

2.10 The maximum distance upto which a bead of another rod can come between a pair of adjacent beads(left) is AB = 0.345. 30

2.11 Shows the images of the system $\rho_0 = 0.247 g/cc$ having order parameter $S_2 \sim 0.8$ for all possible angle of view. There is an artefact in designing this $\rho_0 = 0.247 g/cc$ system leading to the appearence of spherical voids(top right image), that will be corrected in the final submission. . . . 32

2.12 Shows the images of the system $\rho_0 = 0.247 g/cc$ having order parameter $S_2 \sim 0.4$ for all possible angle of view 33

2.13 Shows the images of the system $\rho_0 = 0.247 g/cc$ having order parameter $S_2 \sim 0.0$ for all possible angle of view 34

3.1 Left: Response of the system to applied strain by plotting σ_{xx} vs γ for several different values of the nominal density ρ_0, in units of g/cc. A decrease in the nominal density corresponds to an increase in the void fraction ϕ_V (at $\gamma = 0$). Right: The linear modulus Y is calculated from the slope of the stress-strain plots at low strains ($\gamma \to 0$). Y increases monotonically with the nominal density ρ_0. 36

3.2 Left: The pair correlation function $g(r)$ vs distance r from a NP at different values of strains as given in legend, for a system of void fraction $\phi_v = 0.55$ (i.e.$\rho_0 = 0.49 g/cc$) with $R_{CL} = 1.5\sigma$. The inset shows the zoomed-in $g(r)$ so that the change in the position of the peaks of $g(r)$ can be easily identified. Right: An estimate of the mean distance of the nearest neighbors of a NP r_{mean} (refer to text for calculation details) as a function of the strain γ is shown for different ρ_0 38

3.3 Left: Probability distribution $P(\delta r)$ of the deviation of bonds from its mean length vs the deviation δ is shown. The three vertical dashed line at $\delta r = -22\dot{A}, 0$ and $22\dot{A}$ are drawn to help the eye discern the asymmetry in the distribution. On an average the bonds are more extended than compressed. Right: probability densities of length fluctuations of interface springs for $\phi_V = 0.55$ 39

3.4 The mean deviation of the springs from their equi- librium positions δr_{mean} is calculated from the probability density distribution of the deviation of springs from their mean position δr is plotted as a function of strain for $\rho_0 = 0.34 g/cc$. Note : For the calculation of δr_{mean} of interface and bulk NPs, we have only considered springs which explicitly connect interface and bulk particles. 39

3.5 We compare the value of σ_{xx} obtained for both spherical voids and cubical voids scaffolds with nearly ρ_0 and ρ_V as mentioned in the text. Cubical voids scaffold have $r_s \sim 4.2\sigma$. Cubical voids have a stronger initial response but the value γ_T is relatively less. 42

3.6 The instantaneous stress-response σ_{xx} is plotted as a function of strain for systems containing spherical particles. The cubical voids are created by cylindrical regions of radius $r_S = 3.5\sigma$.(Nominal densities ρ_0 are in g/cc) 43

3.7 The instantaneous stress-response σ_{xx} is plotted as a function of strain for systems containing spherical particles. The cubical voids are created by cylindrical regions of radius $r_S = 4.5\sigma$. We observe less fluctuations in the σ_{xx} values compared to the above figure3.6 where $r_S = 3.5\sigma$ as the bridges are more thicker for systems with $r_S = 4.5\sigma$. (Nominal densities ρ_0 are in g/cc) 44

3.8 Plot of $\sigma_{xx}(\gamma)$ for $r_s = 4.5\sigma$, here we have plotted σ_{xx} upto $\gamma = 0.6$. We observe oscillations decay gradually before the system enters regime-3. (Note: The values of σ_{xx} are averaged out.) 45

3.9 Plot of σ_{xx} for modified cubical voids systems. All the systems with densities $\rho_0 = 0.346 - 0.085 g/cc$ are produced from the system with $L = 55.9\sigma$ case in table 2.1 by retaining NPs in various cylindrical and spherical regions as tabulated in table 3.1. Note: we do not have oscillations in the σ_{xx} values, hence we conclude cubical voids arranged in the cubical lattice that leads to shaping of long beams between the junctions is the source of oscillation. Additional spherical regions are defined at junctions (where the beams meet) so that more number of NPs remain at junctions and do not form long beams. 46

3.10 Linear modulus Y is plotted against nominal density ρ_0 for scaffolds with spherical voids. The Young's modulus is calculated from the slope of initial linear regime in the above figure3.9. 47

3.11 Pair-correlation plots for 4 cubical voids scaffolds of varying densities as given in the plot. Since the void-volume fraction here is large compared to spherical void scaffolds, height of the first peak always deceases as $\gamma(0 \to 0.8)$. Height of the first peak of $g(r)$ increases as we go to lower densities for the same value of γ. This is because we have normalized $g(r)$ values by nominal density ρ_0. Instead if we normalize by intrinsic density ρ_I then the height of the first peak will be same for different densities and $g(r) \to 1$ for sufficiently large r. 48

3.12 Pair-correlation plots normalized with intrinsic number density $n_{NP}/((1-\phi_V)L^3)$ for $\gamma = 0$.. Since the height of the first peak gives the probable number density of neighbouring NPs, same height of the peaks indicate we have identical intrinsic densities across varying ρ_0. 49

3.13 Plot of Linear modulus Y with nominal density ρ_0 for both spherical void scaffolds (in the density range of $0.50-0.34$) and cubical void scaffolds (rest of the range $0.30-0.069$). 49

3.14 log-log plot of Y vs ρ_0 for the figure in 3.13. Note that x-axis has been normalized by lowest nominal density $\rho_{min} = 0.069$. With slope $m = 1.2$ we have nearly linear scaling $Y \sim \rho_0^{1.201}$. 50

3.15 Shows the stress-strain response of $\rho_0 = 0.247 g/cc$ system having order parameter $S_2 \sim 0.8, 0.4$ and 0.0 with three different $r_c = 1.75\sigma, 1.50\sigma$ and 1.25σ when compressed in $\vec{z}$ direction. Also note, by $S_2 \sim 0.8$ we mean most of the rods are oriented strongly along the $\vec{z}$ direction (see figure2.11). Order parameter $S_2 \sim 0.4$ implies rods are oriented on average in the $\vec{z}$ direction but not strongly as $S_2 \sim 0.8$ (figure2.12). We follow this convention in the following discussions and for all the data we present. For system with $S_2 \sim 0$, rods are oriented randomly and the director of the phase should point approximately along $(1/\sqrt{3}, 1/\sqrt{3}, 1/\sqrt{3})$.

3.16 Stress-strain response of systems having nominal densities $\rho_0 = 0.212$ and $0.1 g/cc$ with cutoff $r_c = 1.25\sigma$ for three different order parameters. . 53

3.17 Top left: Shows stress response for $\rho_0 = 0.212 g/cc$ with $r_c = 1.50\sigma$. Reader can observe a lesser fluctuation compared to Figure3.16. Rest of the plots show the instantaneous stress-response for $S_2 \sim 0.8, 0.4$ and 0.0 with $r_c = 1.5\sigma$ having six different nominal densities (in units of g/cc) compressed in $\vec{z}$ direction as discussed in the Table2.3.2. 55

3.18 Plot of stress-strain response of various densities upon compression in both parallel(σ_{zz}) and perpendicular(σ_{xx}) direction to orientational direction($\vec{z}$) of rods. (Nominal densities ρ_0 are in g/cc) 58

3.19 Plot of stress response at a particular value S_2 compressed in $\vec{z}$ or $\vec{x}$ direction, having six different nominal densities(units in g/cc). 59

3.20 We show how the straight line fit was made to all the six plots in figure 3.19. In this plot, $S_2 \sim 0$ for all densities, we made a linear fit to initial regime using first 15 points for all the ρ_0. 60

3.21 Linear modulus Y plotted as a function of nominal density ρ_0 for six different cases: (a)$\sigma_{zz}(S_2 \sim 0.8)$, (b)$\sigma_{xx}(S_2 \sim 0.8)$, (c)$\sigma_{zz}(S_2 \sim 0.4)$, (d)$\sigma_{xx}(S_2 \sim 0.4)$, (e)$\sigma_{zz}(S_2 \sim 0.0)$, (f)$\sigma_{xx}(S_2 \sim 0.0)$. Note the x-axis has been normalized by the lowest density $\rho_{min} = 0.079 g/cc$. 61

3.22 log-log plot of Linear modulus Y as a function of nominal density ρ_0 for six different cases: (a)$\sigma_{zz}(S_2 \sim 0.8)$, (b)$\sigma_{xx}(S_2 \sim 0.8)$, (c)$\sigma_{zz}(S_2 \sim 0.4)$, (d)$\sigma_{xx}(S_2 \sim 0.4)$, (e)$\sigma_{zz}(S_2 \sim 0.0)$, (f)$\sigma_{xx}(S_2 \sim 0.0)$. Note that x axis has been normalized by lowest density $\rho_{min} = 0.079 g/cc$. Stress values are in LJ units. 62

A.1 The diagram helps to visualize the calculation of V_r(yellow region in this diagram). This schematic illuminates the size of a spherical void compared to the length $L\sigma/3$. We first calculate the volume of the grey region(V_r). 68

List of Tables

2.1 The table lists the values (a) The void volume fraction (b) The cubic box size before the compression. (c) The radius R_V of each of the 27 voids, (d) The total number of NPs used for the simulation. (e) The mean number of springs per NP (f) Lasts column lists the prepared nominal density of the system for different ϕ_V 18

2.2 The table lists the values (a) void volume fraction. (b)length of the simulation box (c) The total number of NPs used for the simulation. (d) The total number of springs in the system (e) Mean number of springs per NP (f) Intrinsic number density(ρ_I) (g) Nominal density (ρ_0) 24

2.3 The table lists the values (a) size of the simulation boxes for 6 cases considered (b) number of rods in the simulation box. (c)Nominal density in g/cc. (d)Three order parameters corresponding to a particular density i.e. 0.8, 0.4, and 0.0. (e)The total number of springs in the system. (f)Mean number of springs per rod. (g)Intrinsic particle volume fraction ϕ_I (h) void volume fraction of the system. (i)The thickness of the bridge Δ is suitably adjusted such that the number of rods are identical across 3 different order parameters for a given density. 31

3.1 The table lists the values (a) The radius of the spherical regions defined at 27 junctions. (b) The radius of the cylindrical regions (c) The nominal density after creating the voids. (d) The total number of nanoparticles (n_{Np}) (e) The total number of bonds interconnecting NPs in the system (f) Mean number of bonds per NP(N_B). 45

3.2 The table lists the values of slopes obtained in Y vs ρ_0 plots for all the cases 56

Chapter 1

Introduction

In the past few years, there has been growing interest in the preparation of novel materials that incorporate flexibility, rigidity, and toughness. Polymer Nanocomposites are one such class of materials that are being used in technologically demanding areas with numerous applications ranging from aerospace to electronic materials and from sensors to the food/bioprocessing industry. The applicability of these composites is enhanced by making them porous by containing void spaces, spaces not occupied by the constituent nanofillers and polymer matrix. The macroporous composites are less dense and can be tuned to have desirable mechanical, electrical, and thermal properties. Given the rapid advancement in nanotechnology of polymer nanocomposites, their properties have been widely investigated by researchers drawn from different disciplines([1],[2],[3],[4]). Porous materials which are prepared from only inorganic or glassy colloids are generally brittle and cannot even sustain strains on the order of a few percent and hence restricting its utility. For example, scaffolds of bonded glassy polymer particles, such as macroporous polystyrene foams, exhibit plastic responses beyond small strains. However, these hard inorganic particles can be combined with soft organic components such as polymers and cross-linkers rendering the scaffold elastic up to very large compressive strains.

Typically polymer nanocomposites refer to systems where a small fraction of nanofillers such as nanoclay, carbon nanotubes[5] or graphene[6] is added to the polymer matrix to enhance its functional properties such as stiffness, thermal properties and permeability[7]. The primary component by volume in a polymer nanocomposite is the polymer matrix and the major component by weight is the inorganic nanoparticles (upto 90%) with cross-linked polymers comprising the remaining 10% [8]. There is a separate class of porous polymer nanocomposites realized by ice-templating method. The walls (bridges and junctions) of such a structure are made of nano-particles ($\sim$ O nm)

crosslinked by polymer chains of similar length scales surrounding the micron-sized voids Figure1.1. These voids are inter-connected (open) hence giving the appearance of a foam.

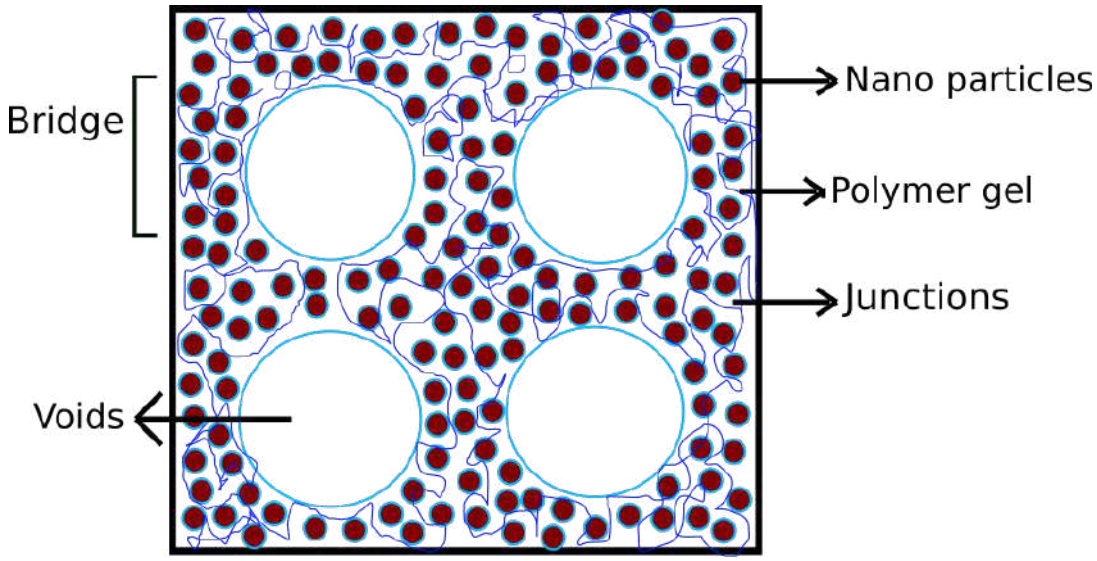


Figure 1.1: Diagram shows the schematic macroporous polymer nanocomposite.

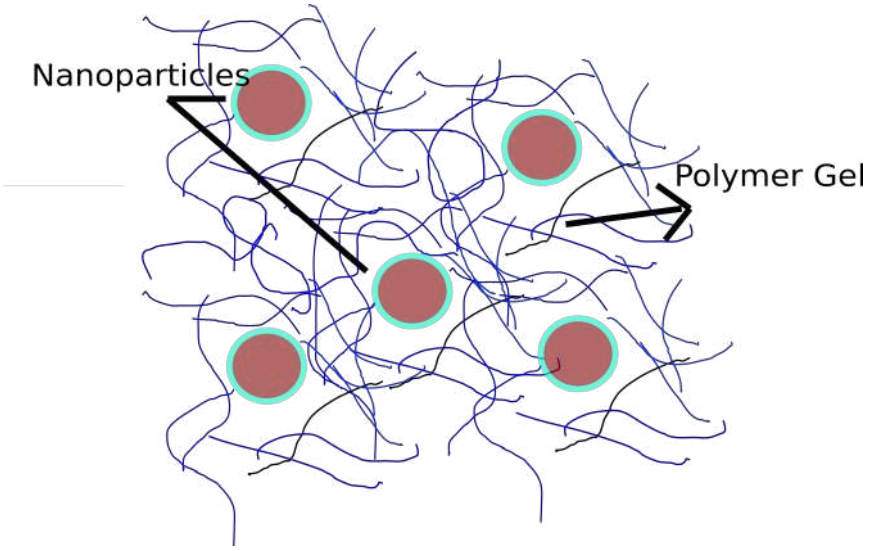


Figure 1.2: Zoomed in view of the above figure

Foams are naturally occurring as well as artificially synthesized (Figure 1.4). Man-made foams are common enough (Figure 1.3), open cell and closed cell polyurethane, aluminum honeycomb, copper, mullite, zirconia are a few examples. Some of the naturally occurring foams are cork, wood, sponge, corla bone, cuttlebone [9]. Some foams

have open cells (like a sponge) in which the material is distributed along the columns which make up the cell edges. Some foams are closed (like soap foam): the material is distributed in plates which forms the faces of the cells. These foams can also be distinguished based on directionality. Some foams are isotropic, meaning their structure and properties have no directionality. Most man-made foams are isotropic. Others are anisotropic. Most of the naturally occurring foams are open and anisotropic. A single piece of cork or bone differs in strength and stiffness by a factor of 2 or more along two directions at right angles. Wood is anisotropic still: many woods are 10 times stiffer and stronger when loaded along the grain than across it.[9]

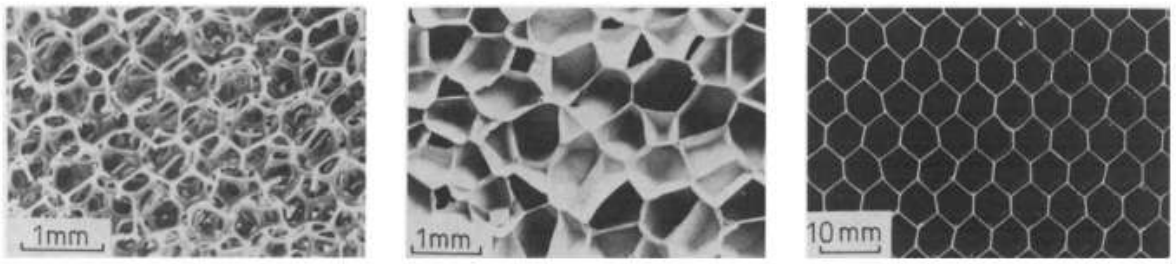


Figure 1.3: Man-made foams. From left: Open cell polyurethane, closed cell polyurethane, aluminum honeycomb. (Source: Reproduced from [9] with permission.)

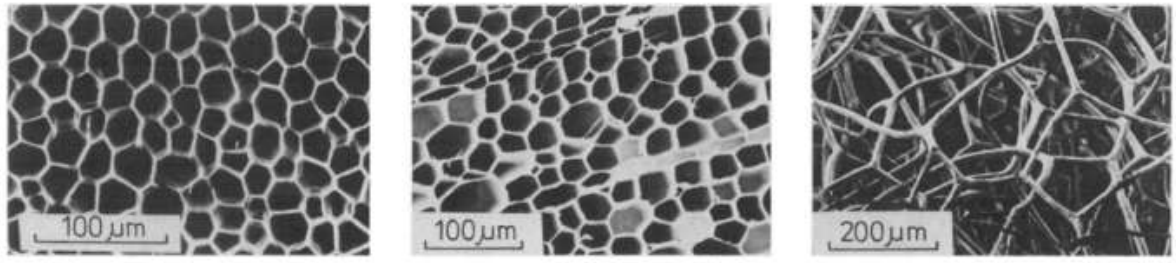


Figure 1.4: Naturally occurring foams. From left: Cork, wood, sponge. (Source: Reproduced from [9] with permission.)

Properties of polymer-nanocomposites are primarily determined by nanofiller chemistry, size, and shape of the nanofillers, amount of interfacial region available on nanofillers for the polymers to be adsorbed[10]. In addition filler-filler dispersed phase interactions mediated by polymer matrix also determines the properties of the hybrid([11]). It is the synergistic effect due to the combination of polymers with hard inorganic nanoparticles that imparts the scaffold amazing properties([12],[13]). Inorganic NP imparts rigidity and polymeric matrix imparts flexibility. Such materials show potential for several application such as fire-retardant foams[14], sponges capable of absorbing liquids with differ-

ent polarities[15], high surface area monoliths for catalytic reactions[16], as flexible capacitors[17],for use in environmental and energy application[18] as well as for use is artificial tissue with bio-medical relevance.

We are particularly interested in the mechanical response of PNC upon uniaxial compression. Earlier experimental work done by Ramamanickam et al.[19] demonstrated that such systems show elastic recovery[20][21] even after compressing up to one-0tenth of their original size inspite being comprised primarily of inorganic nanoparticles. A microscopic model was proposed to investigate the void deformation and stress response of such a system containing polymer networks with spherical nanoparticles and the plots/data matched with the experiment (Anish et al.[8]) We reproduce the major results of the model in this thesis. We also try to overcome the limitations of this model by working with cubical voids instead of spherical voids.

Of special interest are the nanocomposites consisting of ellipsoidal/rod-like particles instead of spherical particles[22]. Now the orientations of the rods and directional properties of the scaffolds cannot be ignored. The aspect ratio of the rod-like filler strongly influences the mechanical properties of the hybrid nanocomposites. Researches have reported an increase in the stiffness, strength,and heat distortion temperature with increase in the aspect ratio of fillers in nanocomposites([23],[24]). Preparation of nanocomposites containing ellipsoidal particles with an aspect ratio ranging from 1 to 4 has been reported (Guruswamy et al.[22]). Mechanical response of such nanocomposites has been shown to have complex non-trivial behavior whose microscopic detail is not understood. We aim to build a model which addresses these complexities and unravels the microscopic details of the system.

1.1 Thesis Outline

In the next section we give a brief overview of literature and how these macroporous monoliths are prepared in the experimental labs using the ice-templating method. For spherical fillers in the scaffold silica particles were used and for the scaffold containing anisotropic fillers, hematite particles were used([19],[22]). All the work related to experiments i.e. compression of scaffold using a rheometer, SEM images of monolith microstructure etc, were done in the lab of Dr. Guruswamy Kumaraswamy. In the next section we overview the properties of the monolith sponges upon compression using an ARES-G2 rheometer. The samples were also compressed (and then allowed to expand) in the rheometer and the normal forces exerted were measured. Small amplitude oscillatory measurements were also performed to measure shear modulus(G). SEM images of the scaffold displaying the local microstructure comprising fillers of varying aspect ra-

tios were taken using FESEM, INSPECT F50.[22]

In the section 1.5 we discuss the literature of entropic origin of the monolith modulus i,e. we explain why increased modulus with temperature was observed. We discuss how Young's modulus Y scales with nominal density ρ_0 of the scaffold for two cases: scaffold incorporating (a) spherical fillers and (b) anisotropic fillers. We end this chapter by discussing the qualitative change in the mechanical properties when the size of the fillers is changed.

In chapter-2, we discuss the coarse-grained minimalistic model investigated by Anish et al. In the next section we discuss why and how do we implement cubical voids and discuss their advantage. Next, we discuss how a rod particle was modelled in our simulation and how a simple WCA potential can be used for interaction between rods. We replace the spherical NPs with such rod-like particles. We prepare systems with three different order parameters for a particular nominal density, $S_2 \sim 0.8, 0.4, 0.0$. We discuss the procedure for creating cubical voids for scaffolds containing rod-like particles. In the next chapter, the results of Anish et al. were independently validated. We first compare stress responses for spherical and cubical voids scaffolds. Using cubical voids we were able to cover a decade range in the density of sponges and we obtain an approximately linear relationship between Y and ρ_0.

In the subsequent section we also obtain stress response for scaffolds with rods by uniaxial deformation in two directions for each of the $S_2 \sim 0.8, 0.4, 0.0$. The functional dependence of Y on ρ_0 was not linear anymore but we were not able to get quadratic scaling with AR ~ 4 rod particles as observed in experiments.
In chapter-4 we summarize our results and discuss some of the drawbacks and future perspectives of the model. We also discuss how some of the artefacts that we have encountered can be improved by further analysis.

The simulations, modelling, and analysis was conducted in the lab of Dr. Apratim Chatterji, by Somesh Kurahatti and Dr. Apratim Chatterji.

1.2 Motivation for this Thesis

Polymer nanocomposites are of potential industrial importance and have attracted significant research due to their wide-ranging application. The synergistic properties it possesses when its components are combined would not be possible by individual components. Computer simulation of such a system would allow better understanding of competing mechanisms which gives the stress-strain response. Careful engineering of

such materials will help us tune the properties to make things better. We focus on understanding the origins of the stress-strain response i.e. the role of individual components of the scaffolds upon compression. The simulation would be able to predict the properties of PNC or an outcome of an experiment without actually performing it. The Computer simulation of PNC allows better development of materials and would bring in rapid growth in PNC related nanotechnology.

In this thesis, we try to see the change in the property of nanocomposites when the spherical fillers are replaced with rod-like fillers with a particular aspect ratio. Through physics based computer simulation, we would be able to estimate many quantities of interest like yield strength, coefficient of thermal conductivity, many electrical properties, etc. for polymer nanocomposites.

1.3 The Ice Templating Method

There are many methods by which porous percolating monoliths can be prepared([25],[26]). Here we briefly review the known ice-templating method by which porous polymer nanocomposites are made. ([27],[28],[29],[30])

1.3.1 For Spherical Silica Particles

An aqueous solution of 1μ m silica particles, 0.5% of polyethylimine (mol wt: 25000 g/mol), and telechelic diepoxide cross-linker was prepared and frozen. Water in the aqueous solution is solidified. The growing ice force out and consolidates other constituents: silica particles, polymers, and cross-linkers to form the walls of the cellular solid. This hybrid particle-polymer network is left frozen for about a day allowing PEI to crosslink. After the walls aggregate ice is removed by dissolving it at a relatively high temperature (Figure1.5). After washing with excessive water to remove unreacted components what we obtain is self-standing macroporous sponge with open voids of size several micrometers interconnected by walls of approximately 1 μm thickness (Figure 1.6). Sponges that are centimeters in size can be prepared by this method.

Amine epoxy crosslinking is affected by several factors. These include amine concentration on the particle surface, chemical identity and concentration of epoxide in the crosslinker and finally reaction temperature and time. Low temperature slows the reaction rate by an order of magnitude. This is balanced by an increase in the local concentration of the crosslinking agent and amine.

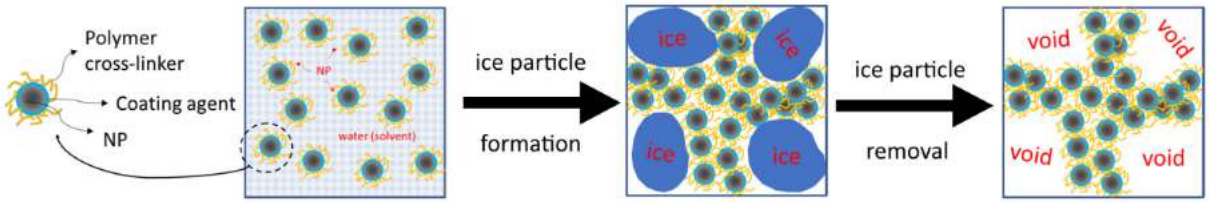


Figure 1.5: Schematic shows how the inorganic sponge is prepared. An aqueous solution of silica particles, polymers, and crosslinkers is frozen. These components are expelled by growing ice-crystals which consolidate to form the walls of the sponge. After the ice is removed we obtain a dry macroporous scaffold consisting of NPs enmeshed in the network of polymer.(Source: Reproduced from [8] with permission.)

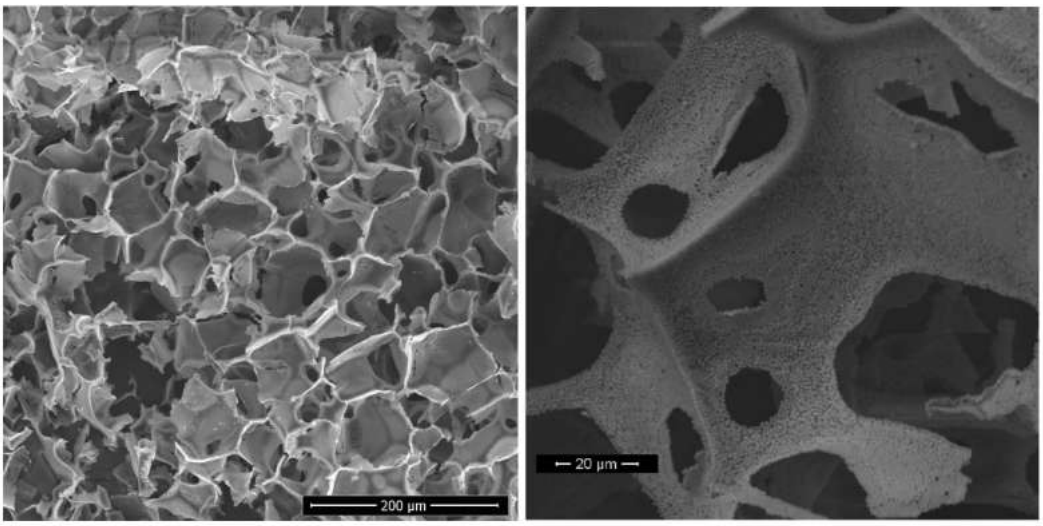


Figure 1.6: SEM images of the experimental system.(Source: Reproduced from [8] with due permission.)

1.3.2 For Anisotropic Hematite Particles

We discuss the preparation of macroporous nanocomposites incorporating anisotropic ellipsoidal particles with aspect ratio 2.2 and 4.0 using ice templating method[22]. We first prepare anisotropic hematite particles by hydrolysis of Fe^{3+}. The aspect ratio of hematite particles can be varied by adjusting the concentration of NaH_2PO_4.
In a typical preparation we add 3.54g of $Fe(ClO_4)_3$, 0.6g of urea and controlled amount of NaH_2PO_4 to 100 ml of milli Q water in 250ml pyrex bottle. The pyrex bottle is kept in a oven at 100°C for a day. Reaction product is segragated by centrifugation and is excessively washed with de-ionised distilled water until the pH of the supernatant is neutral.The structure of the hematite particles were confirmed by X-ray diffraction and size and shape of the hematite particles were identified by SEM images. By varying the concentration of Na_2HPO_4 hematite particles of aspect ratios 1.0,2.2,4.0 can be prepared (Figure1.7.)

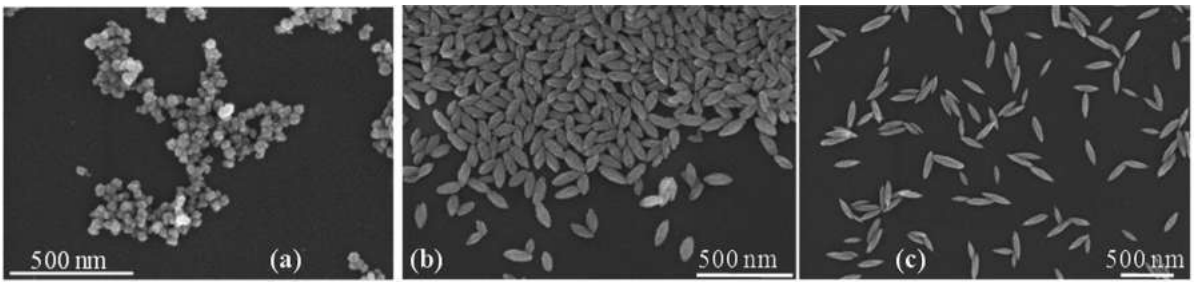


Figure 1.7: Scanning electron microscopy hematite particles of aspect ratio (a) 1.0 (b) 2.2 (c) 4.0 .(Source: Reproduced from [22] with due permission.)

Ice templated scaffolds can be prepared by adding hematite particle dispersion ($688\mu l$) weighing 60mg to 80 μl of PEI stock solution and rigorously mixed for about 10 mins using the vortex mixer. Next 8mg of $1,4$ Butanediol diglycydyl ether was added to this dispersion and vortexed for about 3 minutes. Mixture was then immediately transferred to the refrigerator (Figure 1.8)

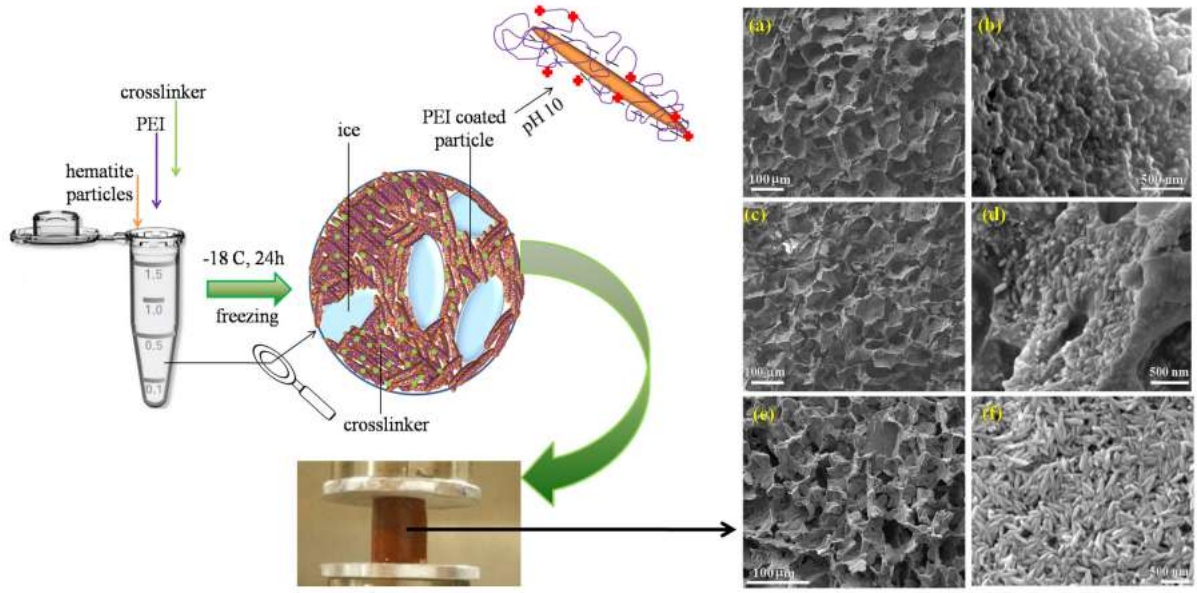


Figure 1.8: Schematic of scaffold preparation protocol and the scanning electron micrographs of scaffolds made of hematite particle with aspect ratios (a) and (b) $\sim$1, (c) and (d) $\sim$2.2, and (e) and (f) $\sim$4. (b), (d), and (f) are the high resolution SEM images of pore walls.(Source: Reproduced from [22] with due permission.)

Following the protocol for silica particles, the dispersion was frozen in centrifuge tubes by placing them in a freezer at $-18°$C for a day during which time PEI was crosslinked through the diepoxy to form a network. Subsequently, the samples were freeze dried. We obtain a dry macroporous scaffold whose walls are composed of anisotropic hematite particles 79% by weight enmeshed in a crosslinked PEI matrix

1.4 The Mechanical Response of Monolith to Compression

These Macroporous monoliths can be compressed up to strain values $\varepsilon = 85\%$ at room temperature and is able to recover completely to their original size upon releasing the strain. Water contained in the monolith was squeezed out during compression and was reabsorbed upon releasing the sponge. If the monolith is immersed in water for a few hours after compression, it completely recovers its original size.

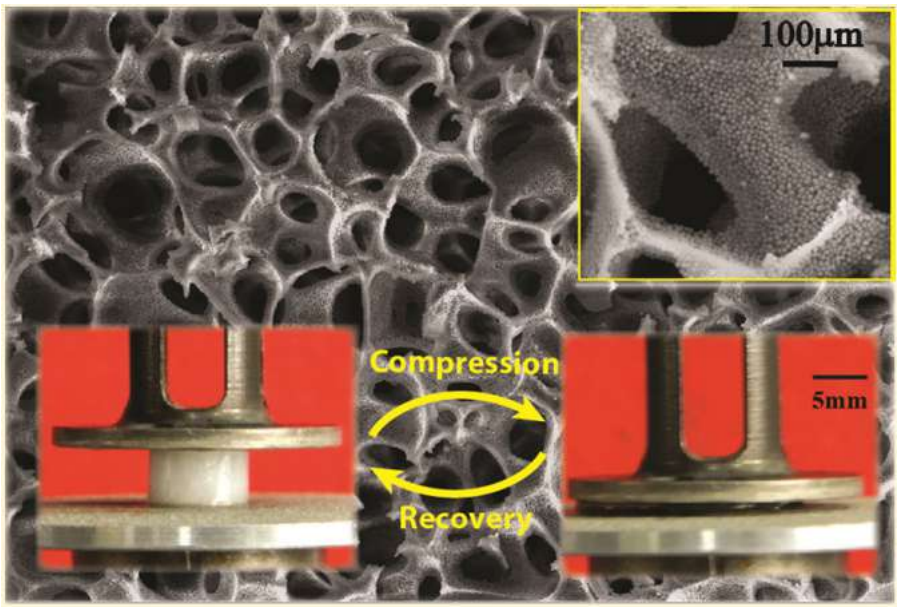


Figure 1.9: Elastic recovery is observed after compressing the scaffold upto 15% of its original size. Water is squeezed out during compression and reabsorbed as it regains its original size. (Source: Reproduced from [19] with due permission.)

The monolith has Young's Modulus approximately $E^* = 24000Pa$, significantly lower than typical values for porous materials prepared from inorganic or glassy particles. From the softness of the material at such a high loading of inorganic NPs, one can conclude that the modulus of the monolith is not determined by silica particles alone but arises from colloid polymer hybrid microstructure.
Stress measurements were made using a rheometer. Initially stress increased linearly with strain ε, plateaus at moderate strains values, and rapidly increases at high strains (Figure 1.10). The stress strain curve showed hysteresis in the compression-expansion cycle indicating the presence of dissipative forces(Figure 2 in [19]). There is no significant change in the lateral length of the cylindrical sample considered in the initial stages of compression Figure1.9. Hence these porous microstructures have unusually low values of Poisson ratio ν. A drastic increase in the stress response at high strains is due to densification of the monolith which correlates with the decrease in the size of the voids.

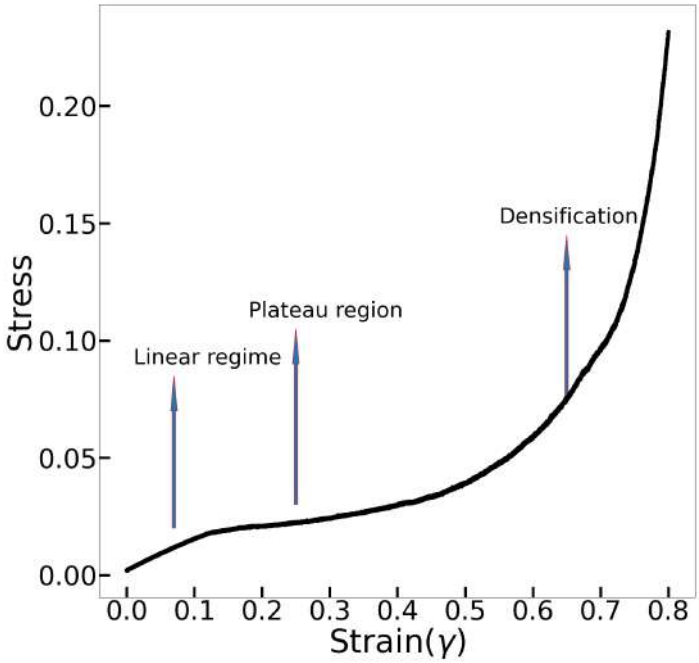


Figure 1.10: A schematic mechanical response of macroporous sponge upon uniaxial compression. Three distinct regions are demarcated.

1.5 Entropic Origin of Monolith Mechanical Response

An increase in the modulus with temperature was observed, indicative of the modulus being entropic in origin. Such behaviour is well known for polymeric rubbers. When polymeric rubber is deformed, the equilibrium end-to-end distance of the polymer strands changes. This generates a restoring force as fewer confirmation states are available. We can generalise this phenomenon as “restoring force increases when the temperature increase because more confirmations are available for polymers at high temperature”[19]

After compression colloid monolith exhibits elastic recovery only when swollen with a solvent. Measurement of G^*(Shear modulus) and E^*[1](Young’s modulus) for silica monoliths were performed over a temperature range of 20°C to 120°C using methanol, water, and DMSO as a solvent. An approximately linear increase of modulus with temperature was observed. Remarkably the mechanical response of monolith was independent of the solvent used. This independence of the mechanical response to solvent

[1]Here we use the symbol E^* for Young’s modulus to keep consistency with the source of the information, we use the symbol Y in Results and discussion section3.3

quality for the polymer suggests that the response is characteristic of the hybrid colloid/polymer architecture of the monolith rather than being merely from the crosslinked PEI.

The presence of solvent is important as it allows polymer connected colloids to have different confirmation space. Furthermore confirmation states in this monoliths must arise from rearrangement and relative motion between bonded colloids such that compression does not fracture the links connecting the particles. Although a fracture might be possible when the wall is heavily loaded with inorganic NPs.

1.6 Scaling Laws

These scaffolds can be prepared with different volume fractions (ϕ) of the silica paticles. SEM images of these scaffolds at different ϕ shows that pore size d scales inversely with particle fraction $d \sim \phi^{-1}$ (Figure 1.11). SEM images also show that average number density of pores $n \sim d^{-3}$ and the number density multiplied by approximate volume of a void as $nd^2t \sim \phi$[19]. This suggests that the wall thickness is independent of the volume fractions of silica particles.

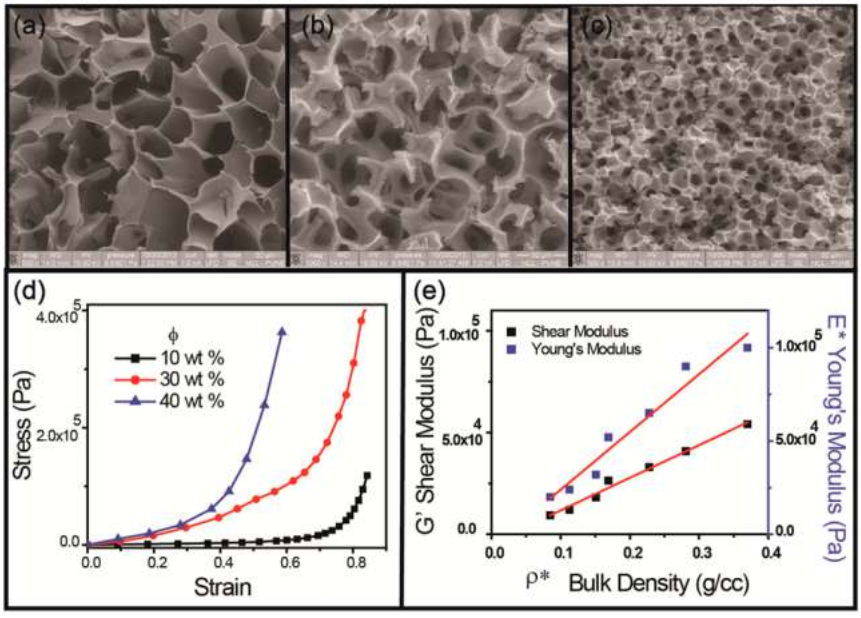


Figure 1.11: SEM image of $1\mu m$ silica scaffolds prepared by ice-templating. a) $\phi = 10\%$ b) $\phi = 30\%$ c) $\phi = 40\%$. d) Nominal stress strain data for scaffolds obtained by varying colloid fraction $\phi = 10\%, 30\%, 40\%$. e)Young's Modulus(E^*) and shear modulus(G^*) also varies linealy with monolith bulk density. (Source: Reproduced from [19] with due permission.)

For these ice templated scaffolds we also observe Young's modulus of the foam scales linearly with bulk density (ρ^*) of the scaffold. We also note that the ratio of the density of silica particles, cross-linkers, and PEI are held constant across different densities. It is a well-known fact that if the scaffold responds to strain by compression of the cell walls then elastic modulus scales linearly with ρ^*. If the cellular solid responds to compression by bending its cell walls rather than compression then moduli scale quadratically with bulk density (ρ^*). In fact for nanocomposites containing ellipsoidal particles walls respond by bending instead of compression which leads to scaling $E^* \sim (\rho^*)^2$ (Figure1.12).
For foams made up of carbon nanotubes even stronger scaling $E^* \sim (\rho^*)^3$ is observed[2]. For the walls to respond by compression, nanofillers must move relative to each other leading to change in the relative spacing of particles. For nanocomposites containing ellipsoidal particles, there is no significant change in the relative spacing of the particle as isotropic dispersion of elongated particles would be difficult.

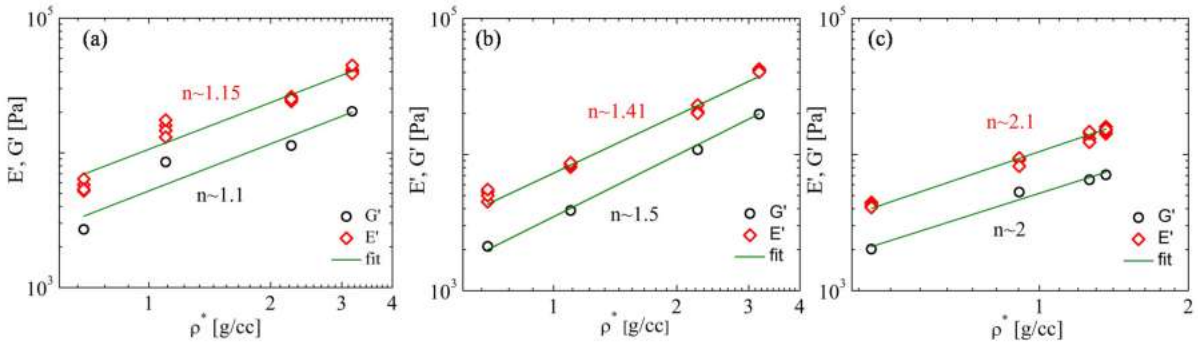


Figure 1.12: Storage and Young's moduli as a function of scaffold nominal density (ρ_0) for scaffolds made of hematite particles with aspect ratios (a) ~ 1, (b) ~ 2.2, and (c) ~ 4. (Source: Reproduced from [22] with due permission.)

1.7 Effect of Nanofiller Size and Shape

Size and shape of the nanofillers are the two most important parameters which determine the mechanical properties of the nanocomposites. The size and shape of the fillers are central in affecting the overall properties of the polymer nanocomposites: (a)surface to volume ratio, (b)excluded volume interaction.
A polymer nanocomposite offers a large surface-to-volume ratio as the constituents fillers are ($\sim O(nm)$) compared to the size of the scaffolds($\sim O(cm)$). This ratio indicates the amount of interfacial region compared to the bulk material. The interfacial region also affects new structural rearrangements on the molecular scale and is responsible

[2]We will change the notation for Young's modulus from E^* to Y in results and discussion section

for efficient stress transfer across the components[10]. Let us compare the surface-to-volume ratio for spherical and cylindrical fillers. For spherical particles with radius r, the surface to volume ratio of the filler is:

$$\frac{A_{sphere}}{V_{sphere}} = \frac{4\pi r^2}{(4/3)\pi r^3} = \frac{3}{r} \tag{1.1}$$

This relationship indicates available surface area A_S per unit volume of the filler V_S increases as the radius of the particle decreases. In a nanocomposite containing spherical particles with the filler volume fraction ϕ, the total interfacial area-to-volume ratio scales directly with ϕ, such that:

$$\frac{A_{sphere}}{V_{sphere}} = \frac{3\phi}{r} = SV_{sphere} \tag{1.2}$$

This relationship suggests, if we keep the filler volume fraction constant and decrease the radius of the filler, then the interfacial area available for the polymer matrix to be adsorbed on the surface filler increase. This leads to efficient stress transfer between the components of the nanocomposites. This relation also demonstrates, two composites having fillers of different radius, can have the same interfacial area if ϕ is suitably adjusted. Surface to volume ratio of the filler is determined by its shape. If fillers have the shape of a cylinder of radius r and length L then, the surface area to volume ratio is:

$$\frac{A_{cylinder}}{V_{cylinder}} = \frac{2\pi r^2 + 2\pi rL}{\pi r^2 L} = \frac{2}{r} + \frac{2}{L} = SV_{cylinder} \tag{1.3}$$

If we compare spherical and cylindrical fillers at equal volume fractions, we find the surface to volume ratio of a sphere compared to cylinder scales as:

$$\frac{SV_{sphere}}{SV_{cylinder}} = \frac{3/r}{(2/r) + (2/L)} = \frac{3}{2(1 + r/L)} \tag{1.4}$$

This relationship demonstrates for plates ($r > L$) and short rods ($L < 2r$) surface area to volume ratio for cylindrical fillers is greater compared to the sphere of radius r. Spherical fillers do have a greater surface-to-volume ratio for long rods ($L > 2r$). Rigid fillers are difficult to disperse isotropically at high void volume fractions. ”Therefore, the mechanical properties of non-isotropically dispersed fillers will likely be anisotropic”[10]. The difficulty of dispersing non-spherical fillers isotropically has been explored and is largely attributed to the excluded volume effect of rigid fillers and the ease of packing anisotropic fillers. Due to the excluded volume of rod fillers, a repulsive force develops due to the entropy of the filler objects. An important conclusion from excluded volume contributions is that high-aspect ratio fillers are increasingly difficult to diffuse isotropically as the aspect ratio L/r increases, as a result, ordered phases, similar to liquid crys-

talline transitions, will develop at lower filler volume fraction.

1.8 Response of Monolith is Chemistry Independent

Elastic recovery after large compression is observed for monoliths prepared with fillers of varying size and chemistry. Qualitatively the mechanical response by a monolith prepared by dispersion of 300nm silica particles is the same as the monolith prepared by a $1\mu m$ silica particles. Scaffolds prepared from 26nm silica particles also show qualitatively the same response. However smaller nanofillers have a large interfacial area. Rather surface to volume ratio of nanocomposites with small fillers is greater than nanocomposites with large fillers given both have the same particle fraction (ϕ). Due to the large interfacial area stress can be efficiently transferred through adsorbed chains segments at the filler surface. Therefore increasing the available interfacial area increases the quality of chain/filler interaction, rendering a high elastic modulus. Scaffolds obtained by varying molecular weight of crosslinked polymer also yield a quantitatively same behavior. Hence the response of the monolith is intrinsic to the preparation protocol and is independent of the specific chemistry involved.([19],[31])

Chapter 2

Computational Models and Methods

We describe a microscopic coarse-grained model proposed to describe the mechanical response of ice-templated nano-particle sponges. This minimalistic model captures the dynamics of sponge compression well despite of many simplifying assumptions[8]. A complete molecular description of the true hierarchical microstructure of the sponge is burdensome. Simulation of such an experimental system is multi-scale: $\sim O(1cm)$ porous sponge comprises $22nm$ silica NPs in a crosslinked PEI network forming $\sim O(10\mu m)$ thick walls surrounding $\sim O(100\mu m)$ pores. We have a description of how a solid open/closed cell foam responds to mechanical strain. We now describe the coarse-grained model which incorporates physics at several length scales in the system and also effectively captures the stress-strain response of the inorganic sponge.

To render the problem tractable we work with the idealized system where we replace silica particles enmeshed in a polymer gel with spherical beads interconnected by springs of the same spring constant. We also have large voids in their midst analogous to the experimental system. This coarse-grained model without the explicit modelling of polymers reproduces the stress-strain behavior observed in experiments to our satisfaction. Moreover, this model provides the microscopic dynamics of void deformation which was previously unavailable.[8]

2.1 Spherical Particles and Spherical Voids

We use non-equilibrium molecular dynamics as implemented by LAMMPS to realize our model for coarse-grained macroporous scaffolds. We use it to study the stress-strain response of the system to uni-axial compression. We model the inorganic sponge i.e. NPs trapped in a polymer gel network with large interconnected voids using a coarse-grained approach where we replace the polymer degrees of freedom with entropic springs. A brief overview of how we model the porous scaffolds is given in Figure 2.1. We do

not model the solvent effects.

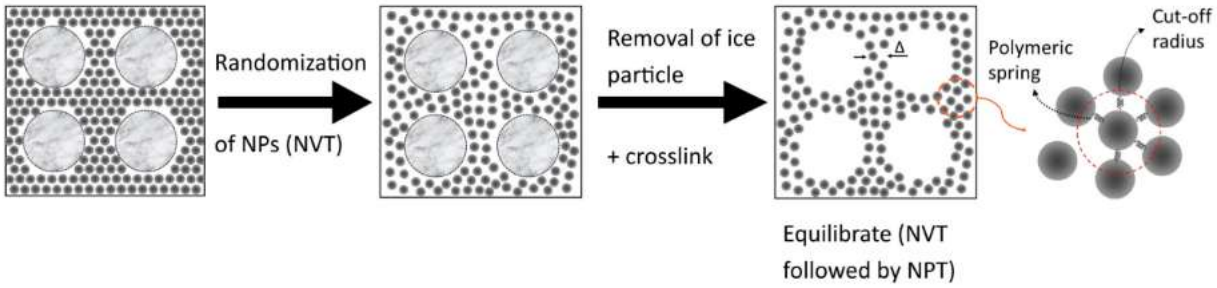


Figure 2.1: A schematic of how the inorganic sponge is prepared in our simulation model. Left box: The NPs are initialized in an FCC lattice surrounding 27 large spheres arranged in a $3 \times 3 \times 3$ cubic lattice where the grey spheres mimic ice-crystals. We implement excluded volume interaction between the NPs and the large grey spheres. We do not model the polymers in this step. Middlebox: After sufficient equilibration of NPs with large spheres in place we obtain a liquid-like short range order. Right box: We connect the NPs by springs with neighboring NPs; the spring network mimics the mesh of cross-linked polymers, which hold the NPs in place. Simultaneously the big spheres (which mimic the ice crystals) are removed from the simulation box such that voids remain. The NPs connected by springs (the NPs are enmeshed by the polymer gel in experiments) remain in position surrounding the voids, after which we do NVT and then NPT molecular dynamics simulations to prepare the system before applying uniaxial strain on the scaffold. (Source: Reproduced from [8] with due permission.)

1. *Initialization of particle positions and void positions*: In this step, we initialize the positions of all NPs on an FCC lattice in a simulation box of length $L\sigma$ and 27 large spheres in a cubic lattice of lattice constant $L\sigma/3$. Later the large spheres are removed to create the voids. NPs are perfect spherical beads of diameter $\sigma = 22nm$. The excluded volume interaction between NPs are modelled by the purely repulsive WCA potential. The WCA potential is a modified Lennard jones potential such that the cutoff of the potential is chosen to be $R_c = 2^{1/6}\sigma$. The form of the potential is:

$$V(r) = 4\varepsilon[(\sigma/r)^{12} - (\sigma/r)^6] + F_c r - V_c \quad \forall r < 2^{1/6}\sigma \tag{2.1}$$

where F_c and V_c are suitable shifted constants that ensure that the force and potential tend smoothly to zero at R_c. These NPs interact with large spheres with repulsive WCA potential such that they are excluded from their regions which mimic the ice crystals in our experiment.
the distance between centres of adjacent spheres were all the same $L\sigma/3$. The diameter of voids R_V was chosen to be larger than $L\sigma/3$ and was varied to achieve different void volume fraction ϕ_v. The large spheres do not interact with WCA potential and hence can overlap. The values of R_V, the initial box size ($L\sigma$), the corresponding void volume

fraction ϕ_V, the number of NPs $n_N P$ are listed in the table 2.1
Simulation box length L and value of R_V were suitable adjusted to achieve systems of different void volume fraction/nominal density, maintaining approximately same bridge thickness δ across different densities. We have relatively thicker junctions because we are working with spherical voids. In the next section we will prepare system with cubic-like voids to reduce the junction size. Snapshots of how we initialize the system in our simulation and how it looks after equilibration is given in the Figure 2.2 . In experiments the voids are arranged randomly in scaffolds and void volume fractionϕ_V can be as high as 0.9, which can be obtained with cubical voids.

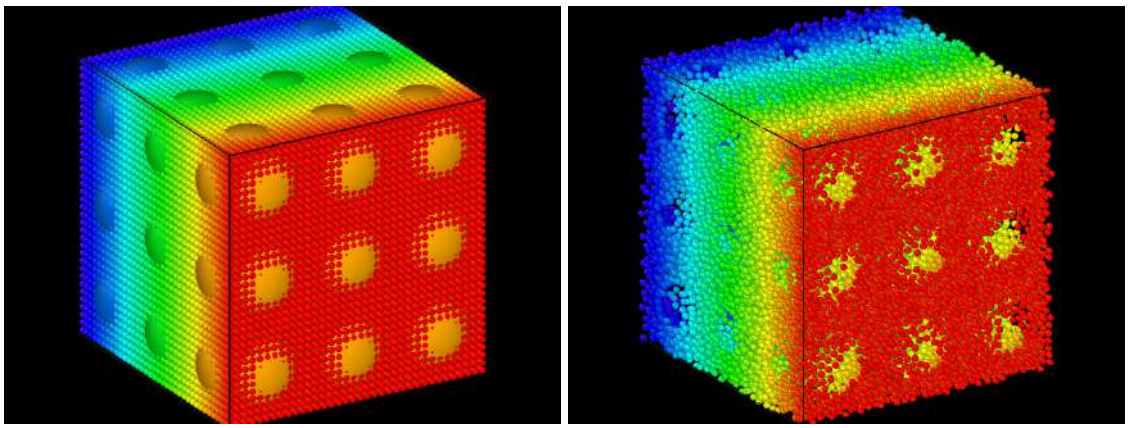


Figure 2.2: Left: Initiaization of NPs and large spheres. Right: After equilibration of NPs in the NVT ensemble

Before proceeding we would like to describe the meaning of some important terminologies.

- *Nominal density* (ρ_0): It is defined as the product of number density of silica particles n_{NP}/L^3 and mass of a silica particle m.

$$\rho_0 = \frac{n_{NP}\, m}{L^3}$$

- *Void volume fraction* (ϕ_V): The void volume fraction ϕ_V for the 27 voids in the simulation box is defined as the ratio of the volume occupied by all the voids V_V to the volume of the simulation box.

$$\phi_V = \frac{27\, V_V}{(L\sigma)^3}$$

  Since the diameter of the voids is greater than $L\sigma/3$, a part of the sphere pops out and overlaps with adjacent boxes leading to open voids. The void volume V_V is calculated by subtracting the volume of the voids outside the cube of $L\sigma/3$ from the volume of the large sphere.

- *Intrinsic number density* (ρ_I): The quantity that gives a measure of how tightly the NPs are packed, i.e ratio of n_{NP} and available volume for those NPs once the voids are removed.

$$\rho_I = \frac{n_{NP}}{(1-\phi_v)L^3}$$

  The value of this quantity has to be kept fixed across the systems with different void volume fraction ϕ_V. The value of this quantity is approximately $0.75-0.8$ for most of the nominal densities ρ_0.

- *Intrinsic particle volume fraction* (ϕ_I): The ratio of the amount of volume enclosed by fillers and available volume for fillers once the voids are removed. This is very useful quantity for scaffolds containing rod-like particles. This can also be understood as the product of ρ_I and the volume of a filler. For a spherical filler:

$$\phi_V = \frac{n_{NP}\, 4/3\pi(\sigma/2)^3}{(1-\phi_V)L^3}$$

ϕ_v	L(nm)	R_v(nm)	n_{NP}	N_B	N_S	$\rho_0(g/cc)$
0.55	1000(45.45σ)	170(7.73σ)	33323	10.383	173009	0.493
0.58	1000(45.45σ)	173(7.86σ)	30955	10.242	158535	0.458
0.6	1000(45.45σ)	175(7.95σ)	29018	10.0247	145449	0.429
0.64	1042(47.36σ)	187(8.5σ)	30358	10.080b	153005	0.397
0.66	1127.2(51.24σ)	205(9.32σ)	35650	10.028	179312	0.369
0.69	1230(55.9σ)	227(10.32σ)	43395	10.068	218460	0.345

Table 2.1: The table lists the values (a) The void volume fraction (b) The cubic box size before the compression. (c) The radius R_V of each of the 27 voids, (d) The total number of NPs used for the simulation. (e) The mean number of springs per NP (f) Lasts column lists the prepared nominal density of the system for different ϕ_V

2. *Melting the lattice of NPs*: We melt the FCC lattice before connecting springs to model the enmeshed NPs. We update the positions and velocities in the NVT-ensemble for 50,000 or more MD steps to melt the lattice with large spheres playing the role of ice crystals in place. The temperature was chosen to be $T_R = 300K$ and thus the unit of energy for these simulations is $k_B T_R = 1$. the mass m of NPs was chosen such that the mass-density of particles matched that of silica. Thus, $M = 14.8 \times 10^{-21}$kg for 22nm beads. The unit of time τ for the MD simulation has to conform to the relation $\tau = \sqrt{M\sigma^2/k_B T_R} = 4.15 \times 10^{-7}$s. The timestep for the integration was chosen to be 5 pico-seconds which is $1.2 \times 10^{-5}\tau$. At the end of equilibration we obtain liquid-like packing as the NPs diffuse from their initial positions over $50K$ MD steps. We show in Figure2.3 the cross-section of the system having $\rho_0 = 0.345 g/cc$

3. *Creation of NP − polymer mesh*: In this step we remove the large spheres of radius

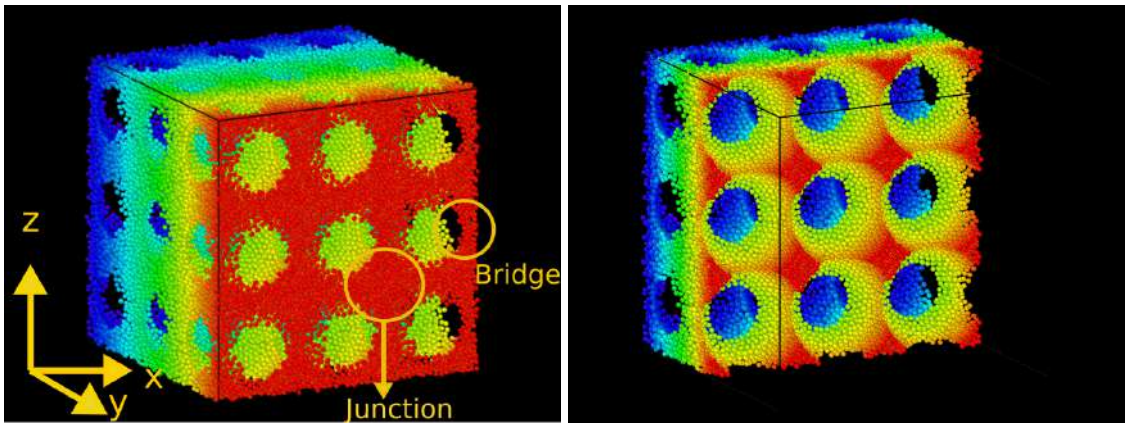


Figure 2.3: Left: Figure shows the image $\rho_0 = 0.345 g/cc$ system after equilibration. Right: Shows the cross-section of the same system.

R_V and all NP pairs which are within the cutoff distance $R_{CL} = 1.5\sigma$ were connected connected by harmonic springs. The form of the potential is $V_H(r) = \kappa_{CL}(r - r_{ij}^0)^2$ where r_{ij}^0 is the distance between neighbouring NP pairs i and j at the end of step 2. Each spring constitute the effects of cross-linked polymer, entrapping the NPs and preventing them from diffusing away. In our system soft-springs maintain the position constraint effected by the polymer mesh and at the same time allow NPs some freedom to move around its mean position. The equilibrium length r_{ij}^0 is different for each NP pair i and j but the spring constant will be same $\kappa_{CL} = 100 k_B T/\sigma^2$ for all springs.
By altering the value of R_{CL} we can change the mean number of connections per NP(N_B) in the system. Since a springs connects two NPs, N_B is given by $2N_S/n_{NP}$ where N_S is the total number of bonds shown in table 2.1. Also mean number of springs connections will be different for NPs in the bulk and for NPs surrounding the voids. Interested readers can find the results with $R_{CL} = 1.25\sigma$ and 1.5σ in [8] rendering different number of springs connections.
One needs to work with larger box sizes for systems with higher ϕ_V to maintain the same bridge thickness (Δ). This leads to change in the number of particle at interface compared to total number of NPs. This also results in larger number of particles at junctions. This problem can be resolved by working with cubical voids.
4. *Equilibration in NVT and NPT ensemble*: After connecting pairs of NP by springs, we first equilibrate the system in NVT ensemble for 10^5 iterations and calculate the equilibrium pressure P_1 of the system. Then fixing this equilibrium pressure, the system was equilibrated in a NPT ensemble for 10^5 iterations before the system is ready for compression.
5. *Applying strain*: Now we started applying a controlled strain along $\vec{x}$ direction and calculated the σ_{xx} component of the stress tensor in the NPT ensemble while the length of the simulation box decreased in the $\vec{x}$ direction. The pressure P_1 was maintained in the $\vec{y}$ and $\vec{z}$ direction using a Nose-Hoover barostat such that L_Y and L_Z could adjust itself.

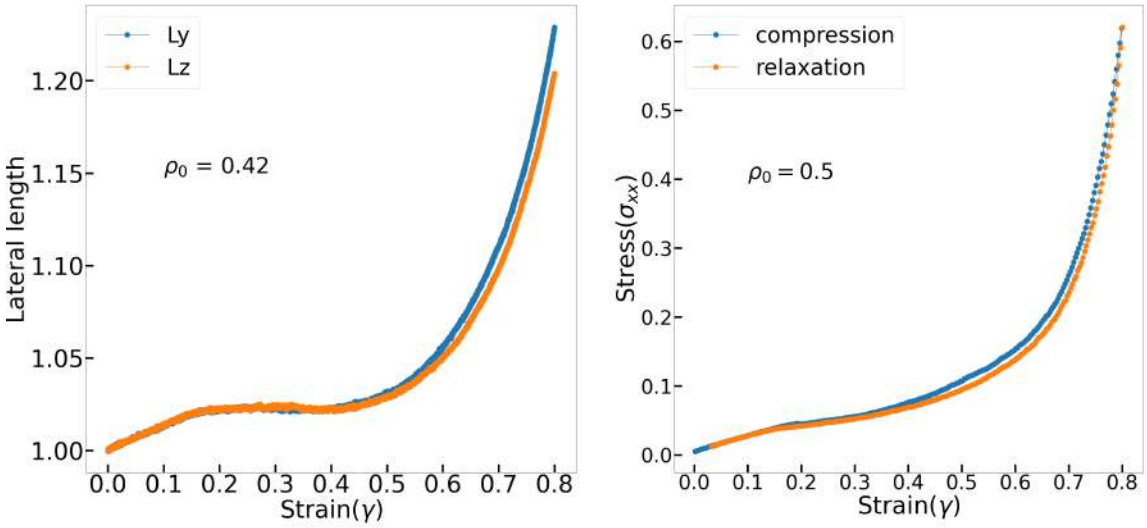


Figure 2.4: Left: The L_Y and L_z are plotted versus the strain γ. L_y , L_z increase linearly with γ in Regime-I, show a plateau regime in regime-II and start increasing from regime-III. Right: The figure shows the Stress-strain data during compression from 0 to 0.8, and relaxation from 0.8 to 0. (The nominal density (ρ_0) is in g/cc)

The pressure is calculated using a virial expression for the stress tensor$\sigma_{\alpha\beta}$ for pair of interacting particles i,j which are separated by $\vec{r}^{ij}$ with force $\vec{f}^{ij}$ acting between them, viz.

$$\sigma_{\alpha\beta} = \frac{1}{V}\left(m\sum_i v_\alpha^i v_\beta^i\right) + \frac{1}{2V}\sum_{i,j;i\neq j} r_\alpha^{ij} f_\beta^{ij} \tag{2.2}$$

where $\vec{v}$ is the velocity and the second summation should remind the reader that the summation is over values of particle pairs i, j when i $\neq$ j. The indices α,β take the values (x, y,z)[8]. The effect of compressing the sponge was investigated by gradually increasing the strain value from 0 to 0.8 over 24 million MD steps(288τ). Thus a sufficiently slow strain (1% strain applied in 3×10^5 time steps (3.6τ)) was applied to maintain the equilibrium. Also note that a harmonic springs with $\kappa = 100k_BT/\sigma^2$ and mass m equal to mass of a NP has a natural time period of oscillation comparable to unit of time: $2\pi\sqrt{\frac{M}{\kappa_{CL}}} \sim \tau$.
As the strain gradually increased, σ_{xx} component of the stress tensor was calculated. Nose-Hoover thermostat maintained the temperature of the system and Nose-Hoover barostat maintained the equilibrium pressure P_1 along $\vec{y}$ and $\vec{z}$ directions allowing corresponding dimensions of the box L_Y and L_Z fluctuate about the mean value Figure2.4.

Validation: Before we present our results and analysis, we comment on the robustness of our calculation. We compare the rate of compression in the experiment and in our simulation. A 1000nm sample was compressed to 200nm in the $\vec{x}$ direction within 288τ,

where the unit of time τ in our case was $4.15 \times 10^{-7}s$. Thus a compression of 800nm was achieved in $1.2 \times 10^{-4}s$. This corresponds to a compression rate of $\sim$1cm/sec, which is 10 times faster than the experimental rate. To establish the system was always close to equilibrium sample was compressed with 3 times faster and 3 times slower strain rate than the one mentioned above(supplementary [8]). Stress-response of the sample remains unchanged independent of nine-fold difference in compression rates. In addition five independent but statistically equivalent systems were created to ensure stress-response from straining the five systems are equivalent([8]. We also emphasize that 3×3 lattice of voids are minimally required in the system with periodic boundary conditions to ensure each bridge is connected with another non-identical bridge of NPs in all directions during deformation. This would not be possible if we choose to work with 2×2 lattice of voids.

To show that our results are consistent we first present some cross-checks. We show that our system is fully recoverable by the plotting compression and expansion curve in Figure 2.4. The value of stress tensor σ_{xx} is compared with stress response when the strain is released from 0.8 to 0.0 during expansion. We do not have viscous dissipation, hence stress response during compression and expansion are nearly the same. In reality, one can expect energy loss due to dissipation as polymers and NPs move past each other. We have relatively lower values of σ_{xx} during expansion because of the readjustment of particles over time to minimize energy and release of local constraint in the packed state. We also plot and compare potential energy density due to contribution from the extension of springs as well as the contribution from WCA interactions as the system is compressed in Figure2.5

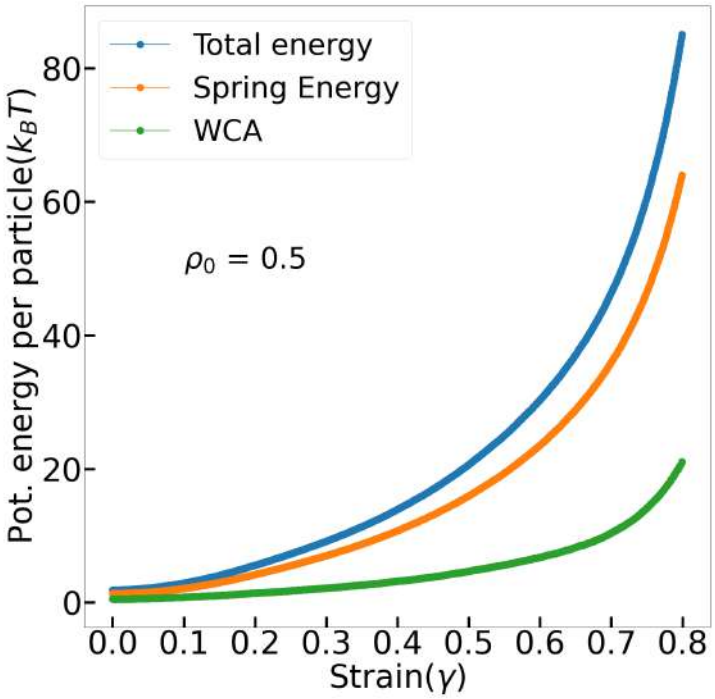


Figure 2.5: A plot of potential energy per particle(in k_BT units) as a function of strain.

2.2 Spherical Particles and Cubical Voids

When we compare our model for inorganic sponge with experimental system Figure 1.6, we observe that number of NP at the junction is unusually high. Also the thickness of the bridge(Δ) remains approximately constant between any two adjacent junctions in the experimental system. In our model, due to the artefact of using spherical voids, width of bridge is thinnest at the mid-point between any two junctions and gradually increases towards junctions

We found out in sections 1.6 that thickness of the wall/bridge is independent of the void volume fraction. This leads to inverse scaling of diameter of the voids with particle volume fraction $1 - \phi_V$ or direct scaling with void volume fraction $R_V \sim \phi_V$. As a consequence we had to work with bigger simulation box length so that we can increase the void volume fraction and at the same time keep the minimum thickness of the bridge Δ nearly constant across systems of different void volume fractions. Figure2.6 shows the images of the systems having cubical voids in which we have kept the thickness Δ of the bridge(Δ) constant across the system. Also note the increasing size of the simulation boxes and size of the voids as we achieve less denser system.

Increasing box length with large spheres to model spherical voids aggregates a great amount of NP at junctions. These big junctions dominate the stress-strain response when the sponge is compressed. Consequently we decided to work with cubical voids instead

of spherical voids. This leads to homogeneous distribution of particles in junctions and bridges.

2.2.1 Procedure for creating cubical voids

1. *Initializations of NP positions and equilibrations*: To begin with we follow similar procedures as established in section 2.1 viz. We initialize the positions of all the NPs on an FCC lattice in the simulation box of length $L\sigma$ along with large spheres of radius R_V in a cubic lattice with lattice constant $L\sigma/3$. Since we are interested in sponges with higher volume fractions we are choosing bigger simulations boxes with sufficiently large spheres placed in them forming open interconnected voids.
Now we melt the lattice by equilibration in NVT ensemble for 1L to 2L MD timesteps depending on the size of the simulation box. To melt the lattice of NPs in a larger simulation box with large junctions we needed to equilibrate the system for a longer time and at a higher temperature. After initial equilibration to melt the lattice we ensured values values of intrinsic number density $\rho_I = n_{NP}/(1-\phi_V)L^3$ remains approximately same as kept in previous section 2.1. This is essential because the response of the two systems with the same nominal density ρ_0 but different void volume fractions ϕ_V would be different. The system with higher volume fractions would be more tightly packed than the system with lower void volume fractions. This increases the number of bonds per NP (N_B) leading to a sharper initial response to compression for system with higher ϕ_V.

2. *Defining regions and retaining NPs*: We make cubical-looking voids after melting (liquid-like packing of NPs) by retaining those NPs whose centers are within the specified region and deleting other NPs which are outside the specified region. As shown in the Figure2.7 we defined 16 cylindrical regions for a pair of opposite faces in the XY plane of the simulation box. The length of all the cylindrical regions is the same as the length of the simulation box and their axes are perpendicular to the XY plane. Out of these 16 cylinders, there are 4 cylinders whose centers are located inside the face of the box and their volume is completely immersed inside the box, 8 cylinders on the edge of the face have half of their volume inside the box and 4 cylinders whose centers are located at corners have a quarter of their volume common with simulation box. We continue defining such a set of 16 cylinders for the other two pairs of opposite faces. The axes of the cylindrical regions defined for the opposite faces in the YZ plane are parallel to the X-axis and similarly for faces in the XZ plane, cylindrical axes are parallel to the Y-axis.
There are in total 48 cylindrical regions defined in the simulation box of length L with the radius of each r_S. Taking periodic boundary into account there are 27 junctions where these cylinders meet and 81 cylinders of length $\frac{L-6R}{3}$. Details can be found in the ap-

pendix sectionA.1. Figure2.8 shows the system with $\phi_V = 0.86$ before and after removing the NPs. The volume of the orthogonal intersection of two cylinders of radius R is given by $16R^3/3$. The NPs whose centers are located inside this defined region are retained and NPs located outside this region are simply deleted. We keep the radius of the cylinders same for systems with different void volume fraction/nominal density akin to the experimentally prepared inorganic sponges of different particle fractions The void volume fraction for our system is given by:

$$\begin{aligned}\phi_v &= 1 - \frac{Vol.\ of\ the\ cylindrical\ region}{Vol.\ of\ the\ simulation\ box} \\ &= 1 - \left[\frac{27 \times \frac{16R^3}{3} + 81\pi R^2(\frac{L-6R}{3})}{L^3}\right] \\ &= 1 - \left(\frac{144R^3 + 27\pi R^2(L-6R)}{L^3}\right)\end{aligned} \tag{2.3}$$

We also note that amount of volume covered by n_{NP} NPs to the available volume after creating voids $(1-\phi_v)L^3$ was about 0.41 for all of the Anish et al. cases in section2.1 and all the cases considered in the table.

ϕ_v	L(nm)	n_{NP}	N_S	N_B	ρ_I	$\rho_0(g/cc)$
0.69	13770(62.59σ)	54245	281277	10.37	0.72	0.342
0.714	14300(65σ)	58574	309469	10.56	0.74	0.296
0.76	16000(72.73σ)	70071	382552	10.91	0.75	0.253
0.787	17150(77.95σ)	75971	410767	10.81	0.76	0.223
0.81	18400(83.63σ)	84457	461783	10.93	0.76	0.199
0.83	19450(88.41σ)	92598	514756	11.11	0.78	0.186
0.86	21800(99.1σ)	105801	583773	11.03	0.77	0.151
0.88	24480(111.27σ)	119703	654282	10.93	0.73	0.120
0.905	27200(123.63σ)	132871	717822	10.80	0.74	0.097
0.92	29700(135σ)	152796	846491	11.08	0.77	0.086
0.93	33100(150.45σ)	169094	923924	10.92	0.71	0.069

Table 2.2: The table lists the values (a) void volume fraction. (b)length of the simulation box (c) The total number of NPs used for the simulation. (d) The total number of springs in the system (e) Mean number of springs per NP (f) Intrinsic number density(ρ_I) (g) Nominal density (ρ_0)

3. *Connecting springs and applying strain*: Once we remove the NPs outside the region, we connect the springs between NPs, viz. all NPs whose centers are within the cutoff distance $R_{CL} = 1.5\sigma$ from each other are connected by harmonic springs. Sufficient NVT equilibration was done for all the systems such that equilibrium pressure at the end of NVT equilibration, converges and fluctuates about some mean value. After subsequent NPT equilibration the system is ready to be compressed. The parameters like rate

of deformation, the frequency at which barostat and thermostat are called, MD timestep, and the total number of iterations were kept the same.

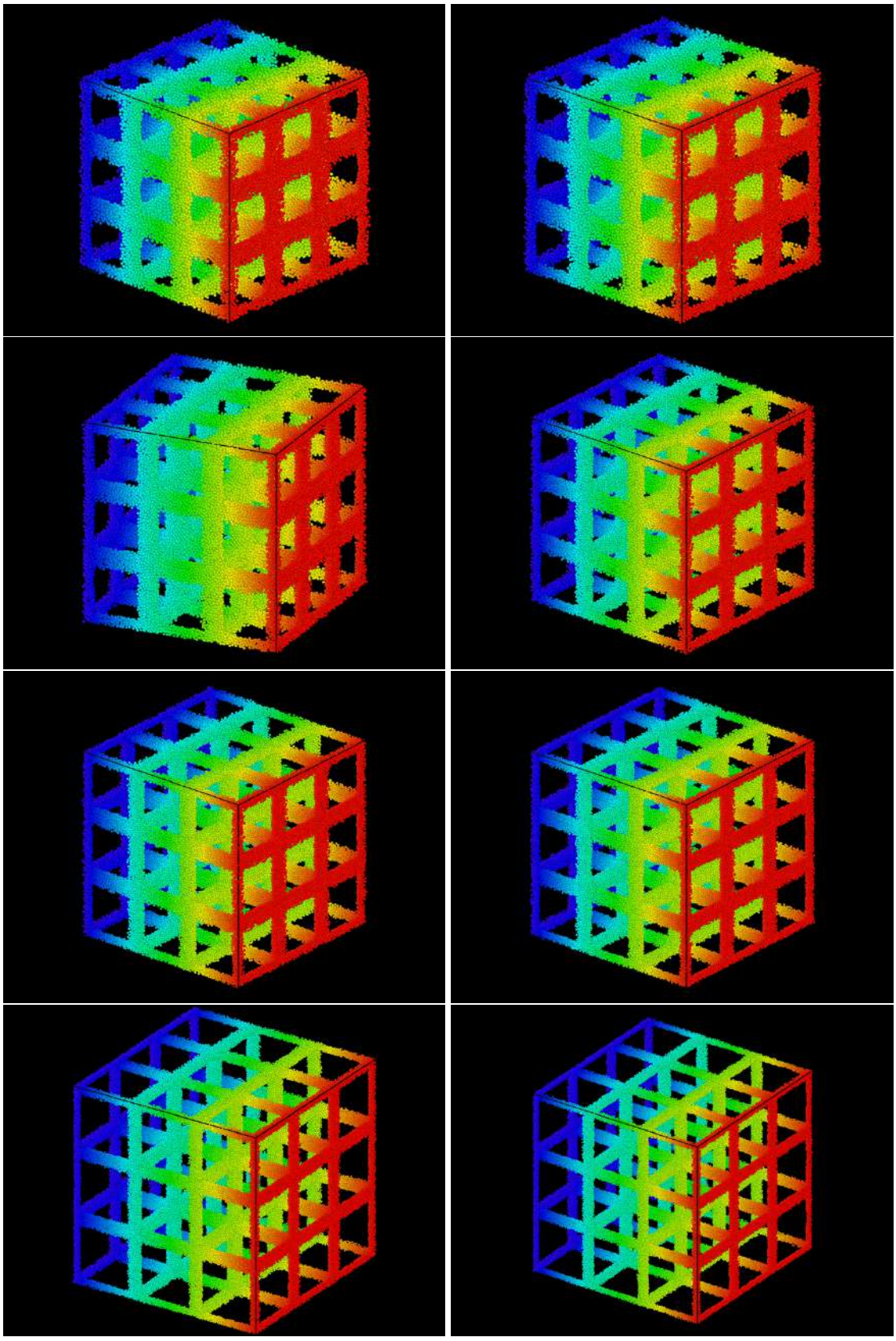


Figure 2.6: Shows the images of the system having densities $\rho_0 = 0.307, 0.296, 0.253, 0.223, 0.199, 0.186, 0.121, 0.0977$ from top to bottom. The densities are in g/cc. Note the increase in pore size as the length of the simulation box increases while the bridge thickness Δ remains constant across different densities.

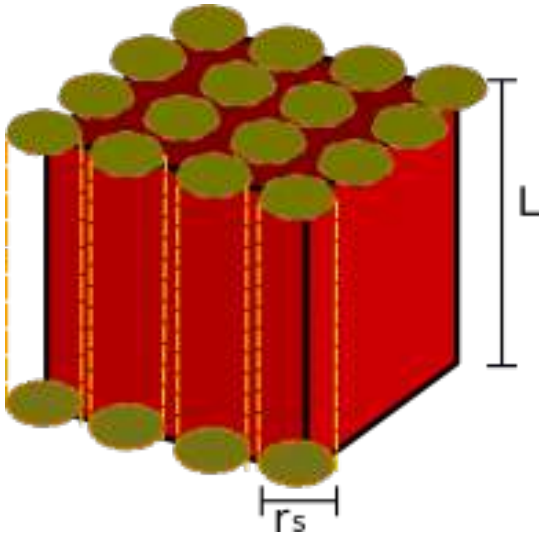


Figure 2.7: Nanoparticles whose centers are located within the defined cylindrical regions of radius r_S and length $L\sigma$ in the simulation box as shown in the figure are retained. There are 16 cylindrical regions defined between a pair of opposite faces and hence we define a total of 48 such cylindrical regions in the simulation box. The NPs whose centers are not located inside the union of 48 cylindrical regions, are simply deleted.

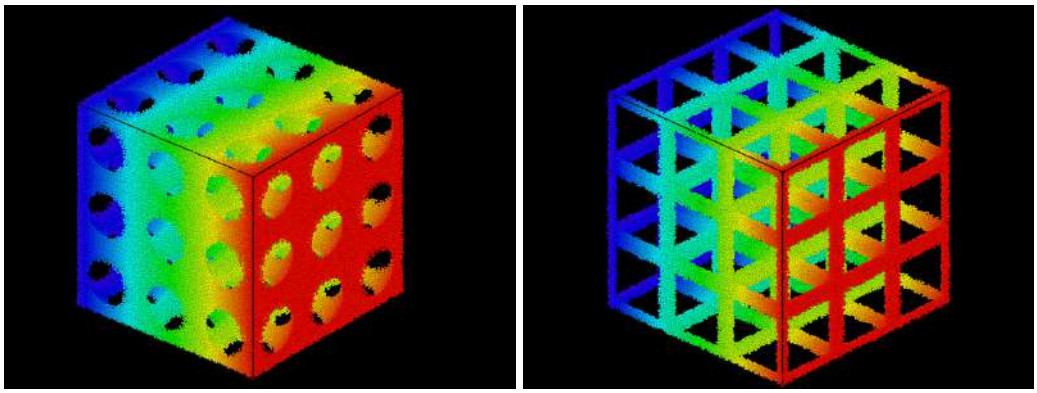


Figure 2.8: Left: Shows the $\phi_v = 0.86$ system before removing the NPs by defining cylindrical regions. Right: After removing the NPs.

2.3 Modelling Rod-like Particles

We are particularly interested in the stress response of inorganic sponges when the spherical beads are replaced by anisotropic rod-like particles. The aspect ratio of the rod strongly influences its mechanical response. If the sponge is composed of ellipsoidal particles, we have to implement complicated potentials like Gay-Berne or ReSquared. We now describe how the rod-like particles were modelled in our simulation using simple WCA potential to model the interaction between rods.

2.3.1 Details of Modelling

A rod-like particle was built using spherical beads viz. depending on the aspect ratio of interest we linearly connect NPs with a very high spring constant. We also implement a three-body potential to make the rod rigid for every 3 adjacent beads in a rod. For example, we build a rod by connecting four beads as shown in the Figure2.9 with a harmonic potential of a very high spring constant between adjacent beads, we define 3 body angle potential between (1,2,3) and (2,3,4) numbered beads. The form of the potential is:

$$V(\theta) = \varepsilon_b cos(\theta) \tag{2.4}$$

where θ is the angle formed by 3 adjoining NPs in a rod, If the value of θ is π, beads are aligned linearly and the energy is minimized. If we use very high values of ε_b, the bending of rods will be energetically unfavourable. A very high spring constant in the harmonic potential defined between adjacent beads restricts oscillations about their mean position.
We construct such rods by combining 4 NPs of radius 0.8σ with the equilibrium length of the spring σ. NPs in a rod interacts with NPs in another rod by WCA potential with $R_c = 2^{1/6}(0.8\sigma) = 0.8979\sigma$. It is essential that we keep the length of intra springs in a rod longer than the diameter of the NP , so that adjacent NPs do not interact. Now we are ready to replace all the spherical particle in a sponge by such type of rigid rods and study the change in its response.

2.3.2 Creating Cubical Voids for System with Rod-like particles

Initialization: We initialize the system by placing all the rods oriented in the Z-direction perfectly along with 27 large spheres in a simulation box. Rods that overlap with large spheres are deleted. We also define WCA interaction between the NPs such that particles within the rod do not interact. WCA potential between large spheres and rods is also defined with suitable parameters such that rods are expelled from their region which mimics ice-crystals. Since these are anisotropic particles their orientation cannot be ig-

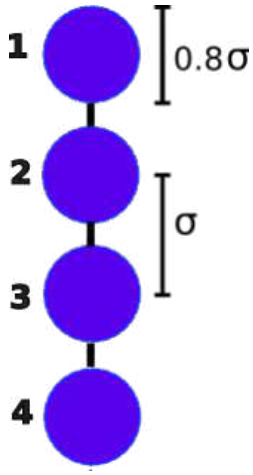


Figure 2.9: Constructing a rod-like particle by connecting spherical particles in a linear fashion. Here the aspect ratio is 4.75.

nored.

To quantify the magnitude of orientation in a particular direction we define the order parameter S_2. This quantity can be calculated by first finding out the average orientation of the vectors associated with each of the rods. This is also called the director of the phase. then we compute the statistically averaged quantity $\frac{3\cos^2\theta-1}{2}$ for all the rods, where θ is the angle made by a rod with the director. This quantity can also be time-averaged(if needed) to get the averaged order parameter. When $\theta = 0$(perfect alignment of all the rods along the director), the value of the order parameter is 1.0

We prepare systems with 3 different order parameter $S_2 \sim 0.8, 0.4, 0.0$ before connecting springs and applying strain. Similar to sponges with spherical nanoparticles we are interested in higher void volume fraction keeping the thickness of the bridge (Δ) constant between the junctions. Again we conform to defining regions and retaining the rods if the centers of all the NPs in a rod are inside the region and deleting the rest of the rods. If the center of any particle in a rod is located outside the defined region, the whole rod is deleted.

The perfectly aligned lattice of rods is melted in the NVT ensemble at a high temperature with a varying number of MD steps depending on the order parameter of the system to be prepared and the size of the simulation box. For example, systems with large simulation boxes have a lot of rods accumulated at the junctions after creating spherical voids. Rods that are located deep inside the junctions take a longer time to equilibrate. Since we start with an ordered system we need to equilibrate for a very long time at a high temperature to get the isotropic phase.

Since we have chosen the diameter of bead in a rod to be 0.8σ, the volume of this bead is approximately half the volume of a NP in a sponge with spherical NPs in section 2.1. As a consequence, if we consider two systems (a) sponge with spherical NPs and (b) sponge having rod-like particles such that both have the same particle volume fraction,

then we must have more beads in (b) than the NPs in (a).

Equilibration: We melt the lattice at a higher temperature since the anisotropic particles can easily form stable phases even at low particle volume fractions. Larger simulation boxes were melted at even higher temperatures because rods located deep inside the junction remained aligned even after long iterations. We prepare the system of different order parameter by varying the number of iterations in initial NVT equilibrations to melt the lattice. A shorter NVT run will prepare the system of order parameter $S_2 = 0.8$, a relatively longer run prepares systems with $S_2 = 0.4$ and very long equilibration will produce isotropic phase. System with $S_2 = 0.8$ will not be a stable phase as it starts to loose order parameter even at room temperature. This is because of our approximation for rod-like particle and also packing fraction is insufficient to form nematic phases. The amount of volume excluded by a rod particle in our simulation is smaller than the volume excluded by a perfect rod-like particle or ellipsoidal particle of similar dimensions.

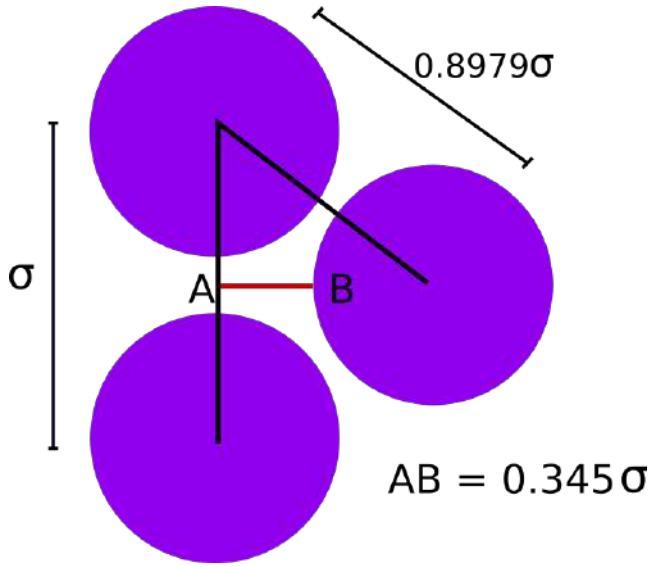


Figure 2.10: The maximum distance upto which a bead of another rod can come between a pair of adjacent beads(left) is AB = 0.345.

To calculate the particle volume fraction for the sponges with rod particles, we make an assumption in which we treat our rod of length 3.8σ and radius 0.8σ as a cylinder of similar dimension. This is valid as most of the volume between the particles in a rod would be excluded (see Figure 2.10) and we make sure that particles volume fraction for our fist case with $L = 48\sigma$ in table 2.3.2 is similar to fourth case of table 2.1 in section 2.1 which also has $L = 47.36\sigma$ albeit void volume fraction of latter($\phi_V = 0.5$) is less compared to former($\phi_V = 0.64$).

$$\frac{30180 \times 4/3 \times \pi \times (0.5^3)}{47.38^3} \sim \frac{(38532/4) \times \pi \times 0.4^2 \times 3.8}{48^3} \sim 0.15$$

L	n_{rods}	ρ_0	S_2	N_S	N_B	ϕ_I	ϕ_V	$\Delta = 2b(\sigma)$
48σ	9633	0.247	0.8	254939	52.93	0.33	0.5	8.0
			0.4	223309	46.363	0.263	0.367	9.428
			0.0	218728	45.41	0.262	0.366	9.438
60σ	16106	0.212	0.8	398278	49.45	0.40	0.648	8.0
			0.4	329499	40.91	0.3	0.524	9.68
			0.0	325498	40.42	0.3	0.524	9.67
72σ	21832	0.166	0.8	528317	48.4	0.43	0.740	8.0
			0.4	444444	40.715	0.327	0.658	9.422
			0.0	416663	38.17	0.311	0.64	9.717
84σ	26324	0.126	0.8	611949	46.49	0.427	0.801	8.0
			0.4	528036	40.12	0.34	0.75	9.112
			0.0	511443	38.88	0.327	0.744	9.266
96σ	31114	0.1	0.8	714678	45.94	0.43	0.84	8.0
			0.4	586263	37.69	0.32	0.79	9.41
			0.0	583105	37.48	0.32	0.79	9.44
108σ	35277	0.079	0.8	798832	45.23	0.423	0.87	8.0
			0.4	656864	37.24	0.317	0.831	9.383
			0.0	645445	36.6	0.31	0.827	9.514

Table 2.3: The table lists the values (a) size of the simulation boxes for 6 cases considered (b) number of rods in the simulation box. (c)Nominal density in g/cc. (d)Three order parameters corresponding to a particular density i.e. 0.8, 0.4, and 0.0. (e)The total number of springs in the system. (f)Mean number of springs per rod. (g)Intrinsic particle volume fraction ϕ_I (h) void volume fraction of the system. (i)The thickness of the bridge Δ is suitably adjusted such that the number of rods are identical across 3 different order parameters for a given density.

This is an important step to ensure as it explains why we need to have 38532 beads (9633 rods) for scaffolds with rod-like particles relative to 30180 NPs in inorganic sponges.Note that we have used the intrinsic volume fraction formula for rod-like particles in the table 2.3.2:

$$\phi_I = \frac{n_{rods}\pi(0.4\sigma)^2 3.8\sigma}{(1-\phi_V)L^3}$$

Defining Cuboidal region: The thickness of the bridges were kept same across different densities by defining cubical regions in the same way defined cylindrical regions for spherical particles. We have chosen to work with cuboidal region as length of the rods is comparable to thickness of the bridge. A rod is retained if the centers of all the beads are located inside the region. Rods located outside the regions are deleted. Thickness of the bridge(Δ) was 8σ for systems with $S_2 \sim 0.8$ and δ was suitably adjusted for $S_2 \sim 0.4$ and 0.0 such that we maintain same nominal density (ρ_0) across different S_2. In figure 2.11,2.12,2.13 we show the images of $\rho_0 = 0.247 g/cc$ system having $S_2 = 0.8, 0.4, 0.0$ from all possible angle of view

Similar to the sponges with spherical particles we defined 48 cuboidal regions of length equal to the length of simulation box and breadth $2b$. Also we have 81 cuboids of length

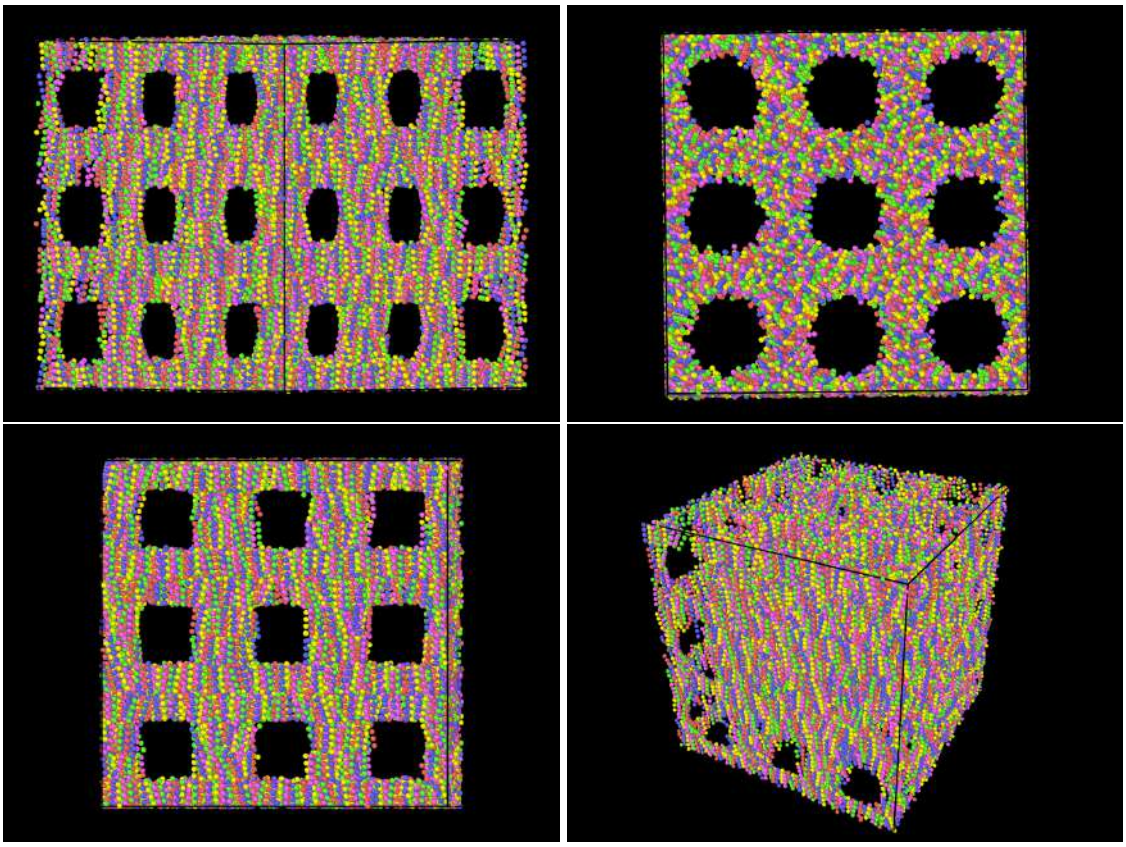


Figure 2.11: Shows the images of the system $\rho_0 = 0.247g/cc$ having order parameter $S_2 \sim 0.8$ for all possible angle of view. There is an artefact in designing this $\rho_0 = 0.247g/cc$ system leading to the appearence of spherical voids(top right image), that will be corrected in the final submission.

$\frac{L-2b}{3}$ and 27 junctions taking PBC into account. Volume of orthogonal intersections of two cuboids is $(2b)^3$ and breadth of the cuboid 2b was kept same across different densities having $S_2 \sim 0.8$ was carefully increased such that we have identical number of rods across for all three cases $S_2 \sim 0.8, 0.4, 0.0$. Void volume fraction can be calculated as follows:

$$\begin{aligned} \phi_v &= 1 - \frac{Vol.\ of\ the\ cuboidal\ region}{Vol.\ of\ the\ simulation\ box} \\ &= 1 - \left[\frac{27 \times (2R)^3 + 81 \times (2b)(2b)(\frac{L-6b}{3})}{L^3}\right] \\ &= 1 - \left(\frac{216b^3 + 81b^2(L-6b)}{L^3}\right) \end{aligned} \tag{2.5}$$

In Table2.3.2 we calculated nominal density by assuming all the beads have a mass 0.512 times the mass of a NP in section 3.1 as Vol. of a bead $\sim$ $0.512\times$ Vol. of a NP. Hence $\rho_0 = 0.512(mn_{beads}/L^3)$ where n_{beads} is the total number of beads. In table 2.1 we kept the value of volume occupied by the n_{NP} particles to the available volume after creating voids $(1-\phi_V)L^3$ in the range $0.4-0.42$. Similar range of values were kept for

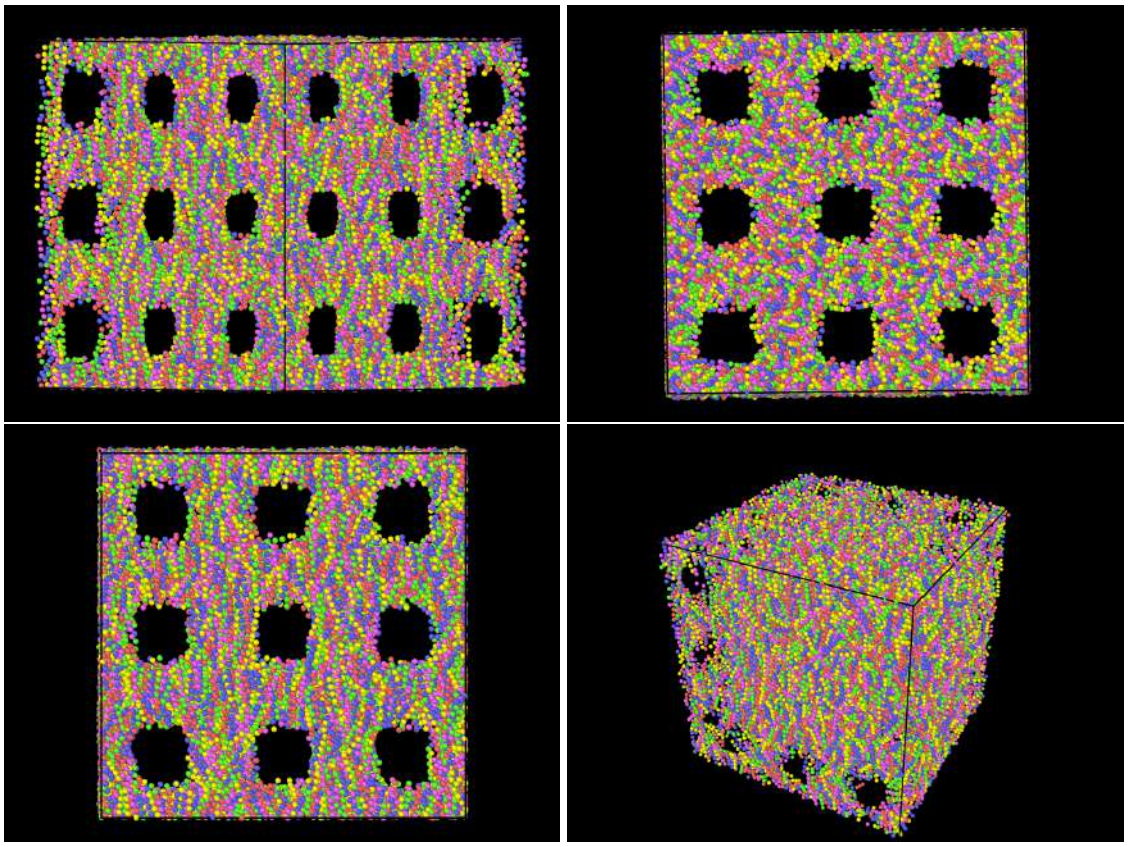


Figure 2.12: Shows the images of the system $\rho_0 = 0.247 g/cc$ having order parameter $S_2 \sim 0.4$ for all possible angle of view

systems with rod-like particles having $S_2 \sim 0.8$. Systems with $S_2 \sim 0.4$ and 0.0 were produced by increasing the thickness of bridges as keeping the same thickness would change(decrease) the nominal density of the system. This resulted in decrease of intrinsic number density(ϕ_I), hence the values are in the range $0.31 - 0.33$. For the first system in table the values are significantly less compared to rest of the cases as these quantities are back calculated. We can achieve similar values of intrinsic number density(ϕ_I) by working with spherical voids.

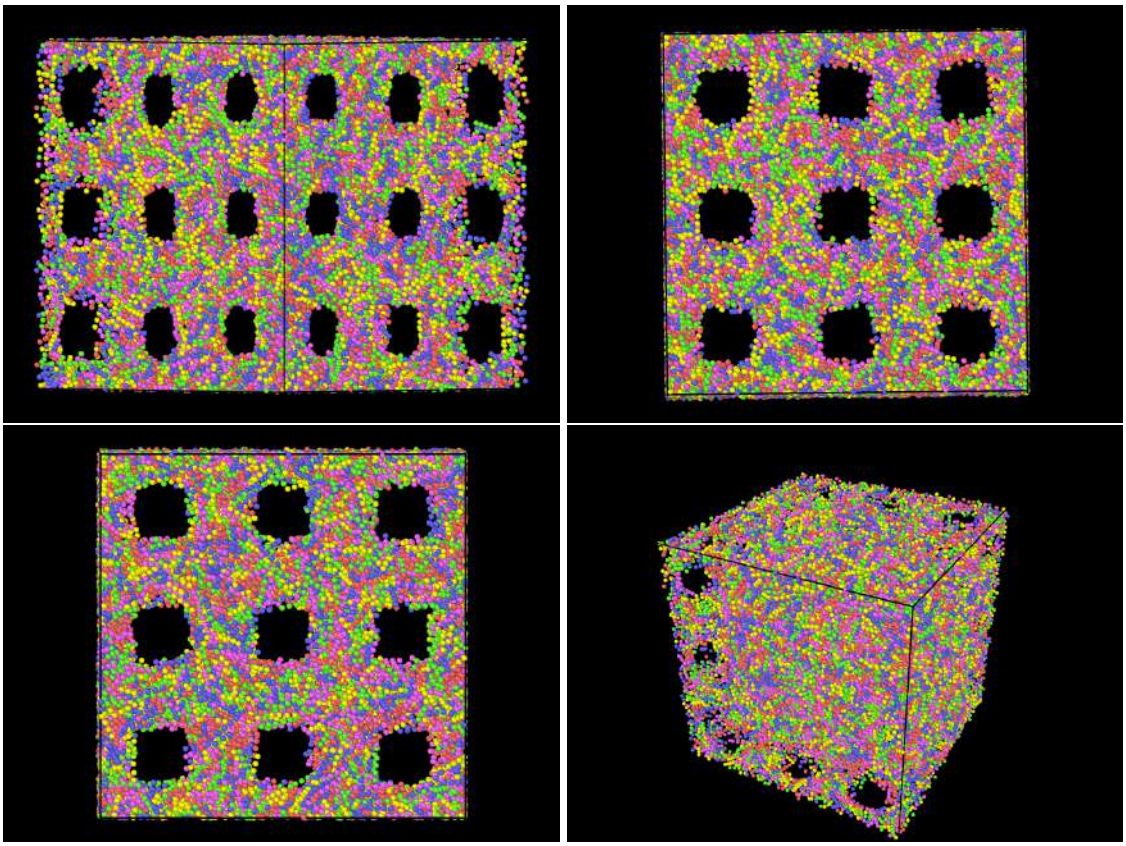


Figure 2.13: Shows the images of the system $\rho_0 = 0.247 g/cc$ having order parameter $S_2 \sim 0.0$ for all possible angle of view

Chapter 3

Results and Discussions

3.1 Validation of Previous Results

We plot the σ_{xx} component of the stress tensor as a function of the strain γ for six different densities in the range $0.5 - 0.34$g/cc[1]. Three distinct regimes can be demarcated based on the activity of various components of the system. Now we illuminate the microscopic origin and physics of three regimes. In regime-1 the stress increases linearly with strain up to $\gamma < 0.2$ (approximately), and the length of the springs get compressed and we do not observe any major deformation of the voids. Region-2 approximately corresponds to stress values of $0.2 - 0.5$, where the stress values increase slowly hence forming a plateau of stress values. The beginning of this regime marks the strain value at which the system buckles under compression. In this regime, voids start to deform and NPs surrounding these voids starts to fill them hence the length of the box in transverse direction L_Y and L_Z remains constant (Figure 2.4). During deformation, some of the springs get stretched, whereas others get compressed though the overall system gets compressed. In regime-3 for $\gamma > 0.5$, the stress and potential energy of the system start increasing rapidly with strain as the voids are filled with significant contribution coming from the WCA interaction between NPs.

3.1.1 Stress-strain response

Regime-1: In figure 3.1 we observe a linear increase in σ_{xx} with strain up to $\gamma = 0.2$. The extent of this regime depends on the nominal density $\rho_0 = mn_{NP}/(L\sigma^3)$ calculated before compression. In the inset of Figure3.1 we clearly identify the linear regime and transition point γ_T: the strain at which the stress values plateaus off. The transition point γ_T increases monotonically with ρ_0. From the initial slope of the stress-strain curve, we calculate linear modulus Y and plot it as a function of nominal density ρ_0. It is a known fact that Y increases linearly with ρ_0 when the elastic response of the sponge is through

[1]Note: The detail is taken from [8] as we have replicated most of the major results in the paper.

effective compaction of the cell walls. On the contrary, the system might also respond through bending of the cell walls if the spherical NPs are replaced by rods or ellipsoidal particles which we plan to investigate in the next chapter, in that scenario $Y \sim \rho^2$. Thus the functional dependence of modulus on nominal density can tell us about the microscopic response of the scaffold.

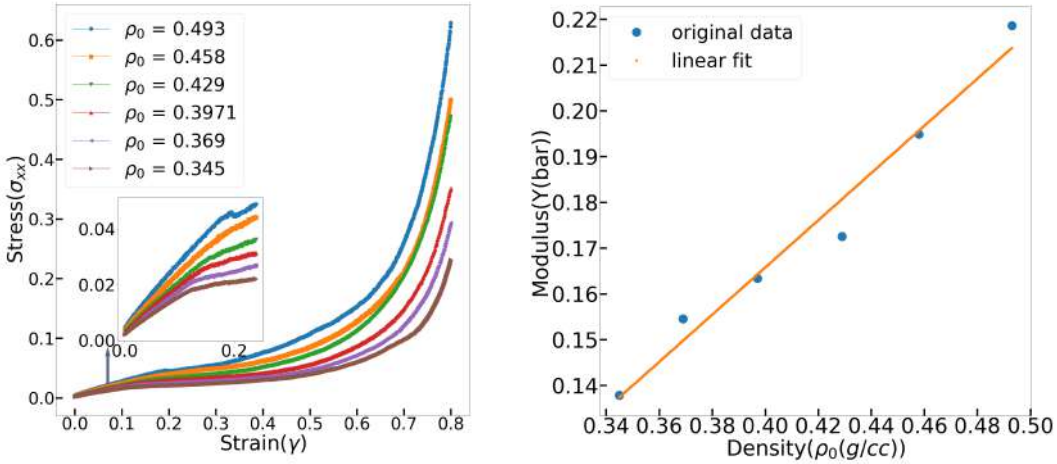


Figure 3.1: Left: Response of the system to applied strain by plotting σ_{xx} vs γ for several different values of the nominal density ρ_0, in units of g/cc. A decrease in the nominal density corresponds to an increase in the void fraction ϕ_V (at $\gamma = 0$). Right: The linear modulus Y is calculated from the slope of the stress-strain plots at low strains ($\gamma \to 0$). Y increases monotonically with the nominal density ρ_0.

The range over which we vary ρ_0, viz. $0.36 - 0.5$ is insufficient to conclude the linear dependence of Y. Contrary to our normal expectation computer simulation of less dense systems has a higher computational costs. As we have to increase box size L along with the size of the voids R_V to keep the bridge thickness Δ unchanged, rendering a larger number of NPs at junctions. In the next chapter, we work with cubical voids to design less dense systems, this will keep the bridge thickness unchanged and do not allow a larger number of NPs to be aggregated at the junctions.

Regime-2 Beyond the transition point we have the plateau regime, here σ_{xx} increases relatively slowly with γ. The rate of increase of σ_{xx} with γ is lower for a less dense system. This is expected as less dense systems has higher void volume fractions, hence more number of NPs surrounding the voids and it can be energetically easy to deform the voids. In the plateau regime, NPs start entering and occupying the voids while the positions of the NPs with respect to each other get reorganized. Also, the values of L_Y and L_Z remain nearly constant in this regime and start increasing at the onset of regime-3 Figure 2.4. We also provide movies of simulation which show the dynamics of void deformation.

Regime-3: Further compressing the system once the voids are filled by NPs leads to a rapid increase in the value of σ_{xx}. This marks the onset of regime-3. The system with lower ρ_0 enters regime-3 at much higher strains due to the large size of voids. This also implies less dense system can be compressed more before entering regime-3. It is not possible to clearly distinguish the transition from regime-2 to regime-3. The existence of two different regimes is reconfirmed by plotting the pair-correlation function g(r) in the next section.

3.1.2 Microscopic response to applied strain

The pair correlation function g(r) describes how the density of the system varies from the reference particle as a function of the distance. The $g(r)$ is usually determined by calculating the distance between all particle pairs and binning them into a histogram. This histogram is normalized by the number density of the system (ρ) multiplied by the volume of the spherical shell $\rho 4\pi r^2 dr$. In figure 3.2 we plot the pair-correlation function $g(r)$ versus the distance r between NPs, as we compress along the $\vec{x}$ direction for the system with $\rho_o = 0.49 g/cc$. The position of the first peak in the pair correlation function shows the highest probability of finding the nearest neighbours of a NP at the corresponding value of r, and the second prominent peak represents the most probable position to find the next set of nearest neighbours from the center of any NP. While the first peak for different values of γ is explicit, the second peak becomes broader for increasing values of γ. Furthermore the position of the first peaks shifts towards smaller values of r with increasing γ, this corresponds to decreasing distance between nearest-neighbour particles.

As shown in the inset of figure 3.2 the height of the peak decreases till $\gamma < 0.5$, after which the height starts to increase slowly. This marks the beginning of regime-3. Broadening of the second peak corresponds to wider distribution of distances between particles and their nearest neighbours as they occupy the void. As the peaks move further to the left for $\gamma > 0.5$, the height of the peaks also starts to increase slowly as the system gets tightly packed. As the strain increases from 0 to 0.8 with a volume change of approximately 80%, the peak position of $g(r)$ shifts from 1.1σ to σ with only a change of 10%. The flattening of the second and third peaks corresponds to a loss in long-range order as the NPs change their relative positions and rearrange their positions as the voids are filled under strain.

In Figure3.2 we plot r_{mean} as a function of γ for different values of ρ_0, where r_{mean} is the mean distance of the nearest neighbours from the center of a NP. The quantity r_{mean} is calculated by first selecting all the k nearest neighbours which are located at distances $r_k < r[g(r)_{min}]$. The quantity $r[g(r)_{min}]$ is the position of the first minimum of g(r). r_{mean} is calculated by first summing all the values of r_k weighted by the probability of finding

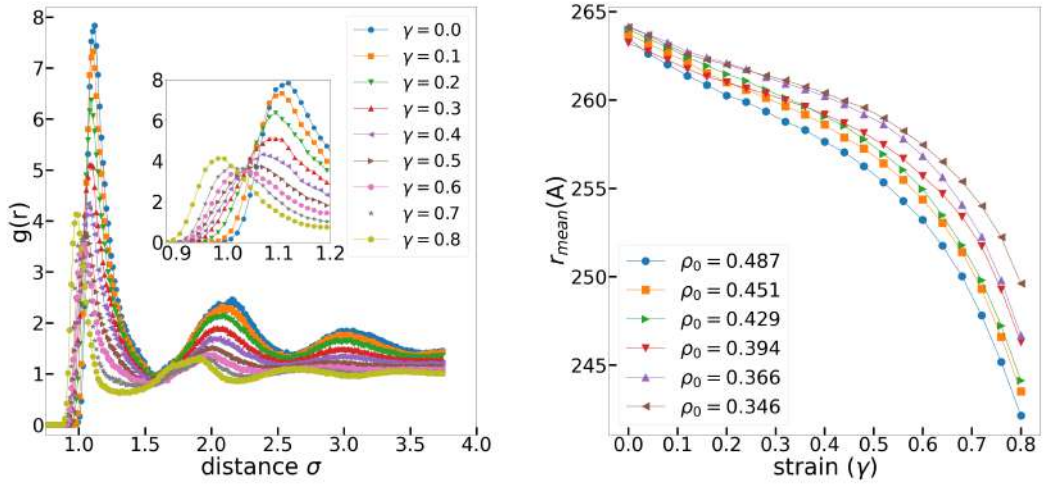


Figure 3.2: Left: The pair correlation function $g(r)$ vs distance r from a NP at different values of strains as given in legend, for a system of void fraction $\phi_v = 0.55$ (i.e.$\rho_0 = 0.49 g/cc$) with $R_{CL} = 1.5\sigma$. The inset shows the zoomed-in $g(r)$ so that the change in the position of the peaks of $g(r)$ can be easily identified. Right: An estimate of the mean distance of the nearest neighbors of a NP r_{mean} (refer to text for calculation details) as a function of the strain γ is shown for different ρ_0 .

the particle at r_k and normalized by the area under the curve of the first peak.

$$r_{mean} = \frac{\sum_{r_k}^{r_{min}} r_k \, g(r_k)}{\sum_{r_k}^{r_{min}} g(r_k)} \tag{3.1}$$

The area under the peak gives the total number of nearest neighbours surrounding a certain NP. Thus the quantity gives the mean distance of the nearest neighbor particles around a NP.

As we see in figure 3.1, the r_{mean} value keeps decreasing with increasing strain; this is further validated by increasing values of harmonic energy term in Figure2.5. We thus expect that the springs are getting compressed. However, as the system transitions from regime-1 to regime-2, we observed that the rate of decrease of r_{mean} with γ showed surprisingly a small upturn, which is prominent for systems with lower nominal densities. One can also observe the values of r_{mean} decrease with increasing ρ_0 for a particular value of γ though the intrinsic number density ρ_I is maintained identical in the junctions and bridges across all the values of densities.

We plot the probability distribution $p(\delta r)$ of the fluctuations of the spring length δr about its mean positions in Figure3.3. We have access to the equilibrium length of all the springs that are connected right after melting the lattice. Furthermore, we can measure the length of the springs at any arbitrary γ taking periodic boundary conditions into account. We calculate the δr of each spring by subtracting equilibrium length of springs

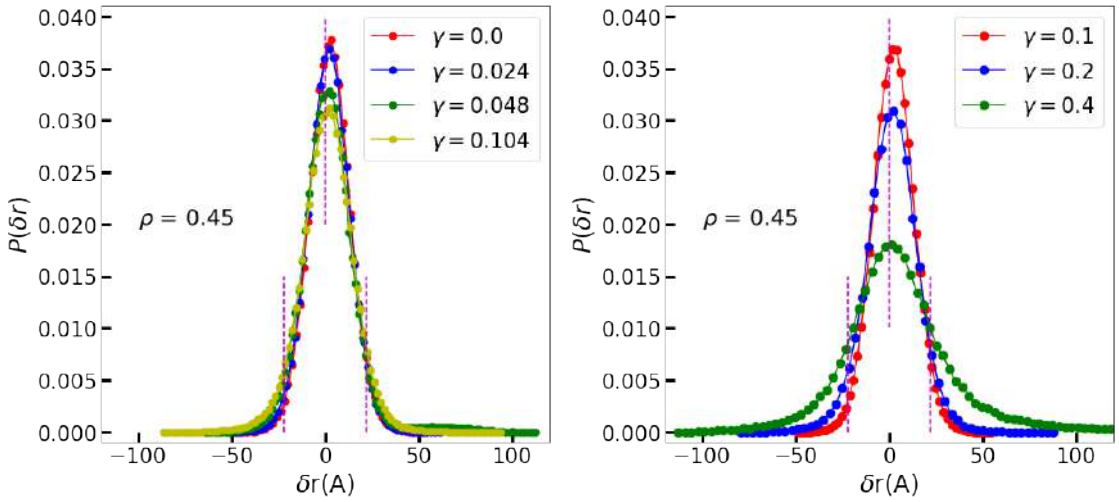


Figure 3.3: Left: Probability distribution $P(\delta r)$ of the deviation of bonds from its mean length vs the deviation δ is shown. The three vertical dashed line at $\delta r = -22\dot{A}, 0$ and $22\dot{A}$ are drawn to help the eye discern the asymmetry in the distribution. On an average the bonds are more extended than compressed. Right: probability densities of length fluctuations of interface springs for $\phi_V = 0.55$

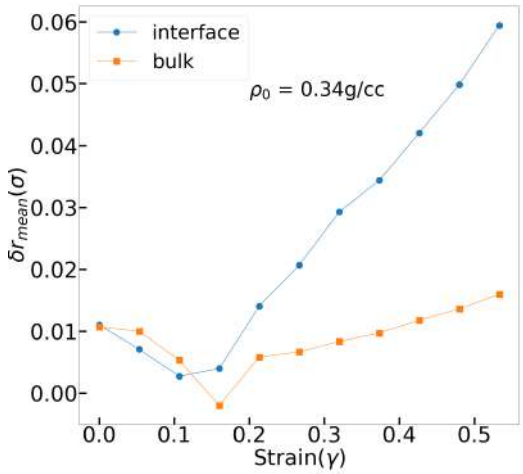


Figure 3.4: The mean deviation of the springs from their equi- librium positions δr_{mean} is calculated from the probability density distribution of the deviation of springs from their mean position δr is plotted as a function of strain for $\rho_0 = 0.34 g/cc$. Note : For the calculation of δr_{mean} of interface and bulk NPs, we have only considered springs which explicitly connect interface and bulk particles.

from the length of springs at desired γ.

We observe that the distribution is asymmetric about $\delta r = 0$ and that larger fraction of springs are stretched rather than compressed even at $\gamma = 0$(Figure3.3). We can quantify this by calculating the mean value of fluctuations of each of the springs, δr_{mean} and plotting it as a function of γ in Figure 3.4. We identify the NPs whose centers are located within the spherical shell R_V and $R_V + \sigma$ as interface NPs. We have plotted δr_{mean}

for $\rho_0 = 0.34$ up to $\gamma = 0.6$. Interested readers can also refer to Figure 5a. of [8] where δr_{mean} is also calculated separately for both interface and bulk NP for two different densities. In regime-2 springs at the interface are more stretched than springs at the bulk. Difference between the response of springs at the interface and those at bulk increases for systems with larger ϕ_V (Figure 5a. of [8]).
Moreover, δr_{mean} initially decreases with an increase in γ, reaches a minimum at the end of regime-1, and then increases with further increase in γ. This indicates that the springs get more stretched on average in regime-2, on compressing the system. Such observations suggest the material is softer at the interface and can deform more easily on compression as compared to the material in the bulk. Interface particles have larger length fluctuations as they can easily stretch out into the voids rather than moving into the bulk of the material. This creates an asymmetry in the probability distribution of the δr, resulting in positive values of δr_{mean} for most of the values of γ
The fact that there are more number of NPs at interfaces for systems with higher ϕ_V is reflected in the values of $r_{mean}(\gamma = 0)$ in figure 3.2. The behaviors of the δr_{mean} at small γ before the minima and the change in probability distribution as strain changes from $\gamma = 0$ to $\gamma = 0.1$ confirm the effective compaction of the springs in regime-1. The minima in Figure3.4 appears at lower strains for a system with lower ρ_0 as the interface can be more easily deformed. Moreover in figure 3.4 we also observe $\delta r_{mean}(I) > \delta r_{mean}(B)$ for $\gamma > 0.2$ in regime-2 confirming the softness of the interface. This increase in δr_{mean} in regime-2 explains the small upturn in the rate of fall of r_{mean} beyond $\gamma > 0.2$, which is more discernable for the system with a large void size.
We would also like stress that our plot for δr_{mean} is different from the one in [8] as we consider springs which connects interface NPs explicitly for $\delta r_{mean}(Interface)$ and springs which connects bulk NPs explicitly for $\delta r_{mean}(Bulk)$ calculation. Before ending we would like to emphasize that this macroporous system is intrinsically very different than the solid system with NPs connected by springs without open voids. We would like to emphasize the point that in our system with large open voids, the interfacial particles play a major role in the stress distribution, which leads to these three distinct regimes.

3.2 Results for Spherical Particles with Cubical Voids

Making cubical voids renders a constant bridge thickness between junctions and NPs are distributed uniformly across bridges and junctions. At the same time, cubical voids enable us to work with higher void volume fractions ϕ_V analogous to the lab-prepared scaffolds where the system might have $\phi_V \sim 0.9$. We were able to achieve similar values of ϕ_V by cubical voids, however it resulted in forming long beams, especially for systems with higher void volume fractions. We do not see such beams for scaffolds prepared in the lab even they have high ϕ_V because of (a)varying void sizes R_V and irregu-

lar void shape. (b)The positions of the voids are randomly arranged in the macroporous scaffolds.

Specifying the cylindrical regions and retaining those NPs whose centers are located inside the region, we obtain 27 large cubical-looking voids arranged in a cubical lattice with $L\sigma/3$ distance between adjacent void centers. We show results when such a system is compressed. We are primarily interested in the functional dependence of modulus (Y) on the nominal density ρ_0 and the range of densities investigated by Anish et al. was not sufficient to conclude linear dependence $Y \sim \rho_0$.

3.2.1 Stress-strain response.

Before we present the details of the stress-strain curve we first want to compare the stress-strain response of the system having spherical and cubical voids with approximately the same ρ_0(same number of NPs), ϕ_V and simulation box length $L\sigma$. In figure 3.5 we compare their response where system with the spherical voids has $\phi_V \sim 0.69$, $\rho_0 \sim 0.345$ and the system with cubical voids has $\phi_V \sim 0.68$, $\rho_0 \sim 0.342$. We chose $r_s = 4.3\sigma$ for the cubical voids system such that nominal density remains identical with spherical void system. We observe that the mean number of springs per NP for spherical voids is smaller than that of cubical voids. For example, for $\rho_0 = 0.34g/cc$ system, with cubical voids we have $N_B = 10.62$ relative to $N_B = 10.077$ for spherical voids. We conclude that spherical voids have large interfacial area compared to cubical voids. Since voids with a large interfacial area are easy to deform we expect the system with spherical voids to reach the transition point γ_T earlier than the system with cubical voids. Contrary to our expectation cubical voids reach the transition point earlier than spherical voids because bulky junctions dominate the stress response and prolong the value of γ_T. We also observe the cubical void system to have a flatter plateau regime than the spherical void system. Although the available volume for NPs in the spherical case: $(1-0.69)L^3$ is less compared to $(1-0.68)L^3$ in cubical voids system for ρ_0) cubical voids system has a higher slope in regime-1 compared to spherical voids system. This is because N_B(cubical voids) is higher compared to N_B(spherical voids).

Now we describe the how the wall thickness: radius of the cylindrical region r_s was chosen. We plotted the stress response of the systems with various $r_s = 2.2\sigma, 3.5\sigma$ and 4.5σ ie, we designed a set of systems with varying nominal density all having the same r_s. Here we show stress response for two values of $r_s = 3.5\sigma$ and $r_s = 4.5\sigma$ and describe which among them is optimum for further calculation.

Figure3.6 and 3.7 show the plot of instantaneous stress value of the system for $r_s = 3.5\sigma$ and $r_s = 4.5\sigma$ respectively as strain is applied. We have only shown the interesting linear regime and the transition point where the stress values plateaus off. We are only inter-

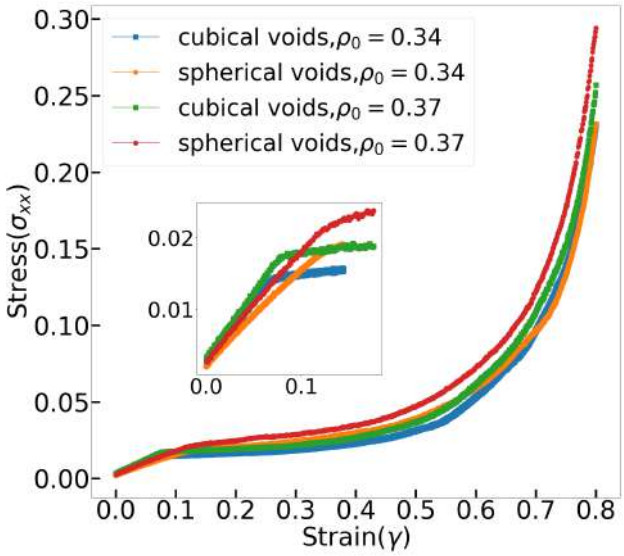


Figure 3.5: We compare the value of σ_{xx} obtained for both spherical voids and cubical voids scaffolds with nearly ρ_0 and ρ_V as mentioned in the text. Cubical voids scaffold have $r_s \sim 4.2\sigma$. Cubical voids have a stronger initial response but the value γ_T is relatively less.

ested in the slope and length of the linear regime. We observe a wider range of fluctuations of σ_{xx} for systems with $r_s = 3.5\sigma$. We observe for systems with $\rho_0 = 0.088, 0.07$ and $0.056 g/cc$ a negative slope instead of a small linear regime. We remark that for these systems we start observing stress at a little higher strain values. This indicates change in the box-size during NPT equilibration before applying strain whereas in the figure for system with $r_s = 4.5\sigma$, all stress values starts from zero strain indicating nearly stable box size during NPT equilibration. System with $r_s = 4.5\sigma$ have more stable stress values and all of the linear regimes are non-negative.

We observe much interesting oscillations in the plateau regime. We observe these oscillations for $\rho_0 = 0.253 g/cc$ for $r_s = 4.5\sigma$ and $\rho_0 = 0.17 g/cc$ for $r_s = 3.5\sigma$ albeit we are not of the threshold density at which oscillations become prominent. This periodic behaviour of stress values is a consequence of our modelling of macroporous scaffolds with cubical voids placed in a lattice. Moreover we have coarse-grained polymer degrees of freedom with entropic springs. These springs can store and transfer the energy to interconnected NP

As the strain γ is increased, initially the interconnected springs gets compressed(linear regime) and at a particular value γ_T when the system buckles, value of σ_{xx} starts oscillating. The frequency of oscillations depends on the length of the bridge i.e. a longer bridge will have lower frequency oscillation. The amplitude and frequency of oscillation gradually decays off before the system enters regime-3 (see Figure3.8). At a critical density $\rho_0 \sim 0.08$ the system do not show periodic behaviour (last two cases with $\rho_0 =$

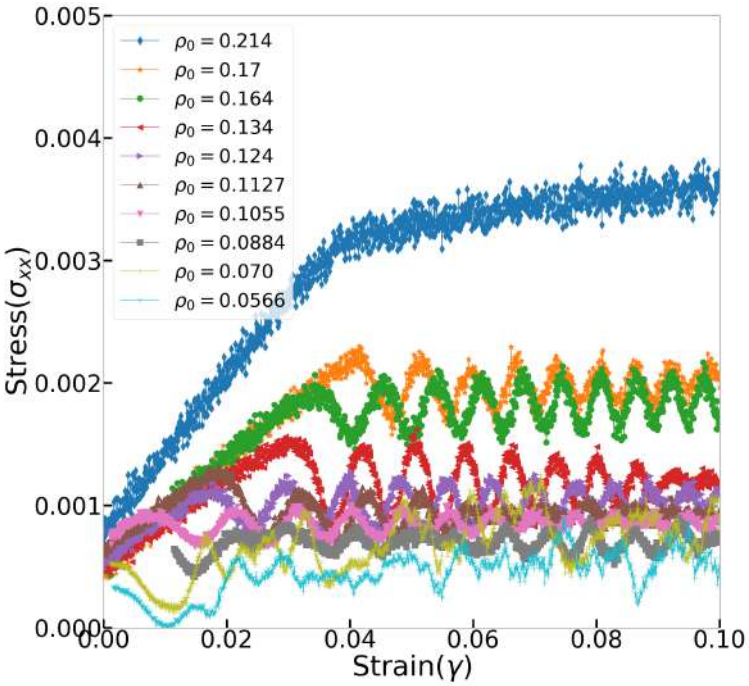


Figure 3.6: The instantaneous stress-response σ_{xx} is plotted as a function of strain for systems containing spherical particles. The cubical voids are created by cylindrical regions of radius $r_S = 3.5\sigma$.(Nominal densities ρ_0 are in g/cc)

0.086 and $\rho_0 = 0.069 g/cc$ in the Figure3.7).

The value of σ_{xx} at $\gamma = 0$ increases with nominal density. This trend is well defined in the Figure3.7, but in Figure3.6 with $r_s = 3.5\sigma$ this trend is not precise, for example value of $\sigma_{xx}(\gamma = 0)$ for $\rho_0 = 0.1055 g/cc$ is greater than $\sigma_{xx}(\gamma = 0)$ for $\rho_0 = 0.124$. Hence we conclude $r_s = 4.5\sigma$ to be ideal for Y *vs* ρ_0 calculation.

We explicitly show oscillations are consequences of cubical voids arranged in the lattice by plotting the stress response of scaffolds with modified cubical voids. To reach lower densities with spherical voids, would be computationally expensive as we will need a much larger box-size than was used for the cubical voids system. For finding the origins of oscillations in σ_{xx} we achieve a less dense system at the cost of changing the wall thickness. We define cylindrical regions as described in the previous sections and additional spherical regions at junctions to keep a sufficient number of NPs, of varying sizes as tabulated in the Table3.1 for a particular system. We choose the last case in the table 2.1 with $L = 55.9\sigma$ for this and systems having a density range of $0.346 - 0.085$ were produced.

Now we plot the $\sigma_{xx}(\gamma)$ when these systems are compressed (Figure3.9). Even though $r_s \sim 2.2$ is used for getting the lowest density we do not see wild fluctuations as there

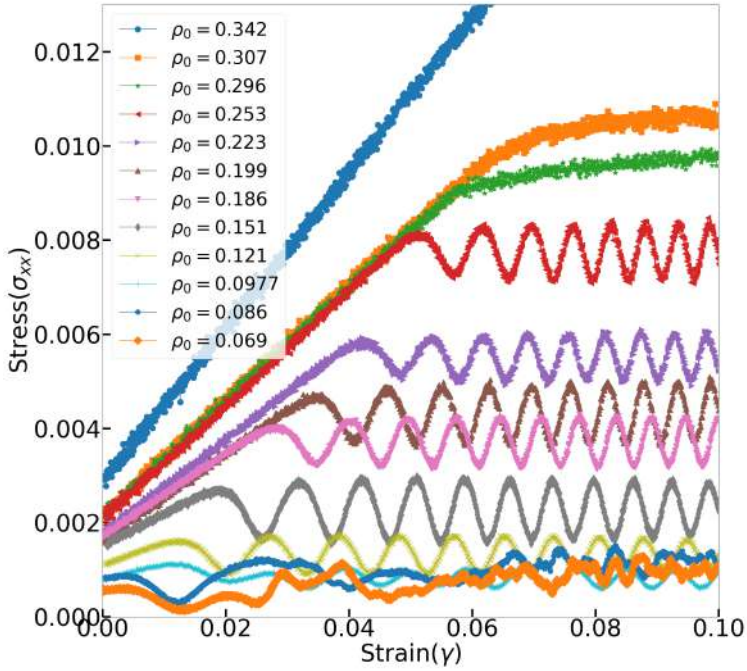


Figure 3.7: The instantaneous stress-response σ_{xx} is plotted as a function of strain for systems containing spherical particles. The cubical voids are created by cylindrical regions of radius $r_S = 4.5\sigma$. We observe less fluctuations in the σ_{xx} values compared to the above figure3.6 where $r_S = 3.5\sigma$ as the bridges are more thicker for systems with $r_S = 4.5\sigma$. (Nominal densities ρ_0 are in g/cc)

are no perfect beams and interestingly there are no oscillations in the plateau regime. We have also plotted Y *vs* ρ_0 for these scaffolds in figure 3.10 along with six cases discussed in the table 2.1. Linear modulus Y varies linearly with ρ_0 to our satisfaction, even though wall thickness is not constant across different densities.

We have also plotted the pair-correlation function (RDF) for four densities $\rho_0 = 0.307, 0.253, 0.186$ and $0.0977 g/cc$ in Figure3.11. We have normalized $g(r)$ values by nominal density ρ_0 and since our system has large voids the height of the first peak varies and $g(r)$ do not tends to 1.0. Effectively, height of the peak indicate size of the voids. Instead if we normalize by intrinsic density ρ_I, $g(r)$ tends to 1 as well as the height of the first peak remains same for different densities (Figure3.12). We are not able to normalize with intrinsic density for $\gamma \neq 0$ because voids deform stochastically under compression. In contrast to the RDF plot in the section 3.1 for $\rho_0 = 0.5 g/cc$ we observe decreasing height of the first peak. Infact the rate of fall of the first peak height decreases as the strain is applied and this effect is not prominent for less denser system like $\rho_0 = 0.0097$ where the rate of fall of the first peak is nearly constant. Also $\gamma \sim 0.8$ curve indicate loss of long range correlation of positions of NPs as these curves are more flatter. The amount

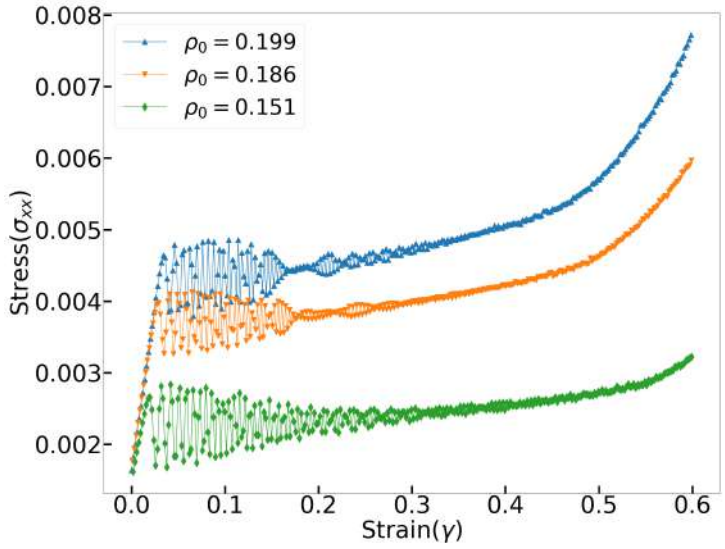


Figure 3.8: Plot of $\sigma_{xx}(\gamma)$ for $r_s = 4.5\sigma$, here we have plotted σ_{xx} upto $\gamma = 0.6$. We observe oscillations decay gradually before the system enters regime-3. (Note: The values of σ_{xx} are averaged out.)

Radius of spherical region(σ)	Radius of cylindrical region(σ)	$\rho_0(g/cc)$	n_{NP}	n_{bonds}	N_B
5	4	0.346	37161	189010	10.172
5	3.56	0.310	33366	166565	9.984
4	3.22	0.28	29824	146660	9.835
3.5	2.82	0.24	24693	117314	9.5
3.5	2.5	0.206	19924	11557	9.19
3.0	2.1	0.118	14190	61259	8.634
3.0	1.7	0.085	10202	41239	8.084

Table 3.1: The table lists the values (a) The radius of the spherical regions defined at 27 junctions. (b) The radius of the cylindrical regions (c) The nominal density after creating the voids. (d) The total number of nanoparticles (n_{Np}) (e) The total number of bonds interconnecting NPs in the system (f) Mean number of bonds per NP(N_B).

of distance shifted towards left by the first peak also decreases for less denser system.

3.2.2 Calculation of Young's modulus

Now we present the details of Y vs ρ_0 plots in the Figure3.13. We plot the slope obtained by stress response of cubical voids scaffolds along with spherical void scaffolds in the Table2.1 even though both have a somewhat non-identical response. We were able to cover a decade range in the densities and we remarkably have a linear relationship between Y and ρ_0. We also plot log(Y) vs log(ρ_0) to get the exact exponent and we have approximately a linear scaling $Y \sim \rho_0^{1.2}$. Note that x-axis in the Figure 3.14 has been normalized by lowest density $\rho_0 = 0.069$.

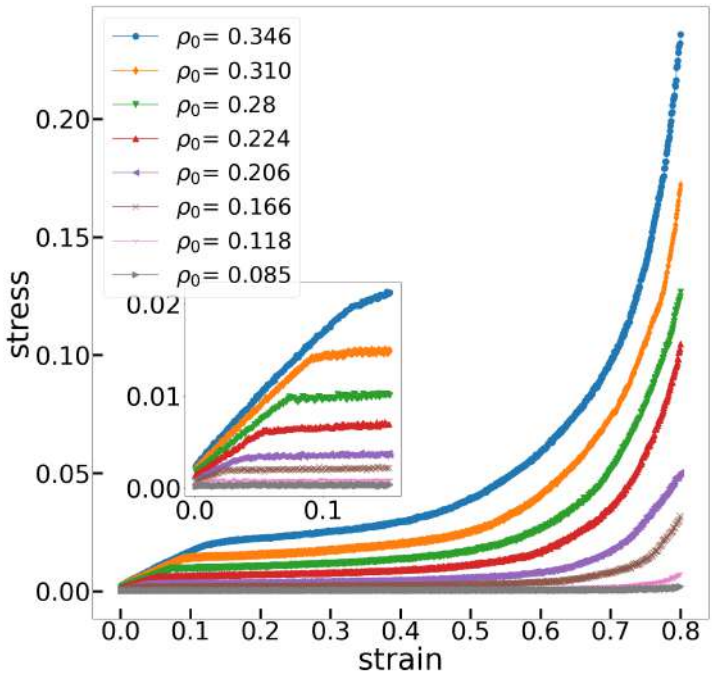


Figure 3.9: Plot of σ_{xx} for modified cubical voids systems. All the systems with densities $\rho_0 = 0.346 - 0.085 g/cc$ are produced from the system with $L = 55.9\sigma$ case in table 2.1 by retaining NPs in various cylindrical and spherical regions as tabulated in table 3.1. Note: we do not have oscillations in the σ_{xx} values, hence we conclude cubical voids arranged in the cubical lattice that leads to shaping of long beams between the junctions is the source of oscillation. Additional spherical regions are defined at junctions (where the beams meet) so that more number of NPs remain at junctions and do not form long beams.

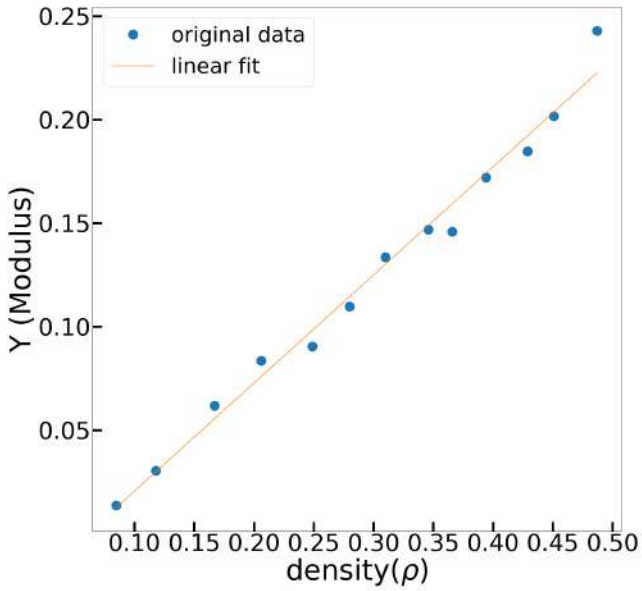


Figure 3.10: Linear modulus Y is plotted against nominal density ρ_0 for scaffolds with spherical voids. The Young's modulus is calculated from the slope of initial linear regime in the above figure3.9.

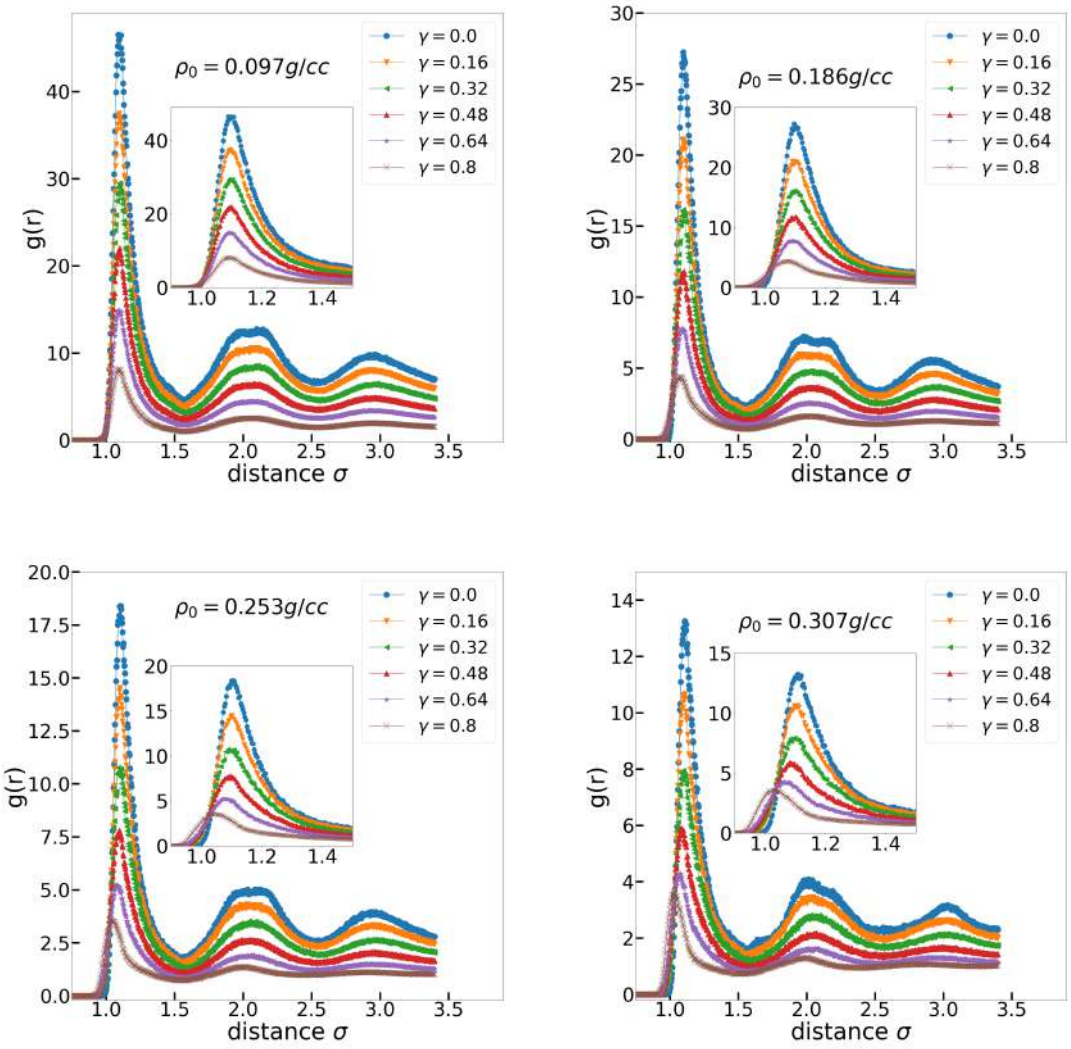


Figure 3.11: Pair-correlation plots for 4 cubical voids scaffolds of varying densities as given in the plot. Since the void-volume fraction here is large compared to spherical void scaffolds, height of the first peak always deceases as $\gamma(0 \rightarrow 0.8)$. Height of the first peak of $g(r)$ increases as we go to lower densities for the same value of γ. This is because we have normalized $g(r)$ values by nominal density ρ_0. Instead if we normalize by intrinsic density ρ_I then the height of the first peak will be same for different densities and $g(r) \rightarrow 1$ for sufficiently large r.

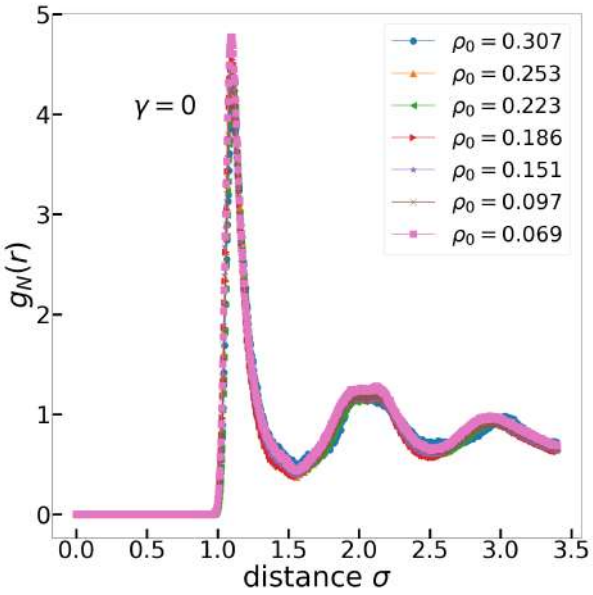


Figure 3.12: Pair-correlation plots normalized with intrinsic number density $n_{NP}/((1-\phi_V)L^3)$ for $\gamma = 0$.. Since the height of the first peak gives the probable number density of neighbouring NPs, same height of the peaks indicate we have identical intrinsic densities across varying ρ_0.

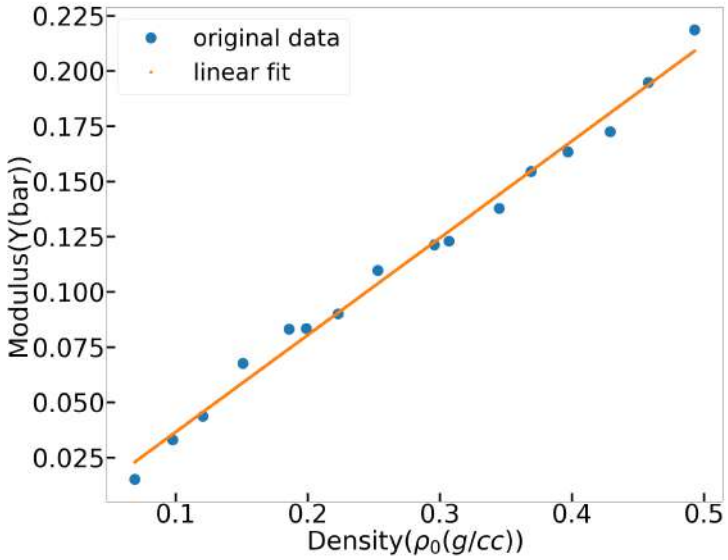


Figure 3.13: Plot of Linear modulus Y with nominal density ρ_0 for both spherical void scaffolds (in the density range of $0.50-0.34$) and cubical void scaffolds (rest of the range $0.30-0.069$).

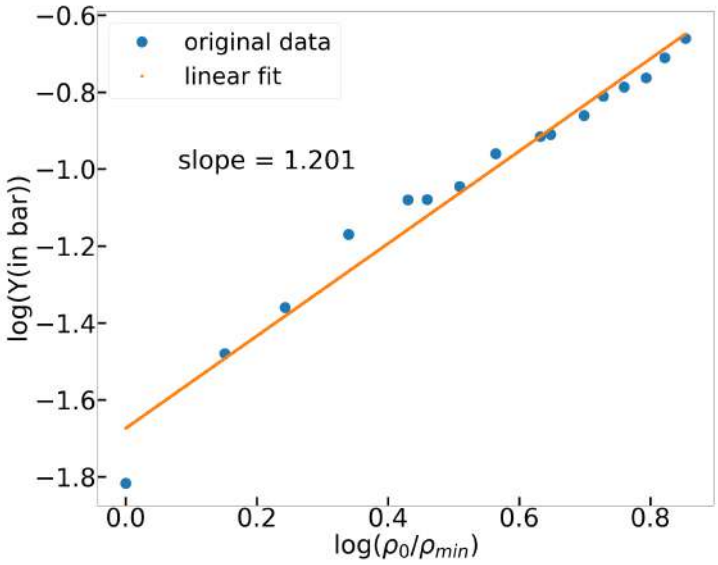


Figure 3.14: log-log plot of Y vs ρ_0 for the figure in 3.13. Note that x-axis has been normalized by lowest nominal density $\rho_{min} = 0.069$. With slope $m = 1.2$ we have nearly linear scaling $Y \sim \rho_0^{1.201}$.

3.3 Results for Rod-like Particles with Cubical Voids

Similar to retaining NPs in a defined cylindrical region for scaffolds containing spherical fillers, in scaffolds with rod-like fillers we retain rods in the defined cuboidal region so that bridge thickness is nearly the same across different densities. We designed $S_2 \sim 0.4$ and 0.0 systems with the same nominal density at the cost change in intrinsic volume fraction ϕ_I and bridge thickness Δ. For scaffolds with rod-like fillers ϕ_I was kept identical with cases in Table2.1 only for $S_2 \sim 0.8$ systems. We stress the fact that ensuring identical $Intrinsic\ volume\ fraction\ (\phi_I)$ between systems with spherical and rod-like fillers would be meaningless as the shape of the fillers are different. We have chosen rods of aspect ratio 4.75 built by joining four spherical beads of diameter 0.8σ. We initialize such rods and equilibrate them for varying number of MD steps to get systems with $S_2 \sim 0.8, 0.4$ and 0.0 as described in the section2.3.2.

We compressed a system in two directions, viz. parallel and perpendicular to the direction along which all the rods are oriented. We initialized the rods along the Z-direction. We call σ_{zz} and σ_{xx} for the stress values obtained upon compressing parallel and perpendicular to the direction along which the rods are oriented. In the section 2.3.2 we assumed the beads in a rod have mass M $= 0.512 \times (14.8 \times 10^{-21})$Kg as volume of a bead is 0.512 times the volume of NP in section 3.1. We designed 6 different densities in the range $0.247 - 0.079$ with $S_2 \sim 0.8, 0.4$ and 0.0. We are interested in the functional dependence of Y on ρ_0. Experimentally it is observed that $Y \sim \rho_0^2$ as the bridges respond by bending instead of getting compressed under strain. Y varies linearly with ρ_0 if the bridges respond by compression (changing the relative positions of NPs) as established in section3.1

Before we present the details of stress-strain let us make a quick calculation to convince ourselves that $Y \sim \rho_0$ and $Y \sim \rho^2$ indeed arise from the response of the cell walls by its compression and bending respectively. If the walls respond by compression then the work done by compressive force F is $F\delta = Y_W d^2 t\varepsilon^2$, where δ is the change in pore dimension along the compression axis, Y_W is the modulus of the wall, d is the pore diameter, t is the thickness of the wall and ε is the strainδ/d[22]. Simplifying, we have for the compressive force $F \sim t\delta$. Now experimentally observed modulus of the foam can be written as $Y = nominal\ stress/strain = (F/d^2)/(\delta/d)$. Now substituting the expression for F and multiplying by $d\delta^2$ we obtain:

$$\frac{Y}{Y_W} \sim \frac{t}{d} \tag{3.2}$$

If the density of the walls is ρ_W,then we can also write $\rho_W(d^2t) \sim \rho_0 d^3$, thus $\rho_0/\rho_W \sim t/d$ and combining with 3.2 we obtain:

$$\frac{Y}{Y_W} \sim \frac{\rho_0}{\rho_W} \tag{3.3}$$

When scaffolds respond by bending of the cell walls. beam theory for linear elastic deflection shows that the deflection, $\delta \sim Fd^3/Y_W I$, where I is the second moment of inertia of the area of the cell wall[22]. Therefore, Young's modulus is given as $Y = \sigma d/\delta$. Substituting for δ and $\sigma = F/d^2$ and $I \sim d^2$ we get:

$$\frac{Y}{Y_W} \sim \frac{Y_W I}{d^4} \sim (\frac{\rho_0}{\rho_W})^2 \tag{3.4}$$

3.3.1 Stress-strain response

We investigated the stress response of rod particle scaffolds for various values of r_c. If the distance between any two beads belonging to two different rods is within r_c, then the pair of beads is connected by a a spring. Here we chose to work with $r_c = 1.5\sigma$. The details of total total number of springs, mean number of springs per rods etc are tabulated in the table 2.3.2. First we present the stress response for $\rho_0 = 0.247 g/cc$ system with three different r_c i,e. $r_c = 1.25\sigma, 1.50\sigma$ and 1.75σ. We compress he system in the z direction along which the rods are oriented.
In Figure3.15 we observe a higher $r_c = 1.75\sigma$ will generate a stronger initial response, followed by $r_c = 1.50\sigma$ and $r_c = 1.25\sigma$ has weakest response among them. We have only shown the linear regime and the transition of σ_{zz} values to plateau regime (upto $\gamma = 0.25$). We note, for a particular value of r_c, system with $S_2 \sim 0.8$ i,e all the rods oriented in the z direction strongly, has the highest slope in the linear regime, followed by $S_2 \sim 0.4$ and $S_2 \sim 0.0$. It is intuitive that when the system of rods are compressed in the same direction in which they are aligned, response is similar to a solid until the walls of the system buckle. Similar trend can be observed for all the three cases $r_c = 1.75\sigma, 1.50\sigma$ and 1.25σ.

For the $S_2 \sim 0.8$ system, initially in the linear regime there is no significant change in the size of the voids, at a particular strain when the system buckles, the value of σ_{zz} makes a sharp transition to the plateau regime and the voids start to deform significantly. We remark that given a macro-porous scaffolds of different order parameters at a particular density, we can distinguish between them in the linear regime by compressing them along the direction of orientations. In the Figure3.15 we observe in the plateau regime for a given r_c, system of different order parameters achieve approximately similar value of σ_{zz}. We remark the strain value for $S_2 = 0.4$ and 0.0 systems at which they make tran-

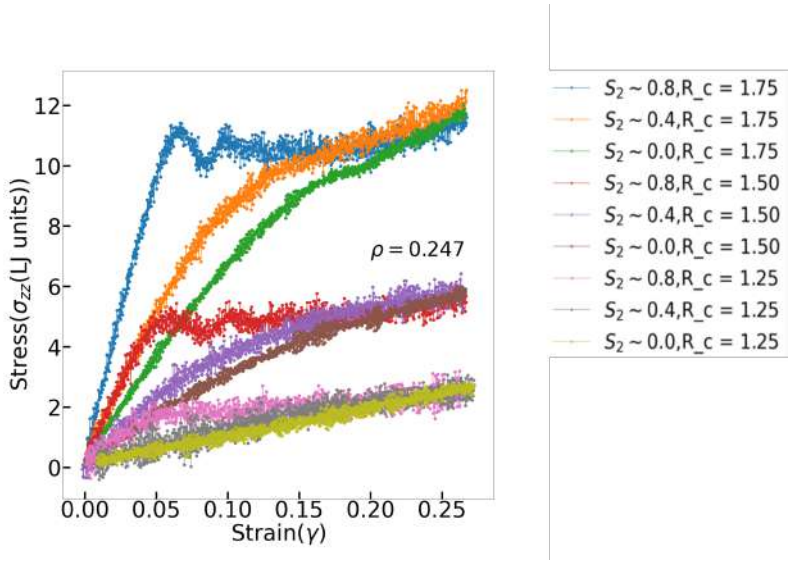


Figure 3.15: Shows the stress-strain response of $\rho_0 = 0.247 g/cc$ system having order parameter $S_2 \sim 0.8, 0.4$ and 0.0 with three different $r_c = 1.75\sigma, 1.50\sigma$ and 1.25σ when compressed in $\vec{z}$ direction. Also note, by $S_2 \sim 0.8$ we mean most of the rods are oriented strongly along the $\vec{z}$ direction (see figure2.11). Order parameter $S_2 \sim 0.4$ implies rods are oriented on average in the $\vec{z}$ direction but not strongly as $S_2 \sim 0.8$ (figure2.12). We follow this convention in the following discussions and for all the data we present. For system with $S_2 \sim 0$, rods are oriented randomly and the director of the phase should point approximately along $(1/\sqrt{3}, 1/\sqrt{3}, 1/\sqrt{3})$.

sition to plateau regime is indecisive. This implies, unlike $S_2 \sim 0.8$ system, there is no abrupt buckling. The walls of the system gradually arc as the σ_{zz} values progress towards plateau regime.

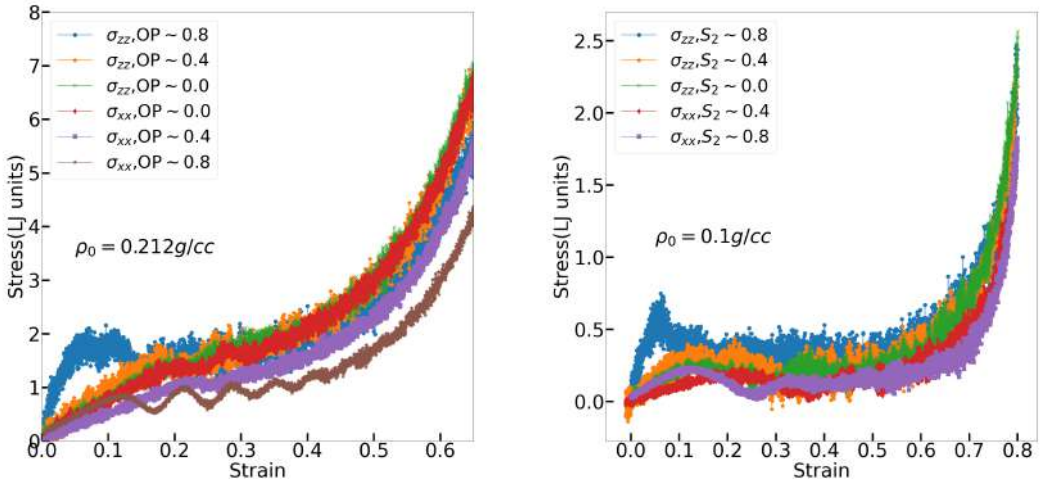


Figure 3.16: Stress-strain response of systems having nominal densities $\rho_0 = 0.212$ and $0.1 g/cc$ with cutoff $r_c = 1.25\sigma$ for three different order parameters.

Unclear of what r_c to choose for further calculation, we decided to compress in the $\vec{x}$ direction also for systems of different densities. In the Figure3.16 we have plotted instantaneous values of both σ_{zz} and σ_{xx} for $\rho_0 = 0.212g/cc$ and $0.1g/cc$ with three different order parameters $S_2 \sim 0.8, 0.4, 0.0$ having the cutoff $r_c = 1.25\sigma$. In the Figure 3.17(top left) we have also plotted the same quantities for $\rho_0 = 0.212$ with $r_c = 1.5\sigma$. Reader can notice the wide range of fluctuation for systems with $r_c = 1.25$ hence we decided to work with $r_c = 1.5\sigma$. We have also plotted the instantaneous values of stress for each of the $S_2 \sim 0.8, 0.4, 0.0$ values having six different densities with cutoff $r_c = 1.5\sigma$ in the same Figure. Reader is encouraged to look at this instantaneous data and compare with averaged one in Figure3.19. Using $r_c = 1.75\sigma$ would render too many bonds per rod, and the response would be dominated by springs.

For the purpose of clear visualization and further calculation we plot the averaged out the stress values in the Figure3.18. In Figure3.16 we had 5000 data points between $\gamma = 0.0$ and 0.8. we take average of every 25 stress values such that we have 200 data points in Figure3.18. When the system is compressed in $\vec{x}$ direction, we expect the slope of $S_2 = 0.8$ system to be lower than the slope of $S_2 \sim 0.4$, but we observe slope for $S_2 \sim 0.8$ system to be slightly greater for most of the system. This is because $S_2 \sim 0.8$ system is tightly packed hence has a higher intrinsic volume fraction ϕ_I compared to $S_2 \sim 0.4$and0.0 systems leading to more number of springs per rod (see Table2.3.2 and in the linear regime scaffolds respond by compression of the springs. Compression of large number of springs results in higher stress response of $\sigma_{xx}(S_2 \sim 0.8)$ compared to $\sigma_{xx}(S_2 \sim 0.4)$ in the linear regime. In the plateau regime system respond by deformation of the voids instead of contraction of springs hence the value of σ_{xx} in the plateau regime is lower for $S_2 \sim 0.8$ system compared to $S_2 \sim 0.8$ system. This confirms the conclusion made for spherical particles by calculating δr_{mean} for interface and bulk particles in the Figure3.4.

We note in Figure3.18the response of isotropic phase ($S_2 \sim 0.0$) system is not identical when compressed in $\vec{z}$ and $\vec{x}$ direction for most of the systems, indicating insufficient equilibration for melting the lattice completely. Reader might recall in section 2.1, isotropic phase was obtained by NVT equilibration at a very high temperature for very long iterations. Even though $S_2 \sim 0.0$ was confirmed by our code, there might be local ordering of the rods responsible for non-identical response when compressed in different direction for isotropic phase.

Once the voids are filled and system enters the regime-3, we observe a general trend in the value of σ in the Figure 3.18: $\sigma_{zz}(S_2 = 0)$, $\sigma_{xx}(S_2 = 0)$ and $\sigma_{zz}(s_2 = 0.4)$ have a higher value followed by $\sigma_{zz}(S_2 = 0.8)$, $\sigma_{xx}(S_2 = 0.4)$ and finally $\sigma_{xx}(S_2 \sim 0.8)$ has the lowest value. The value of $\sigma(\gamma = 0.8)$ will be lesser if most of the rods are oriented in the transverse plane perpendicular to the compression axis. Indeed for the system with

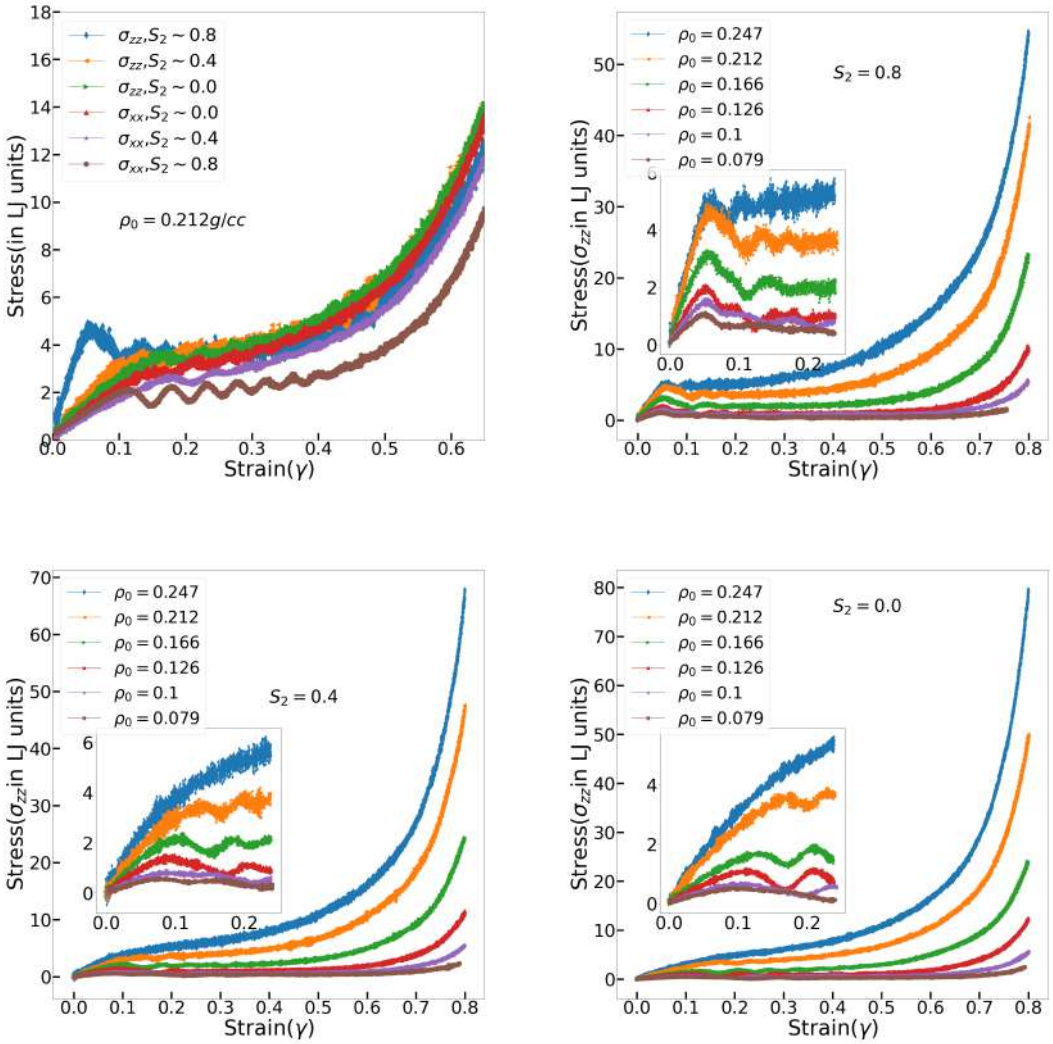


Figure 3.17: Top left: Shows stress response for $\rho_0 = 0.212 g/cc$ with $r_c = 1.50\sigma$. Reader can observe a lesser fluctuation compared to Figure3.16. Rest of the plots show the instantaneous stress-response for $S_2 \sim 0.8, 0.4$ and 0.0 with $r_c = 1.5\sigma$ having six different nominal densities (in units of g/cc) compressed in $\vec{z}$ direction as discussed in the Table2.3.2.

$S_2 \sim 0.4$, the value of $\sigma_{xx}(\gamma = 0.8)$ is lower compared to $\sigma_{zz}(\gamma = 0.8)$ as most of the rods remain aligned in the transverse plane albeit the value of local order parameter in both might be same. Similarly for $S_2 \sim 0.8$ system we observe $\sigma_{xx}(\gamma = 0.8) < \sigma_{zz}(\gamma = 0.8)$ even though both system preserve local order parameter under large compression.

The rods in the isotropic phase are randomly oriented in all direction for any $\gamma \neq 0$, hence achieve highest value of $\sigma(\gamma = 0.8)$. In the Figure3.19 we show the stress response at a particular value S_2 compressed in $\vec{z}$ or $\vec{x}$ direction, of six different densities. We observe a negligible change in the slope from linear regime to plateau regime for $\rho_0 = 0.247 g/cc$ system having $S_2 = 0$ and compressed in $\vec{z}$ ans $\vec{x}$ direction. Even with $S_2 \sim 0.4$ and 0.8 for $\rho_0 = 0.247 g/cc$ compressed in $\vec{x}$ direction, we do not observe a

significant change in the slope. This might be because of smaller void volume fraction for $\rho_0 = 0.247 g/cc$ ($\phi_V \sim 0.37$ for $S_2 \sim 0.4$ and 0.8 cases (Table2.3.2). The length of the bridges are not long enough to cause visible buckling. However we observe buckling for other system with lesser ρ_0 having $S_2 \sim 0.4$ compressed in $\vec{x}$ direction and hence a change in the slope from linear regime to plateau regime. But we confirm beyond doubt the existence of plateau regime, as the value of σ_{xx} for $S_2 \sim 0.8$ system in the plateau regime is lower compared to $S_2 \sim 0.4$ system for most of the nominal density ρ_0.

We again observe interesting oscillations in the Figure3.19 once the system makes a transition to plateau regime. This periodicity in the σ values become prominent for system with bigger simulation boxes upto $L = 96\sigma$. However for systems with $L = 108\sigma$ the periodic behavior is lost.

3.3.2 Calculation of Young's modulus

We finally present the plots for Young's modulus(Y) vs nominal density (ρ_0). We have designed different densities for three order parameters $S_2 = 0.8, 0.4$ and 0.0 and we have compressed each in two directions, viz. parallel and perpendicular to alignment direction, hence we will have six different Y vs ρ_0 plots. The Figure3.21 shows six different Y vs ρ_0 plots. To get the exact exponent of the functional dependence of Y we also show its logarithmic plots i,e. log(Y) vs log(ρ_0) in the Figure3.22. The slope we obtain for different cases is crucially dependent on how many points do we consider for Y vs ρ_0 calculation from the Figure3.19 where the stress values are averaged out. We rigorously consider only a few number of points in the linear regime for Y vs ρ_0 calculation, which makes a linear fit to the beginning part of the linear regime (see Figure3.20). This is very important because within the span of the linear regime the slope decreases slightly as the plateau regime is reached and we are only interested in the very beginning of the linear regime.

	σ_{zz}	σ_{xx}
$S_2 \sim 0.0$	1.559	1.534
$S_2 \sim 0.4$	1.485	1.615
$S_2 \sim 0.8$	1.332	1.265

Table 3.2: The table lists the values of slopes obtained in Y vs ρ_0 plots for all the cases

The fact we have prepared the $\rho_0 = 0.247 g/cc$ system with lesser intrinsic volume fraction ϕ_V is clearly visible for $S_2 \sim 0.8$ when compressed in σ_{xx} direction in the Figure3.21. We might also get a higher slope/modulus for $S_2 \sim 0.4$ and 0.0 systems had we maintained the identical ϕ_I. We will soon redesign the first two systems in Table2.3.2 such

that all the cases have the same intrinsic volume fraction ϕ_I and we will try to cover a decade range in densities. Bearing all these issues we obtain six different exponents for log-log plots as tabulated in the table.

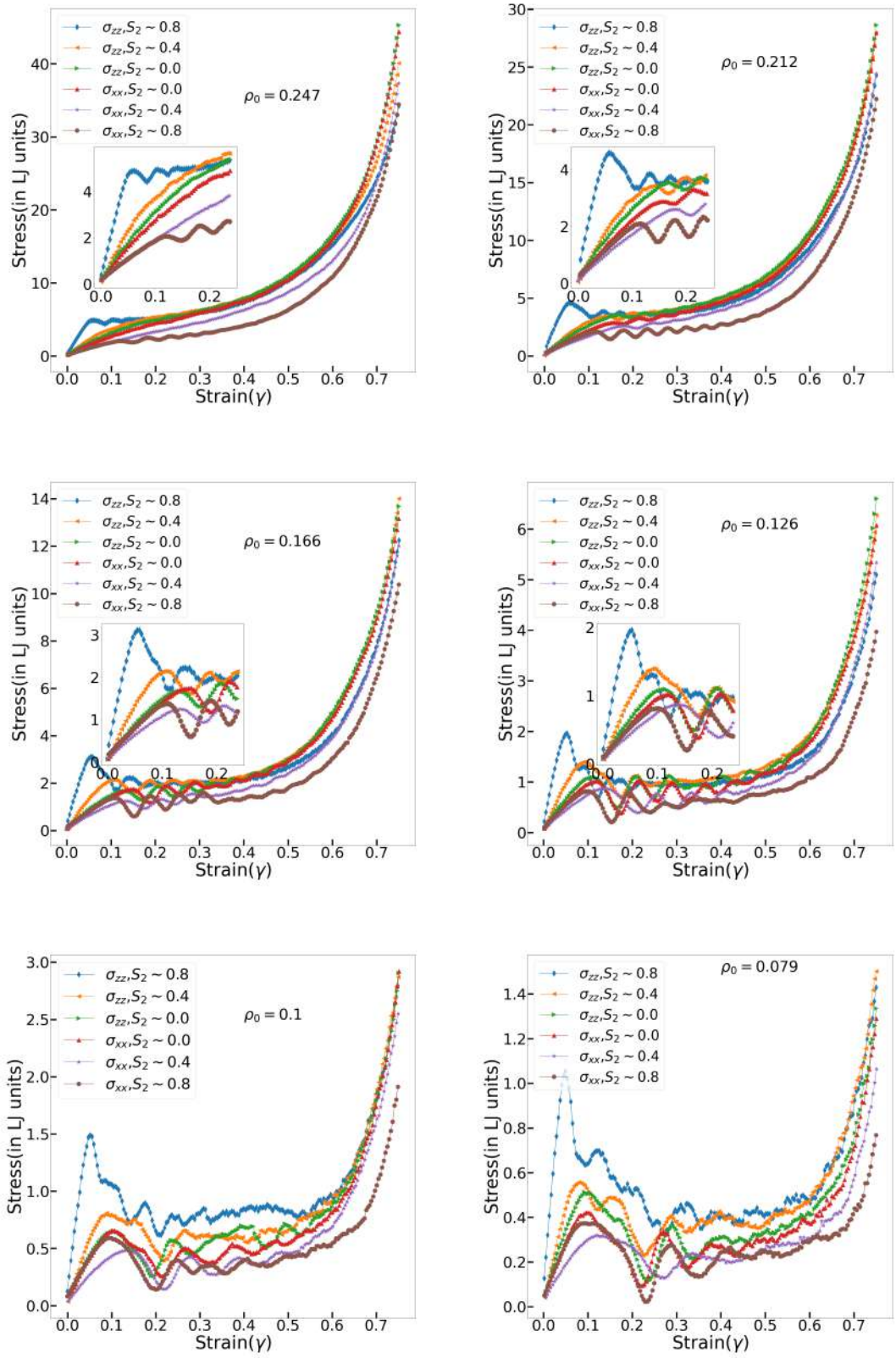


Figure 3.18: Plot of stress-strain response of various densities upon compression in both parallel(σ_{zz}) and perpendicular(σ_{xx}) direction to orientational direction($\vec{z}$) of rods. (Nominal densities ρ_0 are in g/cc)

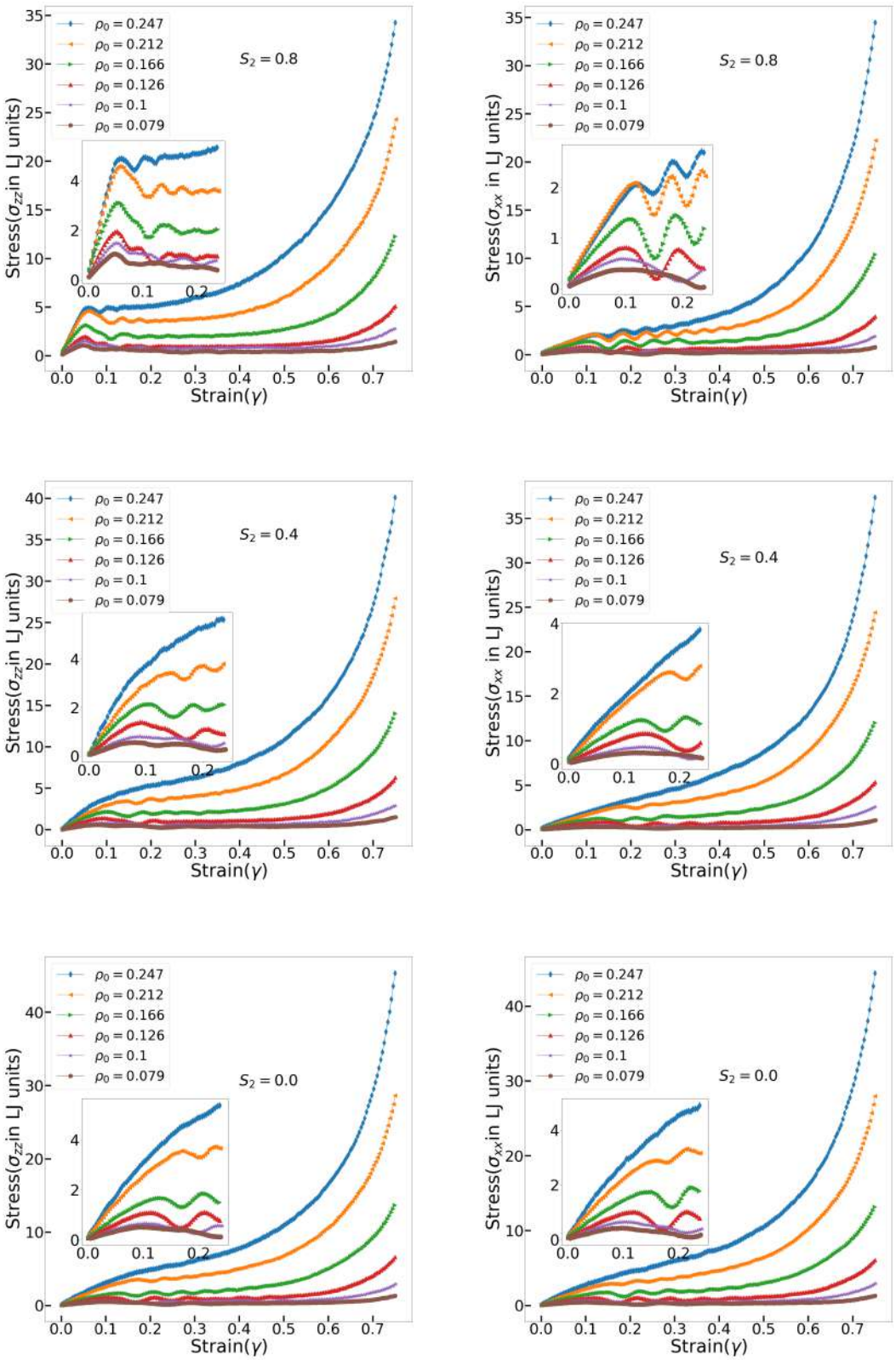


Figure 3.19: Plot of stress response at a particular value S_2 compressed in $\vec{z}$ or $\vec{x}$ direction, having six different nominal densities(units in g/cc).

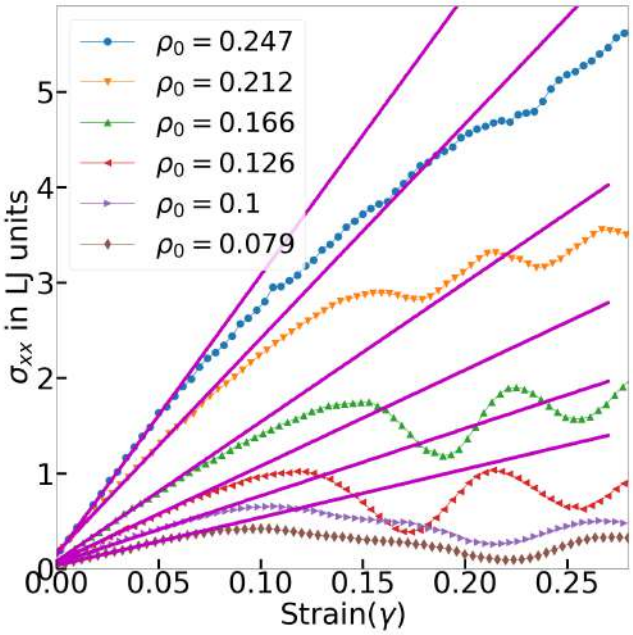


Figure 3.20: We show how the straight line fit was made to all the six plots in figure 3.19. In this plot, $S_2 \sim 0$ for all densities, we made a linear fit to initial regime using first 15 points for all the ρ_0.

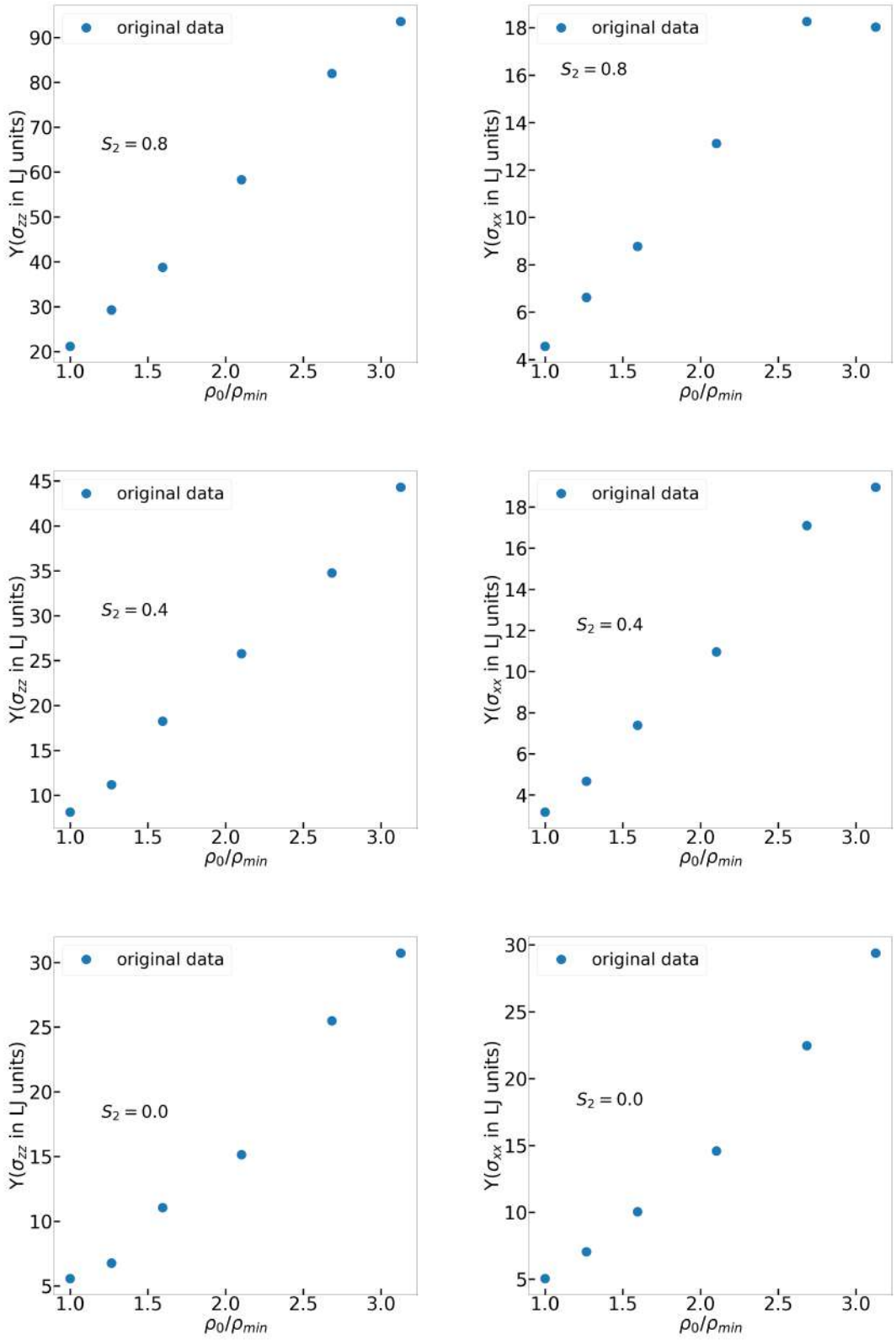


Figure 3.21: Linear modulus Y plotted as a function of nominal density ρ_0 for six different cases: (a)$\sigma_{zz}(S_2 \sim 0.8)$, (b)$\sigma_{xx}(S_2 \sim 0.8)$, (c)$\sigma_{zz}(S_2 \sim 0.4)$, (d)$\sigma_{xx}(S_2 \sim 0.4)$, (e)$\sigma_{zz}(S_2 \sim 0.0)$, (f)$\sigma_{xx}(S_2 \sim 0.0)$. Note the x-axis has been normalized by the lowest density $\rho_{min} = 0.079 g/cc$.

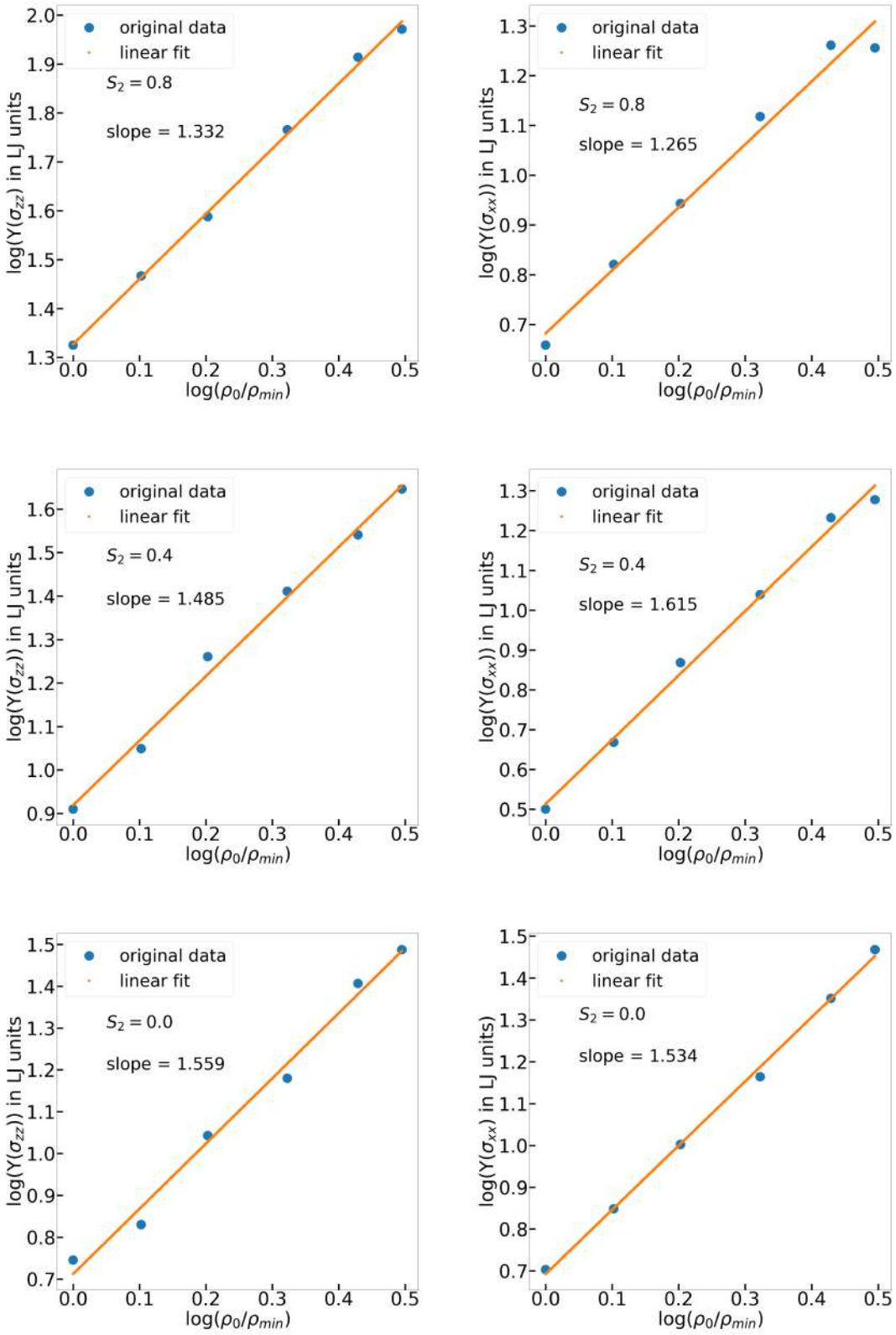


Figure 3.22: log-log plot of Linear modulus Y as a function of nominal density ρ_0 for six different cases: (a)$\sigma_{zz}(S_2 \sim 0.8)$, (b)$\sigma_{xx}(S_2 \sim 0.8)$, (c)$\sigma_{zz}(S_2 \sim 0.4)$, (d)$\sigma_{xx}(S_2 \sim 0.4)$, (e)$\sigma_{zz}(S_2 \sim 0.0)$, (f)$\sigma_{xx}(S_2 \sim 0.0)$. Note that x axis has been normalized by lowest density $\rho_{min} = 0.079 g/cc$. Stress values are in LJ units.

Chapter 4

Conclusion

We were deeply inspired by the elastic recovery of macroporous polymer nanocomposites under large strain. Earlier experimental work by Rajamanickam et al. has demonstrated such a response and the minimalistic coarse-grained model investigated by Anish et al. successfully captured such a mechanical response. We have replaced the effect of the polymer matrix which adsorbs on the surface of fillers and holds them in place by simple springs. Spherical voids were used to model the pores in the sponges which restricted the range of nominal densities/void volume fraction to be investigated. The bridge thickness Δ changed significantly across any two adjacent junctions, unlike the experimental setup where Δ was nearly constant.
We decided to work with cubical voids which allowed us to investigate the systems with void volume fraction $\phi_V \sim 0.9$ at the same time keeping Δ nearly unchanged across adjacent junctions. Since these cubical voids were placed on a lattice with lattice constant $L\sigma/3$, we ended up forming long beams between junctions. When such a system with beads and springs is compressed, we observe oscillations in the values σ_{xx} once the system buckles and enters regime-2. We also compared the response of scaffolds with cubical and spherical voids with approximately the same ρ_0 and concluded the spherical voids have more number of NPs at the interface compared to cubical voids.
Using cubical voids to achieve $\rho_0 = 0.069$ we found the functional dependence of Y on ρ_0, to be approximately linear $Y \sim \rho_0^{1.2}$. We are slightly off by the expected linear relationship. This might be because of long beams which bend under strain along with getting compressed.

We were fascinated by the response of scaffolds that incorporate anisotropic fillers. We first modelled a rod-like particle by adjoining spherical particles. We appended 4 spherical particles to make a rod and the aspect ratio was 4.75. We then designed systems of 6 different densities, each with three different order parameter $S_2 \sim 0.8, 0.4, 0.0$. We applied uniaxial strain in two different directions i.e. parallel and perpendicular to the orientation direction of rods.

With the currently designed system we have functional dependence of $Y \sim \rho_0^x$ with x ranging from 1.26 to 1.56. We stress that, we were not able to maintain the same intrinsic volume fraction ϕ_I across different ρ_0. We expect a significant increase in the stress response for $\rho_0 = 0.247$ and $0.212 g/cc$ systems as the ϕ_I values for these systems were low. Also, we were able to investigate only limited range densities $0.247 - 0.069 g/cc$. Bearing this we observe slope values for isotropic systems are generally higher than $S_2 \sim 0.4$ systems and $S_2 \sim 0.0$ systems have the lowest slope values.

Although our values right now are very far from the experimentally observed values ~ 2, we see a different response compared to scaffolds of spherical particles. We are not sure what value of ϕ_I do we need to keep for systems containing rod-like particles. It is a well-known fact that, if a cellular solid respond to deformation by bending its cell walls, then Young's modulus of the cellular solid scales with ρ_0 as, $Y \sim \rho_0^2$). If the cellular solid respond by compression, then $Y \sim \rho_0$. However, we observe the bending of the cell walls in both scaffolds made of spherical and rod-like particles in our simulation. This is because of the voids placed in a lattice which results in forming long beams, that generally bend on deformation.

Future perspectives and drawbacks of the model

In the experiments, scaffolds are compressed using a rheometer, and the measured stress value is plotted as a function of strain during compression and relaxation. We observe a hysteresis in the stress values which indicate dissipation in the system. We have not incorporated dissipative forces into our system. We plan to modify our system with a background implicit solvent such that NPs experience frictional drag proportional to their velocities.

Instead of placing voids on a lattice, if we disperse them randomly inside the scaffolds, we would get rid of long beams. We also try to make voids of different sizes and shapes akin to the experimental system. In the paper, [22] shear response of monoliths containing anisotropic hematite particles of different aspect ratios were measured using dynamic oscillatory shear rheology. Very weak frequency dependence of $G(\omega)$ showed scaffolds are indeed soft. One would also observe the functional dependence of G(ρ_0) similar to Y(ρ_0) i.e. $G \sim \rho_0$ for spherical particles and $G \sim \rho_0^2$ for ellipsoidal particles of aspect ratio 4.

We plan to shear the scaffold in the near future and show $Y \sim 2G$ indicating that Poisson ratio $\nu = 0$ as observed in the experiments as well as in the plateau regime of our model. We also plan to increase the range of density to be investigated for scaffolds made of rod-like particles as the density range of $0.07 - 0.25$ would be insufficient to conclude any dependence of Y(ρ_0).

We have also not investigated the effect of changing the aspect ratio of the filler. There is a systematic increase in the ρ_0 dependence of Y and G from linear to quadratic as the aspect ratio is increased from 1 to 4 suggestive of a change from cell wall compression to bending in response to deformation.

Appendix A

Appendix

A.1 Void volume fraction calculation

A.1.1 Void volume fraction calculation for open spherical voids

Void volume fraction(ϕ_V) is defined as the ratio of the volume occupied by all the voids to the volume of the simulation box. We have designed all the systems in table 2.1 having open, interconnected spherical voids. If we ignore the volume of the overlapping spherical voids and calculate the void volume fraction, we would end up double-counting volume intersection between the adjacent spherical voids and we obtain a higher void volume fraction.

Since we have 27 spherical voids, we divide our simulation box into 27 cubes of length $L\sigma/3$. Then each of the cubes with its spherical voids embedded would look like the figure A.1. Since the voids are open, a part of the void would pop out of the smaller cube. We will find the volume of these parts of the void which has come out of the cube (V_g) and subtract it from the volume of a spherical void ($4/3\pi R_V^3$). We call volume of the part of the void which lies inside the cube of $L\sigma/3$ as V_r. Then the quantity $27 \times V_r/L^3$ would give the correct void volume fraction. Now we discuss how to calculate V_r, first we calculate V_g:

$$\begin{aligned} V_g &= \int_{R_V - L/6}^{R_V} \int_0^{\theta} \int_0^{2\pi} r^2 dr sin\theta d\theta d\phi \\ &= \frac{2\pi}{3} \left(R_V^3 - (L/6)^3\right) (1 - cos(\theta)) \end{aligned} \tag{A.1}$$

Using basic geometry we can find the length x and θ in the figure A.1 i,e $x = \sqrt{R_V^2 - (L/6)^2}$ and $\tan(\theta) = x/R_V$ for given L and R_V. We can easily find the volume of a shaded region (V_g) in the figure by simple calculus. We can calculate $V_r = 4/3\pi R_V^3 - 6V_g$

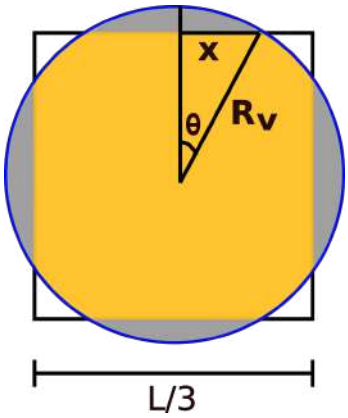


Figure A.1: The diagram helps to visualize the calculation of V_r(yellow region in this diagram). This schematic illuminates the size of a spherical void compared to the length $L\sigma/3$. We first calculate the volume of the grey region(V_r).

A.1.2 Void volume fraction for spherical and cubical voids

When we defined cylindrical and cuboidal regions we mentioned in the text we have 27 junctions, 81 cylinders of length $(L-6r_s)/3$ for cubical voids, 81 cuboids of length $(L-6b)/3$. Let us elucidate that point. Junctions are formed when orthogonal cylinders meet. We count the points where the cylinders meet, taking periodic boundary conditions into account. We have 8 complete junctions located inside the simulation box, we have 4 half junctions on each face and since we have six faces, there are a total of 12 junctions on the face. There are 2 quarter junctions located on the edge of the box, with 12 edges of the cube we have 6 junctions on the edge. Finally, we have a junction located on the 8 vertexes of the cube. So the total count is: 8+12+6+1 = 27.

We should be careful in not to overcount the volume of the junctions. So we first find the volume occupied by cylinders of length $(L-6r_s)/3$, which are located between any two junctions by first counting their total numbers. There are 36 complete cylinders located inside the simulation box (12 cylinders corresponding to each of the axes). There are 12 half-cylinders on each face of the simulation box, since we have 6 faces, there are 36 cylinders on the faces. 3 quarter cylinders on each edge contribute 9 cylinders. So we have a total of $36+36+9=81$ cylinders of length of $(L-6r_s)/3$.. The void volume fraction is given by the equation 2.3

We can also work out the volume of orthogonal intersection of two cylinders of radius r by simple calculus:

$$\begin{aligned} v_g &= 8\int_0^r \int_{-y}^{y} \sqrt{r^2-y^2}\, dzdy \\ &= 16\int_0^r y\sqrt{r^2-y^2}\, dy \\ &= \frac{16r^3}{3} \end{aligned} \tag{A.2}$$

We can also extend the similar argument when defining cuboidal regions, but now we have cuboids instead of cylinders, the corresponding void volume fraction is calculated by 2.5.

A.2 LAMMPS Instructions

Here we provide a summary of how one can use LAMMPS for molecular dynamics simulation and discuss some important commands. Complete detail can be found at https://docs.lammps.org/Manual.pdf.
LAMMPS is a classical "molecular dynamics simulator" that can be used for atomistic, mesoscale, and coarse-grain simulations with a variety of interatomic potentials and force fields. LAMMPS is well documented, easy to modify, extended with new capabilities, such as new force fields. In the most general sense, LAMMPS integrates Newton's equations of motion for a collection of interacting particles.
LAMMPS executes calculations by reading commands from an input script (text file), one line at a time. Each command causes LAMMPS to take some immediate action without regard for any commands that may be processed later. Commands may set an internal variable, read in a file, or run a simulation. For most of the input scripts written for the thesis had 3 parts to it, which we discuss in detail:
(a) Initialization: Here we specify dimensions (2D/3D), units(LJ/metals), boundary conditions(PBC/fixed), positions of all the atoms (lattice or can be set manually). For our project, we initialized the positions of particles manually using the read data command, which instructs LAMMPS to read a file. A data file can also consist of force fields, which can be set directly in the input script file. We used metal units for spherical particles systems and LJ units for rod-like particle systems.

(b) Setting the simulation: Once we set the atoms and molecular topology, we can define a variety of settings like force-field coefficients which include pair-coeffs, bond-coeffs, angle-coeffs, dihedral-coeff, special bonds. Before specifying the coefficients, we need to define the corresponding styles. For our project, we chose pair style lj/cut and used pair-style modify command to get WCA potential, harmonic bond style for springs between atoms, angle style cosine for implementing semiflexible rods, and special bonds

when WCA potential is used along with harmonic potential and gave their corresponding coefficients. We can also define a region, group the atoms and delete atoms. Indeed in the section 2.1 we used these commands to create voids, define a cylindrical region or cuboidal region.
Also one needs to choose a suitable value for timestep, neighbor list, comm-modify according to the problem. The comm-modify allow the user to set inter-processor communication of atom information that occurs each timestep as coordinates and other properties are exchanged between neighboring processor by increasing the cut-off distance for inter-processor communication. A very large cutoff will slow the simulation. Although a default value exists for these commands one has to choose values depending on the system being modelled. We used create-bonds command to create the bonds between NPs. Various computations can be specified for execution during a simulation using the compute. Some of the quantities that were computed include pressure tensor($\sigma_{\alpha\beta}$), potential energy due to springs and WCA interaction, total potential energy, radial distribution function g(r), and many more.

(c) Running a simulation and output options: To run a simulation we set a "fix" operation to atoms or a group of atoms. Examples include updating atom positions and velocities due to time integration, controlling temperature, applying constraint forces to atoms, deforming the simulation boxes. We have used fixes NVT, NPT, and deform. For the fix deform we have chosen parameters such that the box length L will change as a function of time such that:

$$L(t) = L_0(1 + erate * dt)$$

where dt is the elapsed time (in time units), $erate$ is the engineering strain rate(1/time units). We have chosen $erate$ for our simulation such that the box length decreases by 0.8 times the original box length along the direction of compression. For the NVT and NPT fixes one needs to choose the suitable value of damping factor which determines the frequency at which we call barostat and thermostat. The damping parameter is specified in time units and determines how rapidly the temperature/pressure is relaxed. For example, in our simulation in metal units, time unit was picosecond(ps), timestep was 5ps, we chose a damping factor of 100ps for the thermostat, 200ps for the barostat which means we are calling thermostat every 20 timesteps and barostat every 40 timesteps. Various output-related commands work with three different styles of data: global, per-atom, or local. A global data is one or more system-wide values, e.g. the temperature of the system. A per-atom data is one or more values per atom, e.g. the kinetic energy of each atom. Local datums are calculated by each processor based on the atoms it owns, but there may be zero or more per atom. For example, the bonds in our system were local data, as a NP has more than one bond connected to it.

There are several customized dumping options in LAMMPS, ”dump” command allows the user to dump position coordinates of atoms, their velocities, forces, even computed quantities by ”compute” commands every N timesteps in a file. Global quantities can be output by the thermo-style custom command, local quantities can be output by the dump local command, and the ”dump custom” command is used to dump per-atom quantities. Dumped coordinates can be used to visualize the system and make a movie. A ”fix print” command can also be used to dump computed global quantities in a file. A molecular dynamics simulation is run using the run command.

Bibliography

[1] A. C. Balazs, T. Emrick, and T. P. Russell, "Nanoparticle polymer composites: Where two small worlds meet," *Science*, vol. 314, no. 5802, pp. 1107–1110, 2006.

[2] M. C. Fernandes, J. Aizenberg, J. C. Weaver, and K. Bertoldi, "Mechanically robust lattices inspired by deep-sea glass sponges," *Nature Materials*, vol. 20, no. 2, pp. 237–241, 2021.

[3] J. Zhao, L. Wu, C. Zhan, Q. Shao, Z. Guo, and L. Zhang, "Overview of polymer nanocomposites: Computer simulation understanding of physical properties," *Polymer*, vol. 133, pp. 272–287, 2017.

[4] S. K. Kumar, V. Ganesan, and R. A. Riggleman, "Perspective: Outstanding theoretical questions in polymer-nanoparticle hybrids," *The Journal of chemical physics*, vol. 147, no. 2, p. 020 901, 2017.

[5] M. Moniruzzaman and K. I. Winey, "Polymer nanocomposites containing carbon nanotubes," *Macromolecules*, vol. 39, no. 16, pp. 5194–5205, 2006.

[6] H. Kim, A. A. Abdala, and C. W. Macosko, "Graphene/polymer nanocomposites," *Macromolecules*, vol. 43, no. 16, pp. 6515–6530, 2010.

[7] S. K. Kumar and R. Krishnamoorti, "Nanocomposites: Structure, phase behavior, and properties," *Annual Review of Chemical and Biomolecular Engineering*, vol. 1, pp. 37–58, 2010.

[8] A. Sukumar, N. Bachhar, A. Chatterji, and G. Kumaraswamy, "Elastic response of polymer-nanoparticle composite sponges: Microscopic model for large deformations," *Physical Review Materials*, vol. 6, no. 2, p. 025 604, 2022.

[9] M. F. Ashby and L. J. Gibson, "Cellular solids: Structure and properties," *Press Syndicate of the University of Cambridge, Cambridge, UK*, pp. 175–231, 1997.

[10] A. J. Crosby and J.-Y. Lee, "Polymer nanocomposites: The "nano" effect on mechanical properties," *Polymer reviews*, vol. 47, no. 2, pp. 217–229, 2007.

[11] E. Senses, M. Tyagi, M. Pasco, and A. Faraone, "Dynamics of architecturally engineered all-polymer nanocomposites," *Acs Nano*, vol. 12, no. 11, pp. 10 807–10 816, 2018.

[12] B. L. Smith, T. E. Schäffer, M. Viani, *et al.*, "Molecular mechanistic origin of the toughness of natural adhesives, fibres and composites," *Nature*, vol. 399, no. 6738, pp. 761–763, 1999.

[13] P. Podsiadlo, A. K. Kaushik, E. M. Arruda, *et al.*, "Ultrastrong and stiff layered polymer nanocomposites," *Science*, vol. 318, no. 5847, pp. 80–83, 2007.

[14] S. Chatterjee, K. Shanmuganathan, and G. Kumaraswamy, "Fire-retardant, self-extinguishing inorganic/polymer composite memory foams," *ACS applied materials & interfaces*, vol. 9, no. 51, pp. 44 864–44 872, 2017.

[15] S. Chatterjee, P. Doshi, and G. Kumaraswamy, "Capillary uptake in macroporous compressible sponges," *Soft Matter*, vol. 13, no. 34, pp. 5731–5740, 2017.

[16] S. Chatterjee, A. Potdar, S. Kuhn, and G. Kumaraswamy, "Preparation of macroporous scaffolds with holes in pore walls and pressure driven flows through them," *RSC advances*, vol. 8, no. 44, pp. 24 731–24 739, 2018.

[17] C. Das, S. Chatterjee, G. Kumaraswamy, and K. Krishnamoorthy, "Elastic compressible energy storage devices from ice templated polymer gels treated with polyphenols," *The Journal of Physical Chemistry C*, vol. 121, no. 6, pp. 3270–3278, 2017.

[18] A. F. Ismail and P. S. Goh, *Carbon-based polymer nanocomposites for environmental and energy applications*. Elsevier, 2018.

[19] R. Rajamanickam, S. Kumari, D. Kumar, *et al.*, "Soft colloidal scaffolds capable of elastic recovery after large compressive strains," *Chemistry of Materials*, vol. 26, no. 17, pp. 5161–5168, 2014.

[20] K. Davami, L. Zhao, E. Lu, *et al.*, "Ultralight shape-recovering plate mechanical metamaterials," *Nature communications*, vol. 6, no. 1, pp. 1–7, 2015.

[21] L. R. Meza, S. Das, and J. R. Greer, "Strong, lightweight, and recoverable three-dimensional ceramic nanolattices," *Science*, vol. 345, no. 6202, pp. 1322–1326, 2014.

[22] G. Kumaraswamy, K. Suresh, H. Lama, M. G. Basavaraj, and D. K. Satapathy, "Ice templated nanocomposites containing rod-like hematite particles: Interplay between particle anisotropy and particle–matrix interactions," *Journal of Applied Physics*, vol. 128, no. 3, p. 034 702, 2020.

[23] J.-I. Weon and H.-J. Sue, "Effects of clay orientation and aspect ratio on mechanical behavior of nylon-6 nanocomposite," *Polymer*, vol. 46, no. 17, pp. 6325–6334, 2005.

[24] P. Das, J.-M. Malho, K. Rahimi, *et al.*, "Nacre-mimetics with synthetic nanoclays up to ultrahigh aspect ratios," *Nature communications*, vol. 6, no. 1, pp. 1–14, 2015.

[25] J. R. Capadona, O. Van Den Berg, L. A. Capadona, *et al.*, "A versatile approach for the processing of polymer nanocomposites with self-assembled nanofibre templates," *Nature Nanotechnology*, vol. 2, no. 12, pp. 765–769, 2007.

[26] J.-G. Park, J. D. Forster, and E. R. Dufresne, "High-yield synthesis of monodisperse dumbbell-shaped polymer nanoparticles," *Journal of the American Chemical Society*, vol. 132, no. 17, pp. 5960–5961, 2010.

[27] S. Deville, "The lure of ice-templating: Recent trends and opportunities for porous materials," *Scripta Materialia*, vol. 147, pp. 119–124, 2018.

[28] C.-Y. Hsieh, S.-P. Tsai, M.-H. Ho, *et al.*, "Analysis of freeze-gelation and cross-linking processes for preparing porous chitosan scaffolds," *Carbohydrate polymers*, vol. 67, no. 1, pp. 124–132, 2007.

[29] K. Suresh and G. Kumaraswamy, "Effect of electrostatic interactions on structure and mechanical properties of ice templated colloid-polymer composites," *Journal of Physics D: Applied Physics*, vol. 52, no. 21, p. 214 002, 2019.

[30] B. Pandey, S. Chatterjee, N. Parekh, P. Yadav, A. Nisal, and S. Sen Gupta, "Silk-mesoporous silica-based hybrid macroporous scaffolds using ice-templating method: Mechanical, release, and biological studies," *ACS Applied Bio Materials*, vol. 1, no. 6, pp. 2082–2093, 2018.

[31] K. Suresh, A. Chowdhury, S. K. Kumar, and G. Kumaraswamy, "Critical role of processing on the mechanical properties of cross-linked highly loaded nanocomposites," *Macromolecules*, vol. 52, no. 15, pp. 5955–5962, 2019.